ALMA MATER STUDIORUM
UNIVERSITÀ DI BOLOGNA

DEPARTMENT OF PHYSICS AND ASTRONOMY "A. RIGHI"

SECOND CYCLE DEGREE

PHYSICS

Statistical Analysis of the Nuclear Three-Body Problem

Defended by:
Silvia Zironi

Supervisor:
Prof. Paolo Finelli
Co-Supervisor:
Prof. Matteo Vorabbi, University of Surrey

Accademic year 2025-2026

Abstract

The quantum three-nucleon problem represents a fundamental benchmark in nuclear few-body physics as it provides a direct test of how two-nucleon (NN) interactions propagate into three-body observables. In this thesis, the triton binding energy has been studied by solving the homogeneous Faddeev equations in momentum space, with the goal of understanding both numerical stability aspects and the sensitivity of the result to model choices and NN interaction parameters.

The work is organized in two main parts. First, the numerical framework has been validated using the phenomenological Malfliet-Tjon potential, allowing a controlled assessment of the behavior of the triton binding energy under variations of the potential parameters. In the explored region the binding energy varies smoothly and no numerical instabilities are observed, providing a controlled and reliable benchmark for the subsequent calculations. The analysis has been then extended to chiral effective field theory NN interactions at different chiral orders and regulator cutoffs. A Bayesian approach has been adopted to treat the cutoff in a quantitative way: posterior distributions over the cutoff have been constructed from the agreement with the experimental triton binding energy, and Bayesian model averaging is used to propagate residual regulator dependence into a final estimate. The analysis shows a strong cutoff preference at leading order (LO) which progressively reduces at higher orders, consistent with an improving regulator independence of the interaction. An investigation of the local sensitivity of the triton binding energy to contact low energy constants (LECs) has been also performed. At NLO, the response of the triton energy is correlated with specific operator components of the NN interaction. To clarify this connection, the impact of LEC variations on NN partial-wave interaction matrices and phase shifts is explicitly analyzed. The study shows that the dominant variations mainly affect low momentum P-wave channels, while S-wave channels remain comparatively constrained. This combined three-body and partial-wave analysis highlights the limited flexibility of NN only adjustments and supports the need for genuine three-nucleon forces in achieving a fully consistent description.

Contents

Chapter 1

Introduction

1.1 Three-body systems in nuclear physics

The quantum mechanical three-body problem occupies a central role in nuclear physics, as it represents the simplest non trivial extension of two-body dynamics and already exhibits qualitative features that have no analogue in two-particle systems. The presence of a third particle introduces genuinely new dynamical effects, including channel coupling, particle exchange and sensitivity to off-shell properties of the interaction.

By the late 1960s and early 1970s, the theoretical formulation of the non-relativistic three-body problem had reached a mature stage. Rigorous integral equation approaches have been developed, culminating in the Faddeev formalism, which provides a mathematically consistent decomposition of the full three-body wavefunction into components associated with each interacting pair. Unlike straightforward generalizations of the Lippmann-Schwinger equations, the Faddeev equations pose unique solutions for both bound state and scattering problems and treat all possible two-body subsystems on equal footing. At the same time, numerical techniques had become sufficiently advanced to allow realistic calculations involving complicated interactions and non trivial channel structures. The main focus of research consequently shifted from the development of formal methods to their application to realistic problems in nuclear physics ([1]).

A key motivation for the study of three-body systems lies in the fact that reactions involving three particles constitute the simplest example of multichannel processes. In contrast to two-body scattering, where intuition based on asymptotic states often provides reliable guidance, three-body dynamics is governed by interference effects, exchange mechanisms and correlations that cannot be reduced to pairwise interactions alone. The Faddeev equations provide a natural framework to account for these features, as they treat all possible two-body subsystems on equal footing and incorporate the full coupling between different reaction channels.

Beyond their formal significance, three-body systems play a crucial role as probes of the underlying nuclear forces. Since two-nucleon scattering data constrain only the on-shell properties of the interaction, they are insufficient to uniquely determine the nucleon-nucleon potential. Three-nucleon observables, such as the binding energies of the triton and helium-3 or nucleon-deuteron scattering observables, provide additional contributions. As reported in [1], for a long time it was hoped that the systematic study of three-nucleon systems could help resolve the ambiguities inherent in two-body phenomenology.

The triton, as the simplest bound three-nucleon system, occupies a particularly prominent position in this context. Its binding energy is sensitive to the detailed structure of the two-nucleon interaction, especially in the low partial waves, and provides a stringent benchmark for theoretical models. Calculations based exclusively on realistic two-nucleon potentials have historically underestimated the experimental binding energy, highlighting the importance of off-shell effects, higher partial waves and potentially genuine three-nucleon forces.

1.2 Motivation for the study

Despite the long research on three-body systems, the quantitative description of the three-nucleon bound state remains a challenging problem. The Faddeev equations provide an exact formulation of the three-body Schrödinger equation, but their practical solution requires advanced numerical methods. The integral kernels are nonlocal, they depend on off-shell two-body transition operators and they involve multidimensional integrations over momentum and angular degrees of freedom. Hence ensuring numerical stability and convergence is a non trivial task.

At the same time, the triton plays a central role as a benchmark for nuclear interaction models. Any realistic description of nuclear forces must be able to reproduce its binding energy within controlled theoretical uncertainties. This requirement has acquired importance with the development of modern nucleon-nucleon interactions that aim at a consistent description of nuclear forces. In this context, reliable three-body calculations are indispensable not only for testing the quality of the interactions but also for assessing the sensitivity of three-body observables to variations in the underlying two-body parameters.

1.3 Objectives of the thesis

The objective of this thesis is the numerical study of the three-nucleon bound-state problem within the framework of the Faddeev formalism in momentum space, in particular for the triton. This work is based on the analysis and application of established numerical codes that implement the Faddeev equations for three-nucleon systems.

A primary goal of the thesis is to gain a detailed understanding of the numerical solution of the homogeneous Faddeev equation for the three-body bound state. This includes a careful study of the structure of the three-body kernel, the role of the two-body transition operator and the treatment of permutation operator in momentum space.

The second objective is the systematic use of benchmark numerical implementations to compute the triton binding energy for different classes of NN interactions. Phenomenological interactions are used as reference cases to validate the numerical procedure. More advanced interaction models are then used to extend the analysis beyond simplified benchmarks, allowing for a consistent comparison within the same three-body framework.

Another goal of this work is to investigate the sensitivity of three-body observables (binding energy, in particular) to variations in the two-body input and in the numerical parameters entering the calculations. Since three-body bound-state properties depend on the off-shell aspects of the Nucleon-Nucleon (NN) interaction as well as on the details of the numerical treatment, it is essential to work with a controlled and well understood computational setup. The triton binding energy is used through this project as a diagnostic observable to quantify these sensitivities.

Chapter 2 introduces the theoretical framework of the Faddeev equations, Chapter 3 is devoted to the numerical implementations employed in this work, and the subsequent chapters focus on applications and quantitative analysis.

Chapter 2

Theoretical background

2.1 Few-body systems in nuclear physics

Few-body systems occupy a special position in nuclear physics, as they represent the simplest many-body systems in which non trivial correlations and reaction mechanisms emerge. In particular, three-body systems constitute the minimal setting in which multichannel dynamics, particle exchange and interference effects play a fundamental role. These features have no direct analogue in two-body systems and cannot be captured by a simple extension of two-particle concepts, but they require dedicated theoretical tools.

From a physical point of view, the study of few-nucleon systems is motivated by the structure of the nuclear interactions itself. Nuclear forces are known primarily through two-nucleon scattering data and bound-state properties of the deuteron. While such data provide stringent constraints on the on-shell behavior of the interaction, they are insufficient to uniquely determine its off-shell properties. Since many-body observables are sensitive to off-shell effects and to the interplay between different interaction channels, few-body systems offer a unique testing ground for models of the NN force.

Three-body systems are particularly well suited for this purpose. The presence of a third particle introduces additional degrees of freedom and allows one to prove aspects of the interaction that remain inaccessible in the two-body cases. Three-nucleon observables such as bound-state energies and scattering cross sections provide complementary information to two-body data and play a central role in assessing the consistency and predictive power of nuclear interaction models.

At the same time, the theoretical description of three-body systems represents a significant challenge. A naive formulation of the three-body Schrödinger equation in either configuration space or momentum space leads to equations that are difficult to interpret and to solve numerically. Multiple scattering processes, rearrangement channels and particle exchange contributions are strongly coupled and cannot be treated independently. As a result, direct approaches based on the full three-body wavefunction tend to ignore the underlying structure of the problem and to suffer from numerical instabilities.

These difficulties motivated the development of alternative formulations of the three-body problem that exploit the pairwise nature of the nuclear interaction. Integral equation approaches, in particular, proved to be especially well suited for this purpose. By reorganizing the dynamics in terms of interactions between pairs of particles and systematically accounting for particle exchange, such formulations make it possible to disentangle the complex structure of the three-body problem and to construct equations mathematically well defined.

Within this context, the Faddeev formalism represents a decisive conceptual advance. Instead of working with the full three-body wavefunction, the Faddeev approach decomposes the problem into components associated with each interacting pair. This decomposition eliminates double counting of interaction processes and leads to a set of coupled integral equations that posses unique solutions for both bound-state and scattering processes. This reformulation provides a transparent and rigorous framework for the description of three-body dynamics and has become the standard theoretical tool in few-body nuclear physics.

2.2 Nuclear forces

The nuclear force constitutes the fundamental building block of any few-body nuclear calculation. It encodes the effective interaction between nucleons at low energies, where the relevant degrees of freedom are protons and neutrons rather than the underlying quark and gluon fields of quantum chromodynamics (QCD). Despite its long history, the precise form of the nuclear interaction remains a non trivial subject, reflecting the complexity of the strong interaction in the non-perturbative regime.

At energies below the pion production threshold, nuclear forces are commonly described in terms of effective potentials acting between nucleons. These potentials are not observables themselves, but theoretical constructs designed to reproduce experimental data, such as NN scattering phase shifts and bound-state properties, when inserted into a dynamical equation like the Schrödinger or Lippmann-Schwinger equation. As a consequence, nuclear potentials are not uniquely defined: different interaction models may reproduce the same on-shell observables while differing in their off-shell behavior.

2.2.1 Two-nucleon forces

Historically, the dominant contribution to nuclear binding and scattering phenomena has been attributed to two-nucleon forces. These interactions are characterized by a short range repulsion, an intermediate range attraction and a long range component governed by pion exchange. Early phenomenological models captured these features through combinations of Yukawa type terms or operator structures fitted to experimental data.

Modern descriptions of NN forces can be broadly divided into phenomenological potentials and interactions derived within effective field theory frameworks. Phenomenological potentials, such as the **Malfliet-Tjon model**, are constructed by assuming specific functional forms and adjusting a limited set of parameters to reproduce selected NN observables. While these models are not directly connected to QCD, they often provide numerically stable and computationally convenient interactions, making them valuable tools for benchmarking few-body calculations.

In particular, the Malfliet-Tjon (MT) potential represents a simple yet widely used effective NN interaction. It consists of a superposition of an attractive and a repulsive Yukawa term with different ranges [2]:

$$V(r) = \lambda_R \frac{e^{-\mu_R r}}{r} - \lambda_A \frac{e^{-\mu_A r}}{r}, \tag{2.1}$$

where λ_R and λ_A are the repulsive and attractive components, respectively. The parameters μ_R and μ_A control the range of the repulsive and attractive components, typically chosen that $\mu_R > \mu_A$, ensuring a short range repulsive core and an intermediate range attraction.

The qualitative radial behavior of an effective NN potential is illustrated in fig. 2.1, highlighting the short range repulsive core, the intermediate range attraction, and the long range tail associated with pion exchange.

Despite their simplicity, these potentials capture essential features of low energy NN dynamics and have been widely used in three-body bound-state calculations as reference models. Their use allows one to isolate and analyze the numerical aspects of the three-body problem without the additional complications associated with more elaborate interaction models.

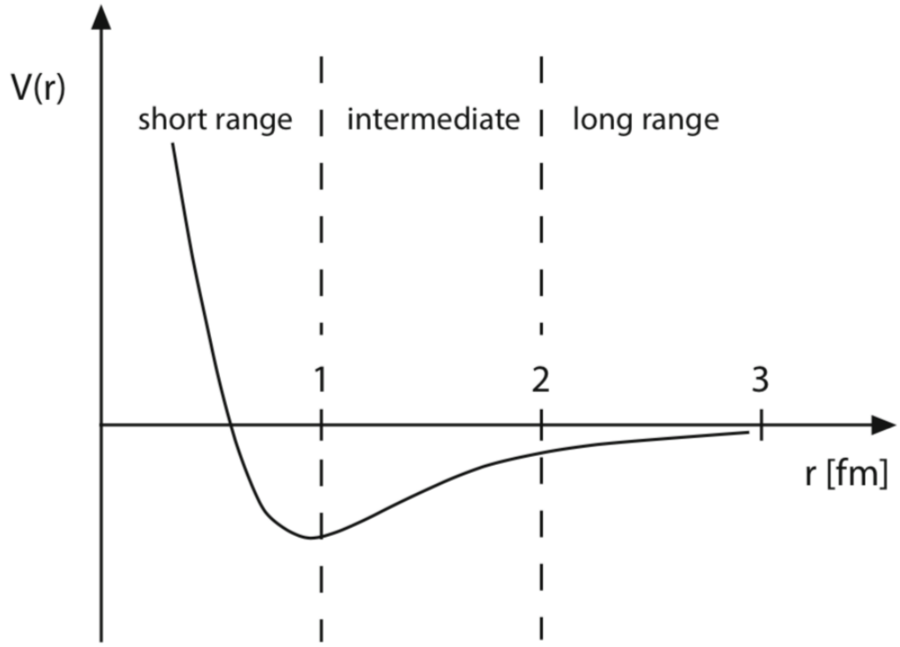

Figure 2.1: Illustrative radial dependence of the Malfliet–Tjon potential, showing the short range repulsive core, intermediate range attraction and long range pion exchange tail.

2.2.2 Chiral effective field theory interactions

A conceptually different approach to nuclear forces is provided by **chiral effective field theory (χEFT)**. In this framework, nuclear interactions are derived systematically from the symmetries of QCD, in particular approximate chiral symmetry, using nucleons and pions as explicit degrees of freedom. The interaction is organized as an expansion in powers of a low momentum scale over a breakdown scale, allowing a controlled and improvable description of nuclear forces.

Chiral EFT naturally generates both two-nucleon and many-nucleon interactions within the same theoretical scheme. Long range contributions arise from pion exchange, while short range one is encoded in contact operators whose strengths are fixed by experimental data. One of the main advantages of this approach is its ability to provide a consistent hierarchy of interactions and a framework for uncertainty quantification.

A more detailed discussion of chiral interactions and their implementation in few-body calculations is deferred to section 2.6.

2.2.3 Three-nucleon forces

While two-nucleon forces account for the bulk of nuclear binding, it has long been recognized that they are not sufficient to fully describe three- and many-body observables. In particular, calculations based solely on NN interactions tend to under bind light nuclei such as the triton and fail to reproduce certain scattering observables. This has led to the introduction of genuine three-nucleon forces, which depend simultaneously on the coordinates of the three nucleons and cannot be reduced to a sum of pairwise interactions.

From a theoretical standpoint, three-nucleon forces arise naturally in chiral EFT at sub leading orders and reflect the composite nature of the nucleon and the underlying dynamics of QCD. Phenomenological three-body forces have also been proposed and successfully applied in few-body calculations.

The present analysis, however, is performed at the two-body level only. The Hamiltonian includes NN interactions up to NLO, but no explicit three-nucleon force contributions are

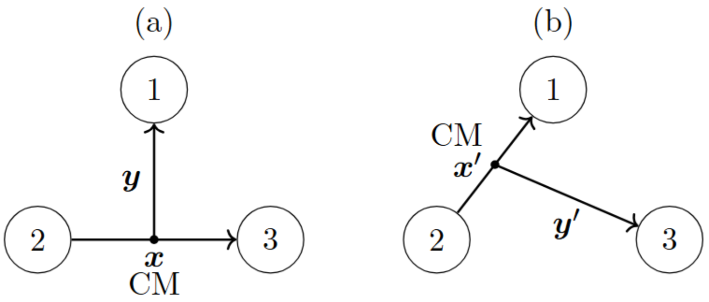

Figure 2.2: Different Jacobi coordinate sets for a three-body system corresponding to different pair-spectator partitions. In each panel, the coordinate $\boldsymbol{x}$ (or $\boldsymbol{x}'$) describes the relative motion inside the interacting pair, while $\boldsymbol{y}$ (or $\boldsymbol{y}'$) denotes the motion of the spectator particle with respect to the center of mass of that pair.

considered. As a consequence, the scope of the thesis is limited to two-nucleon scattering observables and to the local parameter sensitivity of the NN sector. Three-body forces, although naturally emerging in χEFT at subleading orders, lie beyond the scope of this work.

2.3 Three-body dynamics

The theoretical formulation of a quantum three-body system begins by separating the center of mass motion from the intrinsic degrees of freedom. Since the nuclear interaction is translationally invariant, this separation allows one to describe the internal dynamics of the system in terms of a reduced set of relative coordinates. A natural choice for this purpose is provided by the **Jacobi coordinates**, which are particularly well suited for systems governed by pairwise interactions.

It should be noted that Jacobi coordinates are not uniquely defined: different conventions can be adopted depending on the choice of particle partition and on the specific normalization of coordinates. In the following, we adopt the standard Jacobi coordinates corresponding to a given pair-spectator partition, which are commonly used in few-body nuclear physics. Other equivalent conventions lead to the same physical results and differ only by linear transformations. Two equivalent examples are shown in fig. 2.2, corresponding to different pair-spectator partitions.

For a system of three identical nucleons of mass m, with position vector $\mathbf{x}_1, \mathbf{x}_2$ and $\mathbf{x}_3$, the Jacobi coordinates corresponding to the partition $(1,2) - 3$ are defined as [3]:

$$\mathbf{x} = \mathbf{x}_2 - \mathbf{x}_1, \qquad \mathbf{y} = \mathbf{x}_3 - \frac{\mathbf{x}_1 + \mathbf{x}_2}{2}, \tag{2.2}$$

where $\mathbf{x}$ describes the relative motion inside the interacting pair $(1,2)$ and $\mathbf{y}$ represents the motion of the spectator particle 3 relative to the center of mass of that pair.

In terms of these coordinates, the relative distances between the three particles can be expressed as a linear combinations of $\mathbf{x}$ and $\mathbf{y}$:

$$\mathbf{x}_{12} = \mathbf{x}, \qquad \mathbf{x}_{23} = \mathbf{y} - \frac{1}{2}\mathbf{x}, \qquad \mathbf{x}_{31} = \mathbf{y} + \frac{1}{2}\mathbf{x}. \tag{2.3}$$

This representation highlights an important feature of the three-body problem: although each interaction depends only on the distance between two particles, the corresponding potential operator act on different combinations of the Jacobi coordinates.

The intrinsic kinetic energy operator is diagonal in the Jacobi coordinates $\mathbf{x}$ and $\mathbf{y}$ and takes the form [4]:

$$H_0 = -\frac{\hbar^2}{m}\left(\nabla_{\mathbf{x}}^2 + \frac{3}{4}\nabla_{\mathbf{y}}^2\right). \tag{2.4}$$

Including the pairwise interactions, the intrinsic three-body Hamiltonian can be written as:

$$H = -\frac{\hbar^2}{m}\left(\nabla_{\mathbf{x}}^2 + \frac{3}{4}\nabla_{\mathbf{y}}^2\right) + V(\mathbf{x}) + V\left(\mathbf{y} + \frac{1}{2}\mathbf{x}\right) + V\left(\mathbf{y} - \frac{1}{2}\mathbf{x}\right), \tag{2.5}$$

where $V(\mathbf{x})$ denotes the interactions between particles 1 and 2, while the other two terms correspond to the interactions between particles 2 and 3 and between particles 1 and 3, respectively.

Although this Hamiltonian involves only pairwise interactions, its structure already illustrates the intrinsic complexity of the three-body problem. Each potential term acts on a different linear combination of the Jacobi coordinates, implying that all components of the total wavefunction are strongly coupled. As a consequence, a direct solution of the three-body Schrödinger equation in coordinate space becomes numerically challenging and obscures the underlying multiple scattering structure of the problem.

This observation provides the natural starting point for the derivation of the Faddeev equations. By decomposing the total wavefunction into components associated with each interacting pair, the Faddeev formalism reorganizes the three-body dynamics in a way that eliminates double counting of interaction processes and leads to a mathematically well posed integral equation formulation of the three-body problem.

2.4 The Faddeev equations

The quantum mechanical three-body problem is fundamentally more complex than the two-body case due to the coupling of different pairwise interactions in the Schrödinger equation. As said in 2.3, the Hamiltonian written in Jacobi coordinates contains three distinct potentials depending on different linear combinations of the relative coordinates. This form prevents a straightforward separation of variables and makes the direct solution of the three-body Schrödinger equation impractical for realistic interactions.

An alternative formulation came with the derivation of the **Faddeev equations**, introduced by Ludvig Faddeev in the '60, which provide a rigorous and tractable method for solving the three-body bound state and scattering problems. Its key idea is to rewrite the total wavefunction as a sum of three components, each associated with one interacting pair but still containing the full three-body dynamics.

Consider three particles labeled $1, 2, 3$ with masses m_i and free Hamiltonian H_0. The interaction is assumed to be purely pairwise, described by potentials V_i in Jacobi coordinates:

$$V_1 \equiv V_{23} = V(\mathbf{x}), \qquad V_2 \equiv V_{13} = V(\mathbf{y} + \frac{1}{2}\mathbf{x}), \qquad V_3 \equiv V_{12} = V(\mathbf{y} - \frac{1}{2}\mathbf{x}). \tag{2.6}$$

The total Hamiltonian 2.5 becomes then:

$$H = H_0 + V_1 + V_2 + V_3, \tag{2.7}$$

and the exact three-body wavefunction $|\Psi\rangle$ for a state of energy E satisfies the Schrödinger equation:

$$(E - H_0 - V_1 - V_2 - V_3)|\Psi\rangle = 0. \tag{2.8}$$

This equation is formally simple, but it entangles all three interactions in a way that makes it extremely difficult to separate the different physical processes and to formulate a stable and unique integral equation.

A starting point for the three-body problem is the so called triad of **Lippmann-Schwinger equations**. Introducing the free Green's operator:

$$G_0(E) = \frac{1}{E - H_0 + i\varepsilon}, \tag{2.9}$$

one can write for a scattering state $|\Psi^{(+)}\rangle$ three formally equivalent Lippmann-Schwinger equations:

$$|\Psi^{(+)}\rangle = |\Phi_\alpha\rangle + G_0(E)\, V_\alpha\, |\Psi^{(+)}\rangle, \qquad \alpha = 1, 2, 3, \tag{2.10}$$

where $|\Phi_\alpha\rangle$ denotes an appropriate incoming channel (for example a nucleon-deuteron state for a nucleon-deuteron scattering). The key idea here is that, while each of the three equations in 2.10 has a non compact and non connected kernel, the requirement that a physical scattering state must satisfy all three equations simultaneously is sufficient to fix uniquely the solution and the associated boundary conditions. However the triad itself does not yet provide a numerically convenient coupled equation scheme.

Faddeev's idea was precisely to reformulate the three-body problem in terms of **Faddeev components**. The starting point is the formal solution of equation 2.8 in operator form:

$$|\Psi\rangle = G_0(E)\,(V_1 + V_2 + V_3)\,|\Psi\rangle. \tag{2.11}$$

Faddeev introduced three components $|\psi_i\rangle$ defined as:

$$|\psi_i\rangle \equiv G_0(E) V_i |\Psi\rangle, \qquad i = 1, 2, 3. \tag{2.12}$$

By construction, the sum of these components gives the full wavefunction:

$$|\Psi\rangle = |\psi_1\rangle + |\psi_2\rangle + |\psi_3\rangle. \tag{2.13}$$

The physical interpretation is that each ψ_i contains all processes in which the last interaction acting to the right is V_i. In practice, ψ_1 collects all scattering sequences ending with a (23) interaction, ψ_2 those ending with (13) interaction and so on. This decomposition separates the multiple scattering series into three non overlapping parts. Applying G_0^{-1} to the equation 2.12 and using 2.13 gives:

$$G_0^{-1}|\psi_i\rangle = V_i(|\psi_1\rangle + |\psi_2\rangle + |\psi_3\rangle). \tag{2.14}$$

Since V_i acts only inside the two-body subsystem not containing particle i, one obtains:

$$(E - H_0)|\psi_i\rangle = V_i \sum_{j \neq i} |\psi_j\rangle \tag{2.15}$$

Multiplying again by G_0:

$$|\psi_i\rangle = G_0 V_i |\Psi\rangle = G_0 V_i \sum_{j=1}^{3} |\psi_j\rangle = G_0 V_i \sum_{j \neq i} |\psi_j\rangle, \tag{2.16}$$

where has been used the fact that the term with $j = i$ can be absorbed into the two-body transition operator, as will be discussed in the next section. This set of equations is equivalent to the original Schrödinger equation 2.8, but has a more simple structure.

2.4.1 Operator form with two-body t-matrices

It is often convenient to replace the potentials V_i with the corresponding **two-body t-matrices**, which resum all repeated interactions inside each pair. The t-matrix for pair i is defined by the Lippmann-Schwinger equation:

$$t_i(E) = V_i + V_i G_0(E) t_i(E). \tag{2.17}$$

This equation is identical in form to the usual two-body Lippmann-Schwinger equation, but the propagator G_0 now contains the kinetic energy of the spectator particle as well, so that t_i is an off-shell operator depending on the total three-body energy E.

Using this identity in the equation 2.16, one obtains the standard operator form of the Faddeev equations:

$$|\psi_i\rangle = G_0(E)\, t_i(E) \sum_{j\neq i} |\psi_j\rangle, \qquad i = 1, 2, 3. \tag{2.18}$$

Equations 2.18 are the **Faddeev equations** for the three-body system with purely pairwise interactions. The structure is clear: each Faddeev component describes all processes that start with an interaction in pair (jk) and are followed by arbitrary rescattering involving the other pairs. Writing out the set explicitly:

$$\begin{cases} |\psi_1\rangle = G_0\, t_1 \left(|\psi_2\rangle + |\psi_3\rangle\right), \\ |\psi_2\rangle = G_0\, t_2 \left(|\psi_3\rangle + |\psi_1\rangle\right), \\ |\psi_3\rangle = G_0\, t_3 \left(|\psi_1\rangle + |\psi_2\rangle\right). \end{cases}$$

When the three constituents are identical nucleons, as in the nucleon-deuteron system where the underlying degrees of freedom are three identical fermions, the system of equations 2.18 can be further simplified by exploiting permutation symmetry. Introducing the permutation operators P_{ij}, which exchange particles i and j, one defines the combined operator:

$$P = P_{12}P_{23} + P_{13}P_{23}, \tag{2.19}$$

which generates cyclic permutations of the three particles. Using P the total wavefunction can be expressed choosing a single component (for example $|\psi_1\rangle$) as:

$$|\Psi\rangle = (1 + P)|\psi_1\rangle. \tag{2.20}$$

The three coupled equations collapse into a single Faddeev equation for $|\psi_1\rangle$:

$$|\psi_1\rangle = G_0(E) t_1(E) P |\psi_1\rangle, \tag{2.21}$$

which is the form most commonly used in numerical three-nucleon calculations [5].

2.4.2 Coordinate and momentum-space representations

The operator form on the Faddeev equations 2.18 is independent of the choice of the representation. For practical calculations it is convenient to work either in coordinate space, using Jacobi coordinates, or in momentum space, using the corresponding Jacobi momenta. Both representations are completely equivalent, but the momentum-space form is particularly well suited to treat non local and energy dependent interactions, such as realistic nucleon-nucleon potentials, and is the starting point for the most modern three-nucleon calculations (the Jacobi coordinates and the intrinsic Hamiltonian have already been introduced in section 2.3).

Momentum space basis

For each partition i, the Jacobi momenta $(\mathbf{p}_i\mathbf{q}_i)$ are defined as the conjugate variables to the Jacobi coordinates describing respectively the internal motion of the pair (jk) and the motion of the spectator i relative to the pair. Introducing the reduced masses:

$$\mu_i = \frac{m_j m_k}{m_j + m_k}, \qquad M_i = \frac{m_i(m_j + m_k)}{m_i + m_j + m_k}, \tag{2.22}$$

where m_i denotes the mass of the particle i, which for three identical nucleons of mass m reduce to:

$$\mu_i = \frac{m}{2}, \qquad M_i = \frac{2m}{3}. \tag{2.23}$$

In this basis ($|\mathbf{p}_i\mathbf{q}_i\rangle$) the free Green's operator becomes diagonal:

$$G_0(E; \mathbf{p}_i, \mathbf{q}_i) = \left(E - \frac{p_i^2}{2\mu_i} - \frac{q_i^2}{2M_i} + i\varepsilon\right)^{-1}, \tag{2.24}$$

which is the form used in all momentum space Faddeev calculations. The variable p_i describes the internal kinetic energy of the interaction pair, while q_i sets the energy available to the spectator.

The potential V_i acts only on the internal motion of the bound pair (jk). Consequently, the two-body transition operator embedded in the three-body space factorizes as:

$$\langle \mathbf{p}_i\mathbf{q}_i|t_i(E)|\mathbf{p}_i'\mathbf{q}_i'\rangle = \delta^{(3)}(\mathbf{q}_i - \mathbf{q}_i')t_i(\mathbf{p}_i, \mathbf{p}_i'; E - q_i^2/2M_i), \tag{2.25}$$

hence, the spectator momentum is conserved, while the two-body t-matrix depends on the shifted two-body energy $\varepsilon = E - \frac{q_i^2}{2M_i}$. The shift embodies the off-shell character of two-body dynamics inside the three-body system. Putting equations 2.24 and 2.25 into 2.18 gives the integral form:

$$\psi_i(\mathbf{p}_i, \mathbf{q}_i) = G_0(E; \mathbf{p}_i, \mathbf{q}_i) \sum_{j \neq i} \int d^3p_i' \; t_i(\mathbf{p}_i, \mathbf{p}_i'; E - q_i^2/2M_i)\, \psi_j(\mathbf{p}_j', \mathbf{q}_j'), \tag{2.26}$$

where the transformed momenta $(\mathbf{p}_j', \mathbf{q}_j')$ follow from a linear permutation of the Jacobi sets.

2.4.3 Bound state solutions of the Faddeev equations

The Faddeev formalism applies equally well to scattering and to bound states. However, the focuses of the present thesis are bound state solutions, which correspond to three-body energies below the lowest two-body breakup threshold, $E = E_B < 0$. In this energy regime, the three-body problem reduces to an homogeneous integral equation whose non trivial solutions describe discrete bound states of the system.

Starting from the three-body Schrödinger equation with purely pairwise interactions,

$$\left(H_0 + \sum_{i=1}^{3} V_i\right)|\Psi\rangle = E|\Psi\rangle, \tag{2.27}$$

the Faddeev decomposition expresses the total wavefunction as a sum of three components:

$$|\Psi\rangle = \sum_{i=1}^{3} |\psi_i\rangle, \tag{2.28}$$

where each component $|\psi_i\rangle$ collects all processes in which the last interaction acts in the two-body subsystem complementary to particle i. Introducing the three-body resolvent $G_0(E)$, the Faddeev components satisfy the coupled set of equations:

$$|\psi_i\rangle = G_0(E)t_i(E)\sum_{j\neq i}|\psi_j\rangle. \tag{2.29}$$

In the bound state regime $E < 0$, these equations are homogeneous. Non trivial solutions exist only for discrete values of energy E, which correspond to eigenvalues of the full three-body Hamiltonian. In practice, this means finding values of E for which the integral kernel $K(E) = G_0(E)tP$ has eigenvalue 1. Physically, the absence of inhomogeneous terms reflects the fact that bound states do not require external driving and are entirely determined by the internal dynamics of the system.

The homogeneous Faddeev equations may be written schematically as:

$$\psi = K(E)\psi, \qquad K(E) \equiv G_0(E)tP \tag{2.30}$$

where P is the permutation operator, t is the two-body t-matrix embedded in the three-body space. Non trivial solutions exist only for those values of E such that:

$$\det[1 - K(E)] = 0 \tag{2.31}$$

yielding a discrete spectrum of three-body binding energies. This formulation highlights a key conceptual advantage of the Faddeev approach. Rather than attempting to solve a differential boundary value problem for the full three-body wavefunction, the bound state problem is reduced to the spectral analysis of an integral operator. The physical binding energy emerges as a property of the kernel $K(E)$, whose structure encodes the interplay between two-body correlations and three-body rearrangement processes.

From a physical and computational perspective, three-body bound states play a particularly important role in few-body nuclear physics. As the simplest non trivial many-body bound systems, they provide stringent benchmarks for models of the NN interaction and are highly sensitive to the off-shell properties of the two-body force. In particular, the binding energy of the triton has long been recognized as a key observable for testing the consistency of nuclear interaction models beyond two-body data.

From a numerical point of view, bound state calculations are also especially well suited for systematic investigations. The absence of open channels and asymptotic boundary conditions leads to a mathematically well posed eigenvalue problem, whose solutions are typically more stable and easier to control than those of the corresponding scattering equations. For this reason, bound states are often used as a testing ground for numerical implementations of the Faddeev formalism.

In this thesis, the focus on bound state solutions is therefore motivated by their physical relevance and by their suitability for numerical analysis. The three-body binding energy serves as a primary observable through which the dependence on the underlying two-body interaction is explored. This choice provides a controlled setting for the numerical methods discussed in the following chapters and for the subsequent analysis of interaction models.

2.4.4 Scattering solutions and the three-body continuum

Breakup processes

Considering a system of three particles labeled $1, 2, 3$, where particles 2 and 3 form a bound pair (the deuteron) and particle 1 is incident on this subsystem. The nuclear interaction is assumed

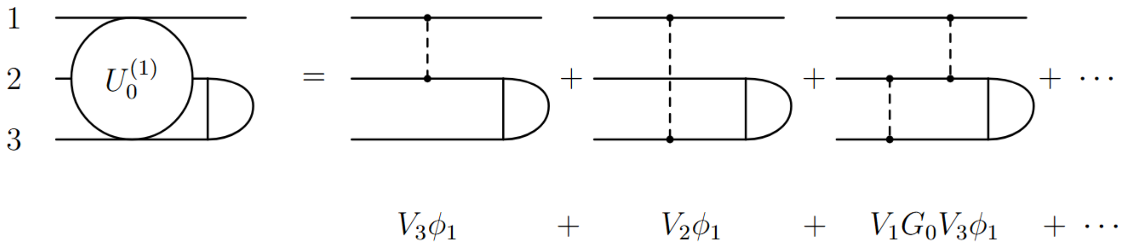

Figure 2.3: Born-Neumann series for the breakup transition operator $U_0^{(1)}$ in the partition (23), following the heuristic picture of Glöckle *et al.*. Notation: $V_{12} \equiv V_3$, etc. The free three-particle propagator between consecutive pair interactions (free Green's function) is denoted by G_0.

to be purely pairwise, so the Hamiltonian contains only two-body potentials V_{ij}. In this setting, the **breakup process** is the reaction in which all three nucleons are free in the final state. The fundamental physical picture of the breakup process (where all the 3 particles emerge free in the final state) can be introduced by writing down the Born or Neumann multiple-scattering series associated with successive pair interactions reported in fig. 2.3.

In the first step, particle 1 interacts with the pair (23) through the potential V_3. This contribution corresponds to the direct breakup term $V_3\phi_1$, where ϕ_1 denotes the initial channel state (projectile particle and bound pair).

A second class of terms arises when the interaction with particle 1 is followed by an intermediate propagation governed by the free resolvent G_0, after which a different pair interacts. For example, interaction with pair (23) followed by free propagation and subsequent interaction pair (12) yields the contribution $V_2\phi_1 + V_3G_0V_2\phi_1$. Similarly, further rescattering events generate contributions involving successively alternating pair interactions (23), (12), (13), each separated by propagation through G_0.

Each term in this series describes a sequence of pairwise collisions between the three particles, separated by free three-body propagation. However, this series is unsuitable as a basis for a scattering theory: its kernel is not compact, and the overlap between scattering channels prevents direct summation. This brings to the Faddeev decomposition, which reorganizes the series into three components.

The key idea is to associate each term in the Born-Neumann series with the last interacting pair. For example: interactions ending with pair (23) define $U^{(1)}$, interactions ending with (13) define $U^{(2)}$ and interactions ending with (12) define $U^{(3)}$. This yields the decomposition:

$$U = U^{(1)} + U^{(2)} + U^{(3)}, \tag{2.32}$$

where each Faddeev component satisfies the integral equation:

$$U^{(i)} = V_i + V_iG_0(U^{(j)} + U^{(k)}). \tag{2.33}$$

Using the t-matrices defined above in equation 2.17, it becomes:

$$U^{(i)} = t_i + t_iG_0(U^{(j)} + U^{(k)}). \tag{2.34}$$

The Born-Neumann series in fig. 2.3 contains repeated interactions in the same pair. An idea is to sum those repeated interactions to all orders for one pair at a time. This is done by using the two-body transition operator, or t-matrix (defined in equation 2.17), for each pair. For example, for the pair (23):

$$t_3 = V_3 + V_3G_0t_3. \tag{2.35}$$

Here t_3 is the two-nucleon t-matrix acting in the subspace where particles 2 and 3 interact while particle 1 is a spectator.

From the diagrammatic series for $U^{(1)}_{0,1}$ one can isolate all terms that end with a V_3 on the left and perform a resummation:

$$U^{(1)}_{0,1}\phi_1 = V_3\phi_1 + V_3G_0(U^{(1)}_{0,2} + U^{(1)}_{0,3})\phi_1 + V_3G_0V_3G_0(U^{(1)}_{0,2} + U^{(1)}_{0,3}), \tag{2.36}$$

this becomes:

$$(1 - V_3G_0)U^{(1)}_{0,1}\phi_1 = V_3\phi_1 + V_3G_0(U^{(1)}_{0,2} + U^{(1)}_{0,3})\phi_1, \tag{2.37}$$

inverting the operator $(1 - V_3G_0)$ and using the definition of t_3:

$$t_3 = V_3 + V_3G_0t_3 = V_3(1 - G_0V_3)^{-1}, \tag{2.38}$$

one obtains finally:

$$U^{(1)}_{0,1}\phi_1 = t_3\phi_1 + t_3G_0(U^{(1)}_{0,2} + U^{(1)}_{0,3})\phi_1. \tag{2.39}$$

Analogous manipulations for the other pairs give:

$$U^{(1)}_{0,2} = t_2\phi_1 + t_2G_0(U^{(1)}_{0,3} + U^{(1)}_{0,1})\phi_1, \qquad U^{(1)}_{0,3} = t_1\phi_1 + t_1G_0(U^{(1)}_{0,1} + U^{(1)}_{0,2})\phi_1. \tag{2.40}$$

Physically, the three nucleons are identical and this symmetry allows one to reduce the system to a single equation. Indeed, if one considers the permutation operator defined in equation 2.19, finds that the three breakup operators $U^{(1)}_{0,1}, U^{(1)}_{0,2}, U^{(1)}_{0,3}$ are no longer independent. In fact, one finds relations of the form:

$$U^{(1)}_{0,2} = P_{12}P_{23}U^{(1)}_{0,1}, \qquad U^{(1)}_{0,3} = P_{13}P_{23}U^{(1)}_{0,1}. \tag{2.41}$$

Now, identifying $T \equiv U^{(1)}_{0,1}$, the coupled set of three Faddeev scattering equations collapses to a single compact equation:

$$T\phi_1 = tP\phi_1 + tPG_0T\phi_1. \tag{2.42}$$

This is the basic Faddeev-like equation. It represents the sum of all diagrams that end with an interaction in the pair (23), with the effects of the other partitions recovered by P. The full breakup operator is then given by:

$$U_0 = (1 + P)T \tag{2.43}$$

which combines the three partitions corresponding to the three equivalent choices of projectile.

Elastic scattering

In contrast to breakup processes (where the final state contains three free nucleons) the elastic scattering corresponds to the framework in which the incident nucleon interacts with the deuteron and the final state remains again a bound (23) pair together with a free projectile. As before, particle 1 plays the role of the projectile, while particles 2 and 3 form the bound pair.

Following the structure employed in the breakup processes discussion, the starting point is the Faddeev component of the elastic transition amplitude associated to particle 1. From the general Faddeev decomposition of the full transition operator U, the elastic component is written as:

$$U^{(1)} = PG_0^{-1} + PtG_0U^{(1)} \tag{2.44}$$

where P is again the permutation operator acting cyclically on the three particles, and $t_1 \equiv t_{23}$ is the two-body transition t-matrix for the interacting pair (23). Iterating the equation 2.44 leads to the Born-Neumann series:

$$U^{(1)} = PG_0^{-1} + Pt_1G_0PG_0^{-1} + Pt_1G_0Pt_1G_0PG_0^{-1} + \cdots, \tag{2.45}$$

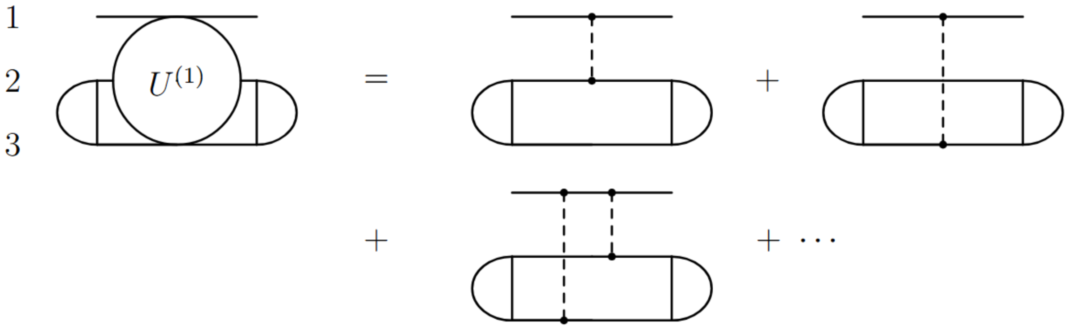

Figure 2.4: First terms in the Neumann series for the elastic transition operator $U^{(1)}$ in nucleon–deuteron scattering, following the diagrammatic representation of Glöckle *et al.* [5].

which makes explicit the physical content of elastic nucleon-deuteron scattering: the projectile interacts successively with each nucleon inside the deuteron, with free three-body propagation in between.

The structure is closely analogous to the breakup case, but here the final state is constrained to remain a bound (23) pair: diagrams containing a leading (23) interaction to the left (forming the deuteron in the final state) are allowed, while diagrams with a final breakup of particles 2 and 3 are forbidden. The first terms of this series are shown in fig. 2.4:

- the left diagram represents the full elastic operator $U^{(1)}$;
- on the right hand side, the first diagram contains a single interaction between particle 1 and 2, while particle 3 remains a spectator inside the deuteron;
- the second diagram contains instead a single interaction between particle 1 and 3;
- the third term corresponds to a double scattering: the projectile first interacts with particle 2, then with particle 3.

2.5 More about two-body interaction

In order to solve the Faddeev equations derived in the previous sections, a specific model for the two-body NN interaction must be provided. The choice of the interaction represents a fundamental physical input of the three-body problem and has a direct impact on the resulting bound state properties.

Over the years, a wide variety of interactions have been developed, differing in their physical motivation, operator structure and range of applicability. They can be broadly divided into phenomenological potentials and microscopic interactions. While both classes aim at describing low energy nuclear dynamics, they serve different purposes in few-body calculations.

2.5.1 The Malfliet–Tjon potential

While modern realistic NN potentials reproduce all partial waves and include detailed operator structures, they are often unnecessarily complicated for the purposes of benchmark three-body calculations.

For this reason, studies of the three-nucleon continuum employ simplified central model potentials, such as the **Malfiet-Tjon (MT) potential**, which has become the standard testing ground for the Faddeev theory, numerical solvers and scattering calculations.

Table 2.1: Parameter sets of the Malfliet–Tjon nucleon-nucleon potential (MT-I/III and MT-V/VI). The table reports the strengths and ranges of the repulsive and attractive Yukawa components. Reproduced from [2].

Potential	λ_A	μ_A (fm^{-1})	γ_R	μ_R (fm^{-1})	a (fm)	r (fm)	E_D (MeV)
I	2.64	1.55	7.39	3.11	−23.3	2.8	
II	0.266	0.809	0		−23.3	2.8	
III	3.22	1.55	7.39	3.11	5.45	1.8	2.23
IV	0.330	0.633	0		5.45	1.8	2.23
V	2.93	1.55	7.39	3.11	12.1	2.2	0.35
VI	0.298	0.723	0		12.1	2.2	0.35

The MT potential in coordinate space is constructed as the sum of two Yukawa interactions with opposite signs:

$$V(r) = \lambda_R \frac{e^{-\mu_R r}}{r} - \lambda_A \frac{e^{-\mu_A r}}{r}. \tag{2.46}$$

The corresponding momentum space representation:

$$V(\mathbf{k}, \mathbf{k}') = 4\pi \left[\frac{\lambda_R}{(\mathbf{k} - \mathbf{k}')^2 + \mu_R^2} - \frac{\lambda_A}{(\mathbf{k} - \mathbf{k}')^2 + \mu_A^2} \right], \tag{2.47}$$

depends only on the momentum transfer $\mathbf{q} = \mathbf{k} - \mathbf{k}'$.

Despite its simplicity, the MT potential captures the most relevant features of low-energy nuclear forces:

- a strong short-range repulsion preventing wavefunction collapse;
- an attractive well producing a deuteron bound state in the triplet channel;
- realistic S-wave phase shifts up to intermediate energies.

Table 2.1 (taken from [2]) summarizes the original MT parameter sets. Potentials I-IV refer to different singlet and triplet channels, while sets V and VI are ”averaged” potentials designed to study the effect of repulsive cores. The parameters (λ_R, μ_R) and (λ_A, μ_A) determine the shape of the repulsive and attractive components, whereas the scattering lengths a and effective ranges r_0 quantify the resulting low-energy NN behavior:

- sets II and IV are purely attractive ($\lambda_R = 0$). These interactions tend to produce excessive attraction at short distances and therefore overbind the three-nucleon system;
- sets I, III and V include a finite repulsive Yukawa term. This moderates the short-range behavior and produces much more realistic scattering lengths and triton binding energies.

The scattering length a and the effective range r quantify the low energy behavior of the S-wave NN interaction, while the deuteron binding energy E_D represents the binding energy predicted by the corresponding parameter set in the triplet channel. These observables serve as the two-body input for the subsequent three-nucleon Faddeev calculations.

Connection with the Faddeev equations

In the operator form of the Faddeev equations 2.18 the MT potential enters exclusively through the embedded two-body t-matrix $t_i(E)$, which is obtained by solving the Lippmann-Schwinger equation with $V(r)$ from 2.46. The analytic Yukawa structure produces a smooth momentum space kernel, free of hard short range singularities, ensuring good numerical stability. This is precisely the reason why with MT potential has been possible to perform the first accurate triton calculations in the 1960s.

2.6 Chiral effective field theory interactions

Chiral effective field theory (χEFT) provides a modern and systematically organized framework for the description of nuclear forces at low energies. Rather than attempting a direct treatment of quantum chromodynamics (QCD) in the non perturbative regime, χEFT exploits the separation of scales that characterizes nuclear physics, constructing an effective theory in terms of relevant low energy degrees of freedom and symmetries.

In this approach, the fundamental symmetries of QCD play a central role in constraining the form of nuclear interactions. The resulting framework allows one to derive two- and many-nucleon forces in a unified and systematically improvable manner, with a clear hierarchy of contributions organized according to a power counting scheme.

From the perspective of few-body physics, chiral EFT interactions provide a controlled connection between nuclear observables and the underlying symmetries of QCD, while at the same time offering a natural setting for uncertainty quantification and parameter estimation. These features make chiral EFT particularly well suited for the Bayesian analysis pursued in this thesis.

2.6.1 General framework of chiral EFT

χEFT is an application of the effective field theory paradigm to low energy strong interactions. Its purpose is to describe hadronic and nuclear phenomena in an energy regime where the fundamental theory of the strong interaction, QCD, is non perturbative and cannot be treated directly.

The basic idea of and effective field theory is that physical processes at low energies are insensitive to the detailed dynamics at much higher energy scales. Instead, the effects of short distance physics can be systematically encoded into a finite set of effective interaction terms, while the long distance dynamics is treated explicitly. Observables are then organized as an expansion in a small parameter that measures the ratio between the low energy scale of the process and a characteristic high energy breakdown scale.

In the case of nuclear physics, the relevant low energy degrees of freedom are nucleons and pions. Typical momenta in nuclear systems are comparable to the pion mass and are well separated from the scale associated with heavier hadronic excitations. As a result, nuclear interactions can be expanded in powers of a dimensionless parameter:

$$Q \sim \frac{p}{\Lambda_b}, \qquad Q \sim \frac{M_\pi}{\Lambda_n}, \tag{2.48}$$

where p denotes a typical nucleon momentum, M_π is the pion mass and Λ_b is the breakdown scale of the effective theory.

At any fixed order in this expansion, only a finite number of interaction terms contribute. Higher order corrections are suppressed by additional powers of Q, which provides a natural hierarchy of contributions and a systematic path toward improved accuracy. The specific form of the effective interactions, as well as the values of the corresponding low energy constants (**LECs**), is constrained by the symmetries of QCD, most notably **chiral symmetry**, which is discussed in the following subsection.

2.6.2 Chiral symmetry and its breaking

The conceptual starting point of χEFT is the approximate chiral symmetry of QCD in the light quark sector. In the limit where the up and down quark masses vanish, the QCD Lagrangian acquires an enhanced global symmetry that strongly constrains the structure of low energy strong interactions.

This symmetry becomes manifest by decomposing the quark Dirac field into its left and right handed components:

$$\psi_L = P_L\psi = \frac{1}{2}(1-\gamma_5)\psi, \qquad \psi_R = P_R\psi = \frac{1}{2}(1+\gamma_5)\psi, \tag{2.49}$$

where $P_{L,R}$ denote the chirality projection operators. In the massless case (chiral limit), the fermionic kinetic term of the QCD Lagrangian can be written as a sum of two decoupled pieces:

$$\mathcal{L}_{m=0} = i\bar{\psi}\,\partial\!\!\!/\,\psi = i\bar{\psi}_L\,\partial\!\!\!/\,\psi_L + i\bar{\psi}_R\,\partial\!\!\!/\,\psi_R, \tag{2.50}$$

which shows explicitly that left and right handed components do not mix; $\partial\!\!\!/$ is the usual shorthand for $\partial_\mu\gamma^\mu$.

Global $SU(2)_L \times SU(2)_R$ symmetry in the chiral limit

Restricting the treatment to the two light quark flavors, (u,d), in the chiral limit, the fermionic part of the QCD Lagrangian takes the form:

$$\mathcal{L}_{m=0} = i\bar{\psi}^j\,\partial\!\!\!/\,\psi^j = i\bar{\psi}^u_L\,\partial\!\!\!/\,\psi^u_L + i\bar{\psi}^d_R\,\partial\!\!\!/\,\psi^d_R. \tag{2.51}$$

The consequence of the no mixing between the two components is that the Lagrangian is invariant under independent global flavor rotations acting on ψ_L and ψ_R:

$$\psi_L \to \psi_L' = \exp\left(-i\frac{\vec{\tau}}{2}\cdot\vec{\theta}_L\right)\psi_L, \qquad \psi_R \to \psi_R' = \exp\left(-i\frac{\vec{\tau}}{2}\cdot\vec{\theta}_R\right)\psi_R, \tag{2.52}$$

where $\vec{\tau}$ are the Pauli isospin matrices and $\vec{\theta}_{R,L}$ arbitrary real parameters. These define the symmetry group $SU(2)_L \times SU(2)_R$ of the massless two flavors QCD Lagrangian (gluons are spectators under these flavor chiral rotations in this discussion).

It is often convenient to trade the left (right) rotations for vector and axial transformations:

$$\Lambda_V:\ \psi \to e^{-i\frac{\vec{\tau}}{2}\cdot\vec{\Theta}}\,\psi, \qquad \Lambda_A:\ \psi \to e^{-i\gamma_5\frac{\vec{\tau}}{2}\cdot\vec{\Theta}}\,\psi, \tag{2.53}$$

and shows that for massless fermions the Lagrangian is invariant under both. This observation explains the equivalence between the left/right formulation of the symmetry and its vector/axial representation and motivates the frequently used notation $SU(2)_V \times SU(2)_A$ for chiral symmetry in the two flavor case.

While vector transformations correspond to ordinary isospin rotations, axial transformations mix fields of opposite parity. The fact that the QCD Lagrangian in the chiral limit is invariant under both symmetries, whereas the observed hadron spectrum is not, already hints at a non trivial realization of chiral symmetry in nature. This point will become central in the discussion of spontaneous chiral symmetry breaking in the following sections.

Noether currents and charge algebra

According to Noether's theorem, every continuous global symmetry of the Lagrangian implies the existence of a conserved currents. In the chiral limit, the invariance of the QCD Lagrangian under global vector and axial transformations therefore leads to the presence of corresponding conserved currents.

For infinitesimal vector transformations, the associated Noether currents are:

$$V^a_\mu = \bar{\psi}\gamma_\mu \frac{\tau^a}{2}\psi, \tag{2.54}$$

while infinitesimal axial transformations give rise to the axial vector currents:

$$A^a_\mu = \bar{\psi}\gamma_\mu\gamma_5 \frac{\tau^a}{2}\psi. \tag{2.55}$$

In the chiral limit, both currents satisfy conservation laws:

$$\partial^\mu V^a_\mu = 0, \qquad \partial^\mu A^a_\mu = 0, \tag{2.56}$$

reflecting the exact invariance of the massless QCD Lagrangian under the corresponding symmetry transformations.

The conserved charges associated with these currents are obtained by integrating the time components of the currents over space:

$$Q^a_L(t) = \int d^3x \; \psi^\dagger_L(x,t)\frac{\tau^a}{2}\psi_L(x,t), \qquad Q^a_R(t) = \int d^3x \; \psi^\dagger_R(x,t)\frac{\tau^a}{2}\psi_R(x,t). \tag{2.57}$$

Conservation of the currents implies that these charges are time independent and, for exact symmetries, commute with the Hamiltonian of the theory.

The algebric structure of the chiral symmetry becomes manifest by evaluating the commutators among the conserved charges. One finds:

$$[Q^a_V, Q^b_V] = i\epsilon^{abc}Q^c_V, \qquad [Q^a_A, Q^b_A] = i\epsilon^{abc}Q^c_V, \qquad [Q^a_V, Q^b_A] = i\epsilon^{abc}Q^c_A, \tag{2.58}$$

which reproduces the Lie algebra of $SU(2)_L \times SU(2)_R$. The first commutator shows that the vector charges generate an $SU(2)$ algebra, which can be identified with isospin symmetry. The mixed commutator indicates that axial charges transform as vectors under isospin rotations, while the second commutator reveals that two successive axial transformations generate a vector transformation.

This structure reflects the non-Abelian nature of the chiral symmetry and highlights the special role played by the axial generator. In particular, while vector transformations correspond to well established symmetries of the hadron spectrum, axial transformations connect states of opposite parity and therefore probe the realization of chiral symmetry in the physical vacuum.

The existence of conserved axial charges in the chiral limit contrasts with the absence of parity doubling in the observed hadron spectrum. This indicates that axial symmetry cannot be realized in a manifest way in nature and must therefore be broken. Whether this breaking is explicit, spontaneous, or a combination of both is the central question addressed in the following discussion.

Explicit breaking: quark masses and partial conservation

Chiral symmetry is not exact in nature because the light quarks have small but not zero masses. The quark mass term in the QCD Lagrangian:

$$\mathcal{L}_m = -\bar{\psi}M\psi, \tag{2.59}$$

with $M = \mathrm{diag}(\mathrm{m_u}, \mathrm{m_d})$, explicitly breaks the chiral $SU(2)_L \times SU(2)_R$ symmetry. While this term is invariant under vector transformations, it mixes left and right handed components and therefore violates axial symmetry.

As a direct consequence, the conservation laws for the Noether currents are modified. The vector current remains exactly conserved:

$$\partial^\mu V^a_\mu = 0, \tag{2.60}$$

reflecting the persistence of isospin symmetry to a very good approximation. The axial current, however, is no longer conserved. Its divergence is proportional to the quark masses:

$$\partial^\mu A^a_\mu = \bar{\psi} i\gamma_5 \frac{\tau^a}{2}\{M, \psi\}. \tag{2.61}$$

In the limit of small quark masses, the axial current is therefore only approximately conserved. This property is summarized by the concept of partial conservation of the axial current (PCAC). In the two flavor case, PCAC relates the divergence of the axial current to the pion field:

$$\partial^\mu A^a_\mu \simeq f_\pi m_\pi^2 \pi^a, \tag{2.62}$$

where f_π is the pion decay constant and m_π the pion mass.

The PCAC relation expresses the fact that the axial symmetry is only weakly broken. In the limit $m_\pi \to 0$, corresponding to the exact chiral limit, the axial current becomes conserved and the pion emerges as a massless mode. The small but finite pion mass observed in nature is therefore a direct manifestation of explicit chiral symmetry breaking induced by the light quark masses.

Spontaneous symmetry breaking and Goldstone bosons

While the explicit breaking of chiral symmetry induced by the light quark masses accounts for the non vanishing pion mass, it does not explain the qualitative structure of the hadron spectrum. In particular, if chiral symmetry were realized in the Wigner-Weyl mode, one would expect hadronic states of opposite parity to appear in degenerate multiples. Such parity doubling is not observed in nature.

This observation indicates that chiral symmetry is not only explicitly broken, but also **spontaneously broken** by the QCD vacuum. In this case, the underlying Lagrangian remains invariant under chiral transformations, while the vacuum state is not. As a consequence, the axial charges do not annihilate the vacuum, even in the chiral limit.

According to Goldstone's theorem, the spontaneous breaking of a continuous global symmetry implies the existence of massless scalar excitations. In QCD with two light flavors, the breaking pattern:

$$SU(2)_L \times SU(2)_R \;\longrightarrow\; SU(2)_V \tag{2.63}$$

leads to three Goldstone bosons, which are identified with the pions.

Because chiral symmetry is also explicitly broken by the quark masses, the pions are not exactly massless, but acquire a small mass. They are therefore referred to as **pseudo Goldstone bosons**. Their mass is parametrically small compared to typical hadronic scales, reflecting the smallness of the explicit breaking relative to the scale of spontaneous symmetry breaking.

The Goldstone nature of the pions is reflected in the structure of the axial current. In the presence of spontaneous symmetry breaking, the axial current acquires a contribution proportional to the pion field:

$$A^a_\mu \;\sim\; f_\pi \partial_\mu \pi^a + \ldots, \tag{2.64}$$

so that the divergence of the axial current is directly related to pion dynamics. In the chiral limit, this relation implies the exact conservation of the axial current, while for finite quark masses it reduces to the PCAC relation discussed above.

A crucial consequence of spontaneous chiral symmetry breaking is that Goldstone bosons couple derivatively at low energies. As a result, pion interactions vanish in the non zero momentum limit and are strongly constrained by symmetry considerations. This property severely restricts the allowed form of pion-nucleon and pion-pion interactions and determines the universal long range behavior of the strong force.

In summary, the spontaneous breaking of chiral symmetry explains both the existence and the special role of the pion as the lightest hadronic degree of freedom. Together with the explicit breaking induced by the quark masses, it provides a coherent picture of low energy strong interactions in which the long range dynamics is governed by pion exchange, while short distance effects are encoded in symmetry allowed contact terms. These general principles form the conceptual foundation for the construction of chiral nuclear potentials.

2.6.3 Chiral nuclear potential

The spontaneous and explicit breaking of chiral symmetry discussed in the previous section provides the theoretical foundation for a systematic description of nuclear forces at low energies. Since pions emerge as the pseudo Goldstone bosons of the broken chiral symmetry they represent the relevant long range degrees of freedom of the nuclear interaction. At the same time, the short distance dynamics associated with heavier degrees of freedom is not resolved explicitly and must be encoded in contact interactions consistent with the symmetries of QCD.

χEFT offers a framework in which these general principles are implemented in a controlled and model independent manner. Nuclear forces are constructed as an expansion in powers of a small momentum scale over a characteristic breakdown scale, while respecting the symmetry constraints imposed by chiral symmetry.

In χEFT, the nuclear interaction is organized as a low energy expansion in powers of a generic momentum scale Q, which collectively denotes nucleon momenta or pion masses, over a breakdown scale $\Lambda_\chi \sim 1$ GeV. Observables are expressed as a systematic series:

$$V_{\mathrm{NN}} = V^{(0)} + V^{(2)} + V^{(3)} + V^{(4)} + \dots, \tag{2.65}$$

where the superscript indicates the chiral order according to Weinberg's power counting scheme.

Each term in the expansion contains all contributions consistent with the symmetries of QCD up to the corresponding order. In particular, the long range part of the interaction is generated by pion exchange diagrams, while unresolved short range physics is parametrized by contact operators with increasing number of derivatives.

2.6.4 Chiral orders and power counting

χEFT provides a systematic framework for deriving nuclear forces that is firmly rooted in the symmetries of QCD at low energies. The starting point of the approach is the construction of an effective Lagrangian that contains pions and nucleons as explicit degrees of freedom, while heavier states are integrated out. The resulting effective Lagrangian is the most general one consistent with chiral symmetry, Lorentz invariance and the discrete symmetries of QCD and can be written schematically as an infinite series:

$$\mathcal{L}_{\mathrm{eff}} = \mathcal{L}_{\pi\pi} + \mathcal{L}_{\pi N} + \mathcal{L}_{NN} + \dots, \tag{2.66}$$

where each term is organized according to an increasing number of derivatives and/or insertions of the pion mass. This structure reflects the low energy expansion underlying chiral perturbation theory and is discussed in detail in [6], [7].

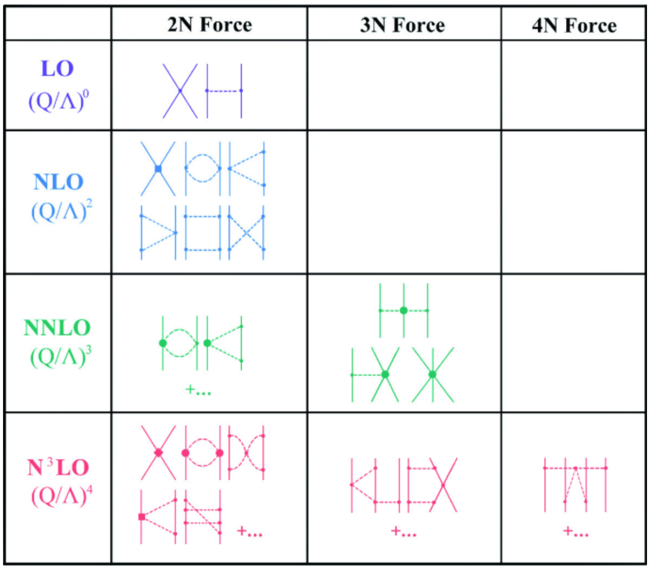

Figure 2.5: Schematic representation of the chiral expansion of nuclear forces. Two-nucleon (2N), three-nucleon (3N), and four-nucleon (4N) interactions enter at increasing orders in the chiral expansion. While two-nucleon forces contribute already at leading order, three-nucleon forces first appear at N^{2}LO, and four-nucleon forces at higher orders.

The effective theory is organized as an expansion in powers of a small dimensionless parameter Q/Λ_χ. At low energies, contributions with higher powers of Q/Λ_χ are systematically suppressed, which allows for a controlled and improvable description of nuclear interactions.

Following Weinberg's description ([8]), the effective Lagrangian is used to derive the irreducible contributions to the nuclear interaction kernel, commonly referred to as the chiral nuclear potential. Diagrams that are reducible, in the sense that they contain purely nucleonic intermediate states, are not included in the potential, but are generated through the non perturbative iteration of the potential in the Schrödinger or Lippmann-Schwinger equation. This separation is essential in nuclear systems, where shallow bound states and large scattering lengths require a non perturbative treatment already at very low energies.

The relative importance of the various contributions to the nuclear potential is determined by Weinberg's power counting scheme. For a connected, irreducible diagram with N nucleons, L pion loops and vertices of type i appearing V_i times, the chiral index ν, which determines the scaling of the diagram as Q^ν, is given by:

$$\nu = -4 + 2N + 2L + \sum_i V_i \Delta_i, \qquad \Delta_i = d_i + \frac{n_i}{2} - 2, \tag{2.67}$$

where d_i denotes the number of derivatives or pion mass insertions and n_i is the number of nucleon fields at vertex i. This expression allows one to assign a definite chiral order to each contribution to the nuclear potential. A crucial consequence of spontaneous chiral symmetry breaking is that all interaction vertices satisfy $\Delta_i \geq 0$. As a result, at any fixed order in the chiral expansion, only a finite number of diagrams contribute. This property ensures the predictive power of the theory and leads to a natural hierarchy among nuclear forces.

In particular, Weinberg power counting implies that two-nucleon forces appear already at **leading order**, while three-nucleon and four-nucleon forces appear by additional powers of Q/Λ_χ. Specifically, two-nucleon forces contribute at leading order (**LO**), three-nucleon forces first arise at **next-to-next-to leading order** (**N^{2}LO**) and four-nucleon forces enter at even higher orders. This hierarchy, which is illustrated in fig. 2.5, provides a theoretical explanation for the empirical dominance of two-body interactions in low energy nuclear systems.

At the level of practical calculations, each chiral order corresponds to a well defined structure of the nuclear potential. At LO, the two-nucleon potential consists of the long range one pion exchange interaction together with two momentum independent contact terms acting in the S-wave channels. At higher orders, additional pion exchange mechanisms and contact interactions with increasing numbers of derivatives appear, allowing for a systematic improvement of the description of NN scattering data.

In the present project, the chiral power counting provides the theoretical basis for employing chiral two-nucleon interactions as input to the three-body bound-state calculations.

2.6.5 Low energy constants in chiral nuclear forces

In χEFT, the short distance dynamics of the nuclear interaction is not resolved explicitly. Instead, it is encoded in a finite set of **low energy constants (LECs)** that multiply contact operators and sub leading pion exchange contributions in the effective Lagrangian and in the resulting nuclear potential. These constants parametrize the effects of high energy degrees of freedom that have been integrated out and cannot be predicted within the effective theory itself.

From a field theoretical perspective, the appearance of LECs is a direct consequence of the construction of the most general effective Lagrangian consistent with the symmetries of QCD. At each order in the chiral expansion, all operators allowed by these symmetries must be included. While the long range part of the interaction is dominated by pion exchange and is largely fixed by chiral symmetry, the coefficients of the contact operators are free parameters that must be determined from data.

In the two-nucleon sector, the number and structure of LECs increase with the chiral order. At LO, the NN potential contains two momentum independent contact terms that contribute in the $^1S_0$ and $^3S_1$ channels. These terms represent the dominant short range interaction at low energies. At NLO and higher, additional contact operators with increasing numbers of derivatives appear. These terms introduce momentum dependence and allow for a systematic improvement of the description of NN scattering data in higher partial waves. The associated LECs control the strength of these short range contributions and are essential for achieving quantitative agreement with experimental phase shifts.

LECs also appear in sub leading pion exchange contributions to the nuclear potential. In particular, the two-pion exchange interaction depends on LECs that enter the pion-nucleon sector of the effective Lagrangian. These constants encode information about intermediate range physics and are constrained by pion-nucleon scattering data.

The values of these LECs play a significant role in determining the strength and shape of the intermediate range part of the nuclear force and their uncertainties propagate directly to a few and many-body observables.

Since LECs cannot be calculated within the effective theory itself, they must be determined by matching to experimental data or to results from lattice QCD (lQCD). In practice, most NN LECs are obtained from fits to NN scattering phase shifts and deuteron properties at laboratory energies below the breakdown scale of the theory.

Once fixed at a given chiral order, the LECs are universal and can be used to make predictions for other observables without further adjustment, provided that calculations are performed consistently at the same order.

The presence of LECs implies that chiral nuclear interactions carry both statistical and systematic uncertainties. Statistical uncertainties arise from the fitting procedure and the experimental data used to constrain the LECs, while systematic ones are associated with the truncation of the chiral expansion at a finite order.

A key advantage of the χEFT framework is that these uncertainties can be estimated in a controlled way, based on the expected size of higher order contributions. This feature is particularly important in few-body systems, where observables such as three-body binding energies are sensitive to variations in the underlying two-body interaction.

In the present project, chiral two-nucleon interactions at different orders are employed as input to the three-body bound-state calculation. The dependence of the triton binding energy on the values of the LECs provides a direct probe of the sensitivity of few-body observables to short range physics and motivates a quantitative uncertainty analysis within a Bayesian framework.

2.6.6 Partial-wave decomposition of the NN interaction

The analysis of NN interactions is commonly performed in a **partial-wave** basis ([9]), which exploits the rotational symmetry of the two-body problem to decompose the interaction according to definite quantum numbers (L, S, J) corresponding to orbital angular momentum, total spin and total angular momentum respectively. This framework provides the natural language for both NN scattering observables and bound state properties and underlies all modern high precision NN potentials and partial-wave analyses.

In momentum space, the NN potential projected into a given partial wave takes the form:

$$V(\mathbf{k}, \mathbf{k}') \longrightarrow V_{LSJ}(k, k'), \tag{2.68}$$

where k and k' denote the magnitudes of the incoming and outgoing relative momenta. This representation allows one to study the momentum dependence of individual spin-isospin channels separately.

At low energies, only a limited number of partial waves contribute significantly to NN observables. In particular, S and P wave channels dominate the scattering amplitude below laboratory energies of approximately $300 - 350$ MeV, while higher angular momentum channels are increasingly suppressed. This hierarchy justifies the truncation of the partial-wave expansion in both phenomenological analysis and χEFT descriptions.

For spin triplet channels with total angular momentum $J > 0$ the presence of tensor components in the NN interaction induces couplings between partial waves with orbital angular momentum differing by two units. The most prominent example is the coupled ${}^3S_1$-${}^3D_1$ channel, which governs the deuteron bound state and plays a central role in few-body nuclear systems.

In this case, the interaction acquires a matrix structure in partial-wave space,

$$V_{J=1}(k, k') = \begin{pmatrix} V_{{}^3S_1-{}^3S_1}(k, k') & V_{{}^3S_1-{}^3D_1}(k, k') \\ V_{{}^3D_1-{}^3S_1}(k, k') & V_{{}^3D_1-{}^3D_1}(k, k') \end{pmatrix}, \tag{2.69}$$

reflecting the coupled channel nature of the deuteron sector.

Within χEFT short range physics is encoded in contact interactions whose LECs enter specific partial waves depending on their spin-isospin structure. As a result, variations of individual LECs primarily affect selected NN partial waves, providing a direct link between the EFT parametrization and observable two-body dynamics.

This motivates a channel by channel sensitivity analysis of the NN interaction.

In the present work the low momentum strength of a given partial wave ch is characterized by the indicator:

$$M_{\text{low}}(ch) = \max_{k,k' \leq k_{\max}} |V_{ch}(k, k')|, \tag{2.70}$$

where $k_{\max}$ is chosen within the momentum region relevant for the few-body nuclear dynamics. This definition allows one to systematically quantify how uncertainties in the two-body sector propagate toward few-body observables.

2.6.7 Operator structure of the chiral NN interaction

While the long range part of the chiral NN interaction is governed by pion exchange and largely constrained by chiral symmetry, the short range sector is encoded in contact operators whose structure reflects the most general interactions compatible with the symmetries of QCD.

At the level of the effective Lagrangian, the two-nucleon contact terms are organized in increasing power momenta. At LO, two momentum independent operators appear, contributing to the $^1S_0$ and $^3S_1$ channels. At NLO and beyond, additional derivative operators are introduced, generating momentum dependence and enabling a systematic improvement of the description of higher partial waves. The associated LECs determine the strength of these short range contributions and are fixed by fits to NN scattering data and deuteron properties, as discussed above.

From a physical perspective, it is useful to express the two-nucleon interaction in terms of its operator decomposition in spin and angular momentum space. In momentum or coordinate space, the general NN potential can be written schematically as:

$$V = V_C + V_\sigma \, \vec{\sigma}_1 \cdot \vec{\sigma}_2 + V_T \, S_{12} + V_{LS} \, \vec{L} \cdot \vec{S} + \dots, \tag{2.71}$$

where:

- V_C denotes the central component;
- V_σ multiplies the spin-spin operator $\vec{\sigma}_1 \cdot \vec{\sigma}_2$;
- V_T is associated with the tensor operator:

$$S_{12} = 3(\vec{\sigma}_1 \cdot \hat{r})(\vec{\sigma}_2 \cdot \hat{r}) - \vec{\sigma}_1 \cdot \vec{\sigma}_2; \tag{2.72}$$

- V_{LS} multiplies the spin-orbit operator $\vec{L} \cdot \vec{S}$,

with $\vec{S} = (\vec{\sigma}_1 + \vec{\sigma}_2)/2$ and $\vec{L}$ the relative orbital angular momentum.

This operator structure provides the direct connection between the underlying Lagrangian and the phenomenology observed in partial waves. In particular:

- the central spin-spin components dominate the uncoupled S-wave channels $^1S_0$ and $^3S_1$;
- the tensor operator S_{12} induces coupling between partial waves with $\Delta L = 2$, most prominently in the coupled $^3S_1$-$^3D_1$ channel that governs the deuteron bound state;
- the spin-orbit operator $\vec{L} \cdot \vec{S}$ is responsible for the splitting of triplet P-waves $^3P_0$, $^3P_1$, and $^3P_2$.

The spectroscopic notation $^{2S+1}L_J$ used in this work therefore encodes not only angular momentum quantum numbers, but also the dynamical action of specific operator structures in the NN potential.The partial-wave representation discussed in the previous section constitutes the natural framework in which these operator components manifest themselves in observable phase shifts and in the matrix elements entering few-body calculations.

This operatorial structure manifests itself in the partial-wave phase shifts, which, as an example, for the semilocal chiral interaction at $\Lambda = 450$ MeV are shown in fig. 2.6. The excellent agreement with modern partial-wave analyses demonstrates the accuracy achieved in the two-nucleon sector.

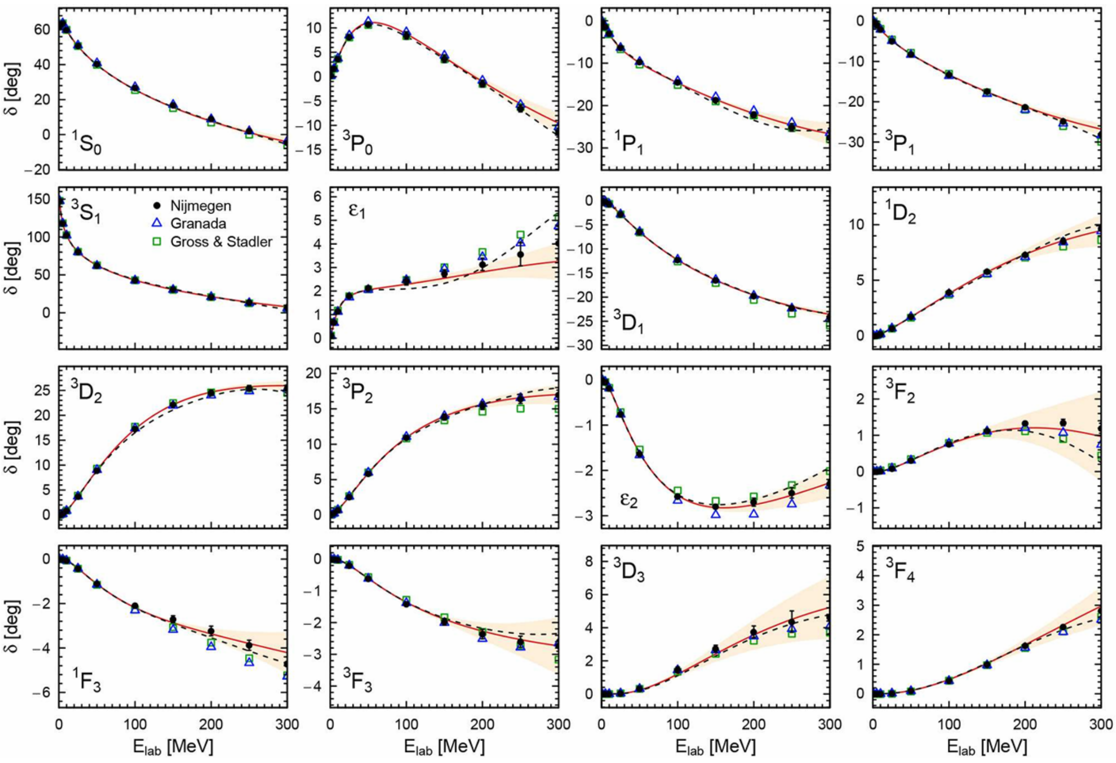

Figure 2.6: Neutron-proton phase shifts obtained with the semilocal chiral NN interaction at N^4LO^+ for the cutoff $\Lambda = 450$ MeV, compared with modern partial-wave analyses. The bands indicate the estimated truncation uncertainty. Adapted from [6].

2.6.8 Specific chiral NN interaction employed in this work

In this thesis, chiral two-nucleon interactions derived within χEFT are employed as input for the three-body calculations. The interactions are constructed following power counting and are considered at LO, NLO and N^2LO.

The nuclear force is regularized in momentum space by means of the regulator function characterized by a cutoff scale, which controls the contribution of high momentum components beyond the breakdown scale of the effective theory. In the present analysis, the cutoff is treated as a discrete model parameter and varied over a finite set of values, as detailed below.

At each order, the long range part of the interaction is given by pion exchange contributions, while unresolved short range physics is encoded in contact terms. The strengths of these contact interactions are parametrized by low energy constants (LECs), which are determined by fits of two-nucleon scattering data.

Table 2.2 summarizes the NLO contact LECs employed in the present work for the analysis of the partial-wave response of the NN interaction. The table provides a compact overview of the short range operators whose controlled variations are investigated in the NN sector. The NN partial-wave variations are implemented and analyzed using the `pyScattering` ([10]), which allows a channel resolved inspection of the NN interaction. The column of the sensitivity scale provides a qualitative estimate of the relative variation induced in the corresponding partial-wave amplitude when the associated LEC is varied within a certain range.

2.7 From theory to numerical implementation

In this chapter, the theoretical framework underlying the numerical study of three-nucleon bound states has been established. Starting from the general role of few-body systems in

Table 2.2: Overview of the NLO contact terms of the chiral NN interaction ($\Lambda = 450$ MeV), showing the partial-wave sectors they affect and the qualitative scale of their impact.

NLO contact	Partial-wave sector	Nature of effect	Sensitivity scale
$C_{^1S_0}$	$^1S_0$	central S-wave strength	$\mathcal{O}(10^{-6})$
$C_{^3P_0}$	$^3P_0$	spin-triplet P-wave	$\mathcal{O}(10^{-2})$
$C_{^1P_1}$	$^1P_1$	spin-singlet P-wave	$\mathcal{O}(10^{-2})$
$C_{^3P_1}$	$^3P_1$	spin-orbit dominated	$\mathcal{O}(10^{-2})$
$C_{^3S_1}$	$^3S_1$	central S-wave strength	$\mathcal{O}(10^{-6})$
$C_{^3P_2}$	$^3P_2$	tensor-enhanced P-wave	$\mathcal{O}(10^{-2})$
C_{SD}	$^3S_1$–$^3D_1$	S-D tensor mixing	$\mathcal{O}(10^{-3})$

nuclear physics, the formulation of three-body problem has been introduced and its solution cast in terms of the Faddeev equations. This formalism provides a rigorous and well defined starting point for the description of three-body bound and scattering states.

The structure of nuclear forces has been discussed, with particular emphasis on the distinction between phenomenological interactions and chiral effective field theory. The latter offers a systematics and symmetry-based approach to nuclear forces, with a controlled expansion in powers of a low energy scale and natural hierarchy between two, three- and many-nucleon interactions.

Within this framework, the role of low energy constants has been clarified , together with their connection to experimental data and theoretical uncertainties. These elements provide the conceptual basis for assessing the sensitivity of few-body observables to the underlying nuclear interaction.

In the present thesis, the theoretical concepts introduced in this chapter are combined with numerical implementations of the Faddeev equations. Phenomenological interactions are used as benchmarks, while chiral two-nucleon interactions at different orders are used to explore the impact of systematic improvements and parameter variations. Explicit three-nucleon forces are included and are treated as higher order effects beyond the scope of this analysis.

After the study of three-nucleon bound states, a complementary analysis of the underlying NN interaction is performed by means of a partial-wave decomposition. By projecting the NN potential into individual spin-angular-momentum channels it becomes possible to disentangle the role of specific partial waves and to interpret the sensitivity observed in few-body observables in terms of the structure of the two-body force.

Chapter 3

Numerical implementation of the Faddeev equations

The numerical solution of the three-body problem represents one of the central challenges of few-body nuclear physics. As discussed in Chapter 2, the Faddeev formalism provides a mathematically rigorous decomposition of the full wavefunction into components associated with each pairwise interaction, yielding a set of coupled integral equations whose kernel contains the free propagator and the embedded two-body transition operator. Although this formulation is exact, its practical implementation requires significant numerical sophistication: the integral kernels are highly non local, the off-shell dependence of the two-body t-matrices must be handled consistently, and the discretization of Jacobi momentum variables must guarantee both stability and convergence.

3.1 The TRIMOD implementation

3.1.1 Overview and purpose of TRIMOD

TRIMOD is the computational framework employed in this project to perform these tasks. It is a Fortran based few-body solver designed to compute the binding energy of three-nucleon systems by numerically solving the Faddeev equations in momentum space. The code implements the standard operator form:

$$|\psi_i\rangle = G_0(E)\, t_i(E) \sum_{j\neq i} |\psi_j\rangle, \tag{3.1}$$

and its symmetry reduced single-component formulation for identical particles:

$$|\psi_1\rangle = G_0(E)\, t_1(E)\, P|\psi_j\rangle, \tag{3.2}$$

where G_0 is the free three-body Green's operator and P is the permutation operator introduced in Chapter 2. This reduction is crucial for computational feasibility: instead of solving 3 coupled equations, TRIMOD needs to solve one integral equation whose kernel incorporates all cyclic permutations of the identical nucleons.

The primary purpose of TRIMOD is to compute the **triton binding energy** by solving the homogeneous Faddeev eigenvalue problem:

$$\psi = K(E)\psi, \qquad K(E) = G_0(E)tP, \tag{3.3}$$

whose non trivial solutions occur only when:

$$\det[1 - K(E)] = 0, \tag{3.4}$$

as described in Chapter 2.

In practice, the code searches for the energy $E = E_B < 0$ for which the kernel admits eigenvalue 1. This requires:

1. Construction of the Jacobi momentum grid, used to represent the Faddeev components.
2. Evaluation of the free propagator:

   $$G_0(E; p, q) = \left[E - \frac{p^2}{2\mu} - \frac{q^2}{2M} + i\epsilon\right]^{-1}, \tag{3.5}$$

   which is diagonal in the chosen basis.
3. Computation of the embedded two-body t-matrix from the Lippmann-Schwinger equation (2.17), using the momentum-space form of the chosen NN potential.
4. Assembly of the integral kernel including the transformation of Jacobi momenta under particle permutations.
5. Solution of the eigenvalue problem to extract the three-body binding energy.

The code is designed to handle different two-body nuclear interactions via modular routines. In the baseline configuration used in this project, TRIMOD employs the MT potential.

The code architecture allows, in principle, for the use of externally provided momentum-space potentials.

Within this thesis, TRIMOD plays a dual role:

1. Theoretical engine for computing the triton binding energy associated with a given set of NN interaction parameters.
2. Computational backend for the Bayesian parameter estimation presented in Chapter 4.

3.2 Numerical solution of the Faddeev equations

The numerical implementation of the bound-state Faddeev equation requires a sequence of well structured computational steps that convert the integral operator $K(E) = G_0(E)t(E)P$ into a discretized matrix acting on a finite-dimensional representation of the Faddeev component. The numerical procedure to do so can be decomposed into 5 essential stages (already introduced in the previous section): construction of Jacobi momentum grids and quadrature weights, computation of the free three-body propagator, solution of the two-body Lippmann-Schwinger equation of the off-shell t-matrix, evaluation of the three-body kernel including permutation operators and iterative extraction of the leading eigenvalue and energy search.

3.2.1 Construction of the Jacobi momentum grid

The Faddeev component $\psi(p, q)$ is represented on a two-dimensional grid in the Jacobi moment p and q. As described in 2.4.2, these variables parametrize respectively the internal motion of the interacting pair and the motion of the spectator relative to the pair.

In TRIMOD these grids are constructed in `main.f90` using the auxiliary routine `gauss` from the module `trimod_sub`, which itself calls `gauleg` from the module `nr_sub`.

The subroutine `gauss` determines n quadrature points $x(i)$ and associated weights $w_x(i)$ on the interval $[a, c]$, with a clustering controlled by the middle point b. Internally `gauss`:

1. calls `gauleg(-1,1,gp,gw)` to obtain standard Gauss-Legendre nodes g_p and weights g_w on $[-1,1]$;
2. maps these nodes to the physical interval $[a,c]$ through a rational transformation that symmetrically distributes half of the points on each side of b;
3. computes the corresponding weights $w_x(i)$ such that the quadrature remains exact for polynomials up to degree $2n-1$.

This mechanism is used to generate both the **spectator momentum grid** and the **pair momentum grid**:

- **q-grid**: provides n_q points $q(i) \in [0, q_{max}]$ with enhanced resolution around q_0.
- **p-grid**: the pair momentum is constructed in two pieces which generate a dense grid in the low and intermediate momentum region $[0, p_{max}]$ and a separate grid in the high momentum interval $[p_{max}, p_{cut}]$.These are then merged into the full array `p(1:nptot)` with $p = 0$ and the remaining points taken from `aux1/aux4` and weights from `aux3/aux6`. The first point is exactly $p = 0$ with vanishing weight, which simplifies the treatment of the kernel at the origin.

The resulting grids are non uniform Gauss-Legendre type quadrature, tailored to resolve the low momentum structure of the kernel while keeping the total number of points manageable.

Implementation details and representative code excerpts for the construction of the Jacobi momentum grids are reported in appendix A.1.

Spline-based representation of permutation integrals

The action of the permutation operator P in the kernel G_0tP requires evaluating the Faddeev component at transformed Jacobi momenta, corresponding to different choices of interacting pair and spectator. The analytic relations between the old and new Jacobi coordinates are derived in 2.4.2, but their numerical implementation requires efficient interpolation on the p-grid.

TRIMOD addresses this by computing cubic spline basis functions in the module `interpolation`. The routine `spline` receives the momentum grids and weights and returns:

- an angular quadrature grid `x(1:nx)` and weights `wx(1:nx)` in the interval $[-1, 1]$;
- two four-dimensional arrays `s1(ix,ip,iqp,iq)` and `s2(ix,ip,iqp,iq)` containing spline coefficients.

Inside `spline` helper procedures (among them `selem`) compute cubic spline polynomials on the p-grid. The expression for `spl(j)` shows explicitly that spline is a polynomial of degree three in the local variable dx, with precomputed coefficients `fak1`, `fak2`, `fak3`. The arrays `s1` and `s2` then encode the values of these spline basis functions at the transformed momenta that arise when changing from one Jacobi partition to another.

Later, in the application of the kernel (see below), TRIMOD uses these precomputed spline elements to approximate integrals over the intermediate momentum p' and the angle between the Jacobi vectors. The double sum found in `main.f90` corresponds precisely to a Gaussian quadrature over the cosine of the angle, combined with the cubic spline interpolation of $\psi(p', q')$ at the transformed momenta.

Implementation details of the spline construction and of the numerical evaluation of the permutation operator are reported in appendix A.2.

3.2.2 Two-body t-matrix

The two-body transition operator is computed in the subroutine `tmat` of `m_trimod_sub.f90`. For a given energy e and momentum grid $\{p_i\}$, the routine receives the potential matrix $v_{ij} = V(p_i, p_j)$ and returns the off-shell t-matrix $t_{ij}(e)$.

Formally, the Lippmann-Schwinger equation 2.17 can be written, after discretization of the intermediate momentum, as an algebric system:

$$At = V, \tag{3.6}$$

where A is a matrix that approximates the operator $1 - VG_0$. TRIMOD follows exactly this strategy: `tmat` constructs a matrix `akern` (the discrete analog of A) and then solves the linear system above using the LAPACK driver routine `dgesv`. The call of `dgesv` performs an LU decomposition of `akern` with partial pivoting and row interchanges, and overwrites `vv` (initially a copy of `v`) with the solution, which is assigned to the output `t`. LAPACK is a widely used library for numerical linear algebra; using `dgesv` ensures a robust and efficient computation of the off-shell t-matrix.

The potential matrix itself is generated in the subroutine `pot`.

Iterative Faddeev solver and energy search

Once the grids, spline coefficients, potential and t-matrix are available, TRIMOD proceeds to solve the homogeneous Faddeev equation by power iterations on the kernel $K(E)$ and to locate the binding energy by a simple secant type search.

Implementation details of the two-body t-matrix construction are reported in appendix A.3.

Vector iteration

For a fixed energy $E = e(\text{ie})$, the code first computes the off-shell t-matrix for all spectator momenta. The iterations then start from the constant trial vector and repeatedly applies the discretized kernel to obtain a new vector `x2`.

Convergence of the power iteration is monitored through the stabilization of the leading eigenvalue of the kernel. Once convergence is achieved, this eigenvalue provides an estimate of $\eta(E)$ at the trial energy.

Energy search

The binding energy is located by searching for the zero of:

$$\text{eig}(E) = \eta(E) - 1 \tag{3.7}$$

The energy loop is bounded by `iemax`, and the search is stopped as soon as $|\text{eig}(E)| < 10^{-6}$, at which point the corresponding value fo `emev = e(ie)*hbarc/mf` is printed as the three-body binding energy.

Implementation details of the iterative solver and of the energy-search algorithm are reported in appendix A.4.

3.2.3 Input parameters and potential definition

The TRIMOD code requires a set of numerical and physical parameters that define both the discretization of the three-body Hilbert space and the form of the underlying two-body interaction. These inputs determine the resolution, stability and convergence properties of the numerical solution described in 3.2.

Momentum-space discretization parameters

The discretizations of the three-body problem is performed in Jacobi momentum-space, where the Faddeev component $\psi(p,q)$ depends on the pair relative momentum p and the spectator momentum q. The continuous integral equations are replaced by finite sums through Gaussian quadrature, requiring the specification of discrete momentum grids and associated weights.

The spectator momentum grid is characterized by:

- n_q: total number of quadrature points, which controls the resolution of the spectator degree of freedom;
- q_{max}: maximum spectator momentum included in calculation, which defines the upper bound of the integration domain;
- q_0: internal reference point used in the construction of the quadrature grid to enhance resolution in the low momentum region.

Similarly, the discretizations of the pair momentum p is defined through:

- n_{p1}, n_{p2}: number of quadrature points used in the low and high momentum regions respectively;
- p_0, p_{max}, p_{cut}: momentum parameters specifying the structure and extension of the pair momentum grid.

The combination of these parameters determines the total number of grid points used for the representation of the Faddeev component $\psi(p,q)$. As discussed in 3.2, the grids are constructed using Gaussian quadrature, and the associated weights are used consistently in all momentum integrations.

The angular integration required for the permutation operator is controlled by n_x, which is the number of quadrature points for the cosine of the angle between Jacobi momentum vectors. This parameter determines the accuracy of the angular integration entering the permutation contributions and influences the convergence of the kernel application.

Energy parameters and iteration control

The three-body binding energy is determined through an iterative eigenvalue search in the negative energy region. This procedure requires the specification of a set of numerical parameters controlling the energy scan and the convergence of the iteration at fixed energy. The relevant inputs include:

- an initial trial energy $E_0 < 0$, chosen within a physically reasonable range below the breakup threshold;
- an energy step ΔE, used to guide the exploration of the energy domain when searching for eigenvalue condition;
- a maximum number of iterations allowed in the eigenvalue solver at fixed energy;
- tolerance parameters defining the stopping criteria of the iterative procedure.

In the original implementation of TRIMOD, these controls are deliberately kept simple. The energy search and convergence checks are designed to provide reliable results for benchmark calculations rather than to achieve optimal performance or global error control.

Definition of the two-body interaction

The physical input to the three-body calculation is provided by a NN interaction entering the Lippmann-Schwinger equation for the two-body transition operator. TRIMOD supports interaction models supplied in momentum-space and discretized consistently with the momentum grid used in the calculation.

Phenomenological potential

In its baseline configuration, TRIMOD employs a phenomenological NN interaction of Malfliet–Tjon type, which has been widely used as a benchmark in three–body bound–state calculations. The interaction is defined in coordinate space as a superposition of repulsive and attractive Yukawa components with different ranges.

The MT interaction is characterized by a small set of parameters controlling the strength and the range of its repulsive and attractive components. These parameters, conventionally denoted by $v_0^{(i)}$ and $a^{(i)}$, determine the relative weight and spatial range of each Yukawa term and fully specify the two–body interaction employed in the calculation.

In TRIMOD, these parameters are treated as external inputs and enter the computation exclusively through the momentum–space interaction kernel used in the discretized Lippmann–Schwinger equation.

The MT potential is not intended to provide a high precision description of experimental NN data. Instead, its role in TRIMOD is to furnish a well behaved interaction kernel that is free of short range singularities and exhibits smooth momentum-space behavior. These properties make it particularly suitable for testing the numerical solution of the Lippmann-Schwinger and Faddeev equations and for studying convergence with respect to discretization parameters.

In the numerical implementation, the interaction enters exclusively through its momentum-space matrix elements, which are provided on the discretized momentum grid and used directly in the construction of the two-body transition operator.

Physical units and constants

Al calculations performed by TRIMOD are expressed in natural units commonly used in nuclear few-body physics. Physical constants such as the nucleon mass and the factor $\hbar c$ are defined internally and applied consistently in the definition of kinetic energy, Jacobi coordinates and energy conversions.

3.3 The TRITON implementation

In order to extend the three-body analysis beyond phenomenological interactions, a second numerical implementation, referred to as TRITON, has been employed. The introduction of TRITON is motivated by the necessity of treating **chiral effective field theory** (χEFT) **NN interactions**, whose operator structure, regulator dependence, and order by order construction differ substantially from the phenomenological potentials used in TRIMOD.

From a theoretical point of view, TRITON solves the same homogeneous Faddeev equation discussed in the previous sections. The bound-state problem is formulated in momentum space and consists in finding non trivial solutions of:

$$|\psi\rangle = G_0(E)t(E)P|\psi\rangle. \tag{3.8}$$

The triton binding energy corresponds to the value of the total energy $E < 0$ for which the leading eigenvalue of the kernel equals unity.

The main distinction between TRIMOD and TRITON does not lie in the normal structure of the three-body equation, but in the construction of the two-body input and in the size and complexity of the coupled-channel space required for a realistic description of the triton.

3.3.1 Chiral two-body interaction input

In TRITON, the NN interaction is supplied through a dedicated Fortran library implementing chiral effective field theory interactions in momentum space. The routines are contained in the file `ichiral.f90`, which provides momentum space partial-wave matrix elements of chiral NN potentials up to N^{4}LO.

The central interface routine

```
SUBROUTINE CHIRALMOMPWD(OSTAT,FORCE,PPUN1,PPUN2,JMOM,CUTNUMR,POTEN)
```

computes the momentum-space matrix elements:

$$\langle p', l', s, j | V | p, l, s, j \rangle \tag{3.9}$$

for fixed total angular momentum j, where the magnitudes of the incoming and outgoing relative momenta p and p' are provided in physical units (GeV).

The interaction model is selected by an integer flag `FORCE`, allowing the use of different NN potentials, including chiral N^{4}LO interactions with different regulator choices. The regulator dependence enters explicitly through the parameter `CUTNUMR`, which selects among predefined cutoff values in the chiral interaction library.

From the perspective of the three-body solver, the two-body interaction is therefore provided exclusively through partial-wave projected momentum-space matrix elements, consistently with the formulation of the Lippmann-Schwinger equation in a partial-wave basis [4].

3.3.2 Two-body transition operator

For each two-body partial-wave, the corresponding off-shell transition operator is obtained by solving the LS equation on the discretized momentum grid. As in standard momentum-space Faddeev calculations, the integral equation is reduced to a linear algebra problem after Gaussian quadrature discretization.

The discretized equation is solved independently in each two-body channel, and the resulting t-matrix elements are stored and later embedded into the three-body kernel. This channel by channel construction is explicitly visible in the TRITON workflow implemented in `m_triton_sub.f90`, where the two-body input is treated as diagonal in the total angular momentum j but contributes to channel coupling once embedded into the three-body Hilbert space.

3.3.3 Coupled-channel Faddeev equations

In contrast to the single-channel implementation employed in TRIMOD, TRITON solves the Faddeev equation in a coupled-channel partial-wave basis. Each Faddeev component is labeled by a collective channel index α, representing a specific set of orbital angular momenta, spins, total angular momentum, and isospin quantum numbers for the three nucleon system.

The bound-state Faddeev equations thus take the standard coupled-channel form [4]:

$$\psi_\alpha(p, q) = \sum_{\alpha'} \int dp', p'^2 \int dq', q'^2; K_{\alpha\alpha'}(p, q; p', q'; E), \psi_{\alpha'}(p', q'), \tag{3.10}$$

where the kernel $K_{\alpha\alpha'}$ contains the free three-body propagator, the two-body transition operator embedded in the three-body space and the permutation operator.

After discretization of the Jacobi momenta (p, q) by Gaussian quadrature, the integral equation is mapped to a matrix eigenvalue problem:

$$\boldsymbol{\psi}(E) = \mathbf{K}(E), \boldsymbol{\psi}(E), \tag{3.11}$$

where $\boldsymbol{\psi}$ collects all discretized channel amplitudes. As in the standard Faddeev formalism, the triton binding energy corresponds to the value of $E < 0$ for which the largest eigenvalue $\mathbf{K}(E)$ equals unity.

3.3.4 Permutation operator and momentum interpolation

The action of the permutation operator in the partial-wave basis induces both momentum transformations and channel mixing. The momentum-space part of the permutation operator requires evaluating the Faddeev amplitudes at transformed Jacobi momenta (p', q') and integrating over the angle between Jacobi vectors.

In TRITON, this operator is implemented numerically using Gaussian quadrature for the angular integration and spline based interpolation on the discretized momentum grids. The interpolation machinery is provided by the module `m_interpolation.f90`, which constructs cubic spline representations of the Faddeev amplitudes on the pair momentum grid. This strategy is fully analogous to that employed in established momentum-space Faddeev solvers and ensures stable numerical evaluation of the permutation contributions.

Channel recoupling induced by particle exchange is handled explicitly in the kernel construction routines in `m_triton_sub.f90`, where the permutation operator connects different channel indices α according to the angular momentum and spins coupling structure of the three nucleon system.

3.3.5 Channel-space truncation

In practical calculations, the partial-wave expansion must be truncated to a finite number of channels.

In the present TRITON implementation, the maximum number of channels is fixed by the parameter:

```
nchmax = 66,
```

which determines the dimension of the coupled-channel system. All channels are treated on equal footing, and no additional truncation of the channel space is introduced beyond this fixed cutoff. This truncation is an explicit implementation choice and can be systematically tested by varying the channel cutoff.

3.4 Computational setup for the NN partial-wave sensitivity analysis

The numerical analysis of the NN interaction in partial-wave representation is based on a dedicated computational framework combining Fortran routines implementing chiral NN potentials with Python scripts for data handling, automation and post processing. This hybrid approach allows for efficient evaluations of the NN interaction kernels while retaining flexibility in the exploration of parameter variations and diagnostic analyses.

The core of the computation is provided by Fortran routines based on the publicly available `pyScattering` code [10]. These modules implement the chiral NN interaction at fixed cutoff and chiral order and evaluate the momentum space NN potential and return its matrix elements projected into individual partial waves.

These routines have been interfaced with custom Python scripts written for the present thesis in order to automate the generations of NN potential matrices, the systematic variation of LECs and the extraction of diagnostic quantities. In particular, controlled multiplicative variations of individual contact terms are applied directly at the level of the NN interaction and the resulting partial-wave matrices are recomputed for each parameter choice.

The NN potential is evaluated on a discrete momentum grid and stored in matrix form for each partial wave. Since few-body bound states are dominated by low momentum components, the subsequent analysis focuses on a restricted momentum region $k, k' \leq k_{\text{max}}$, chosen to be representative of the momentum scales relevant for the deuteron and triton. This restriction provides a robust and physically motivated range for the sensitivity analysis.

The numerical framework described here serves as a diagnostic tool designed to interpret the sensitivity of few-body observables in terms of the underlying structure of the two-body interaction. Within this scope, the code provides a controlled and transparent link between variations of EFT parameters and their manifestation in specific NN partial waves.

Chapter 4

Bayesian framework

4.1 Bayesian inference: basic principles

Bayesian inference provides a framework for statistical reasoning, particularly well suited for problems in which theoretical models, numerical approximations and experimental data must be combined in an unified way. Its core is **conditional probability**, from which **Bayes' theorem** naturally follows. This approach originates from the work of Thomas Bayes and has become a cornerstone of modern statistics, particularly in fields where information is incomplete, noisy or indirect (such as nuclear physics).

4.1.1 Bayes' theorem

The foundation of Bayes statistics is conditional probability: the probability of an event A given that another event B is known to occur. In [11] is explained that the entire edifice of Bayes' theorem originates from three basic relationships between **conjunction** and **conditional probability**.

Given events A and B:

$$P(A|B) = \frac{P(A \text{ and } B)}{P(B)}, \tag{4.1}$$

which is presented as **theorem 1** and says that the probability of A happening given that B has happened is the fraction of the probability mass of B that also belongs to A. In practice one restricts his attention to situations where B is true and asks how many of these situations also satisfy A.

Rearranging terms yields **theorem 2**, the second relationship:

$$P(A \text{ and } B) = P(B)P(A|B). \tag{4.2}$$

Since logically the conjunction is symmetric, so:

$$A \text{ and } B = B \text{ and } A, \tag{4.3}$$

this means that $P(A \text{ and } B) = P(B \text{ and } A)$ and so:

$$P(B)P(A|B) = P(A)P(B|A). \tag{4.4}$$

Solving for $P(A|B)$ gives the **Bayes' theorem** (**theorem 3** in [11]):

$$P(A|B) = \frac{P(B|A)P(A)}{P(B)}, \tag{4.5}$$

where:

- A is the hypothesis whose probability may be affected by data observed (evidence). There are often competing hypothesis, and the objective is to determine which one is the most probable;
- $P(A)$ is the **prior probability**: the estimate of the probability of the hypothesis A before the event B is observed;
- B is the event and corresponds to new data that were not used in computing the prior probability;
- $P(A|B)$ is the **posterior probability**: probability that A happens after B is observed;
- $P(B|A)$ is the **likelihood**: probability of observing B given H. It indicates the compatibility of the event with the given hypothesis;

To compute the denominator $P(B)$ in equations 4.5 is used the **law of total probability**:

$$P(B) = \sum_i P(H_i)P(B|H_i), \tag{4.6}$$

where the hypothesis H_i are mutually exclusive and exhaustive. This theorem states that the probability of observing data B is obtained by considering every possible underlying cause H_i weighting each by its probability.

To sum up, Bayes inference is a process of **updating beliefs**: the prior expresses what we consider plausible before observing data, the likelihood expresses how compatible the observed data are with each hypothesis and the posterior is the result of combining these two elements. Each new dataset can be incorporated sequentially, with the posterior becoming the new prior.

In the context of few-body nuclear physics, Bayesian inference provides a natural framework to quantify theoretical uncertainties associated with model assumptions, regulator choices and truncation effects in effective field theories.Rather than selecting a single interaction model or cutoff prescription, the Bayesian approach allows one to treat these choices as sources of uncertainty and to propagate them consistently to the predicted observables.

In this work, Bayesian inference is employed to combine triton binding energy predictions obtained at different chiral orders and regulator cutoffs, and to assess their relative statistical weight given the experimental binding energy.

4.2 Likelihood function for binding energy data

The likelihood function is the central component of Bayesian inference: it quantifies how probable the observed data are assuming that a given set of physical parameters is correct. In the present work, the data consist of the experimental binding energy of the triton while the theoretical prediction is obtained from the numerical solution of the three-body Faddeev equations using the TRITON/TRIMOD framework.

Let E_{exp} denote the experimental value of the triton binding energy and $E_{\text{th}}(\theta)$ the corresponding theoretical prediction obtained for a given set of parameters θ. In this analysis the parameter vector θ may include the regulator cutoff, selected low energy constants or effective model labels such as the chiral order. The likelihood function is defined as the conditional probability of observing the experimental value given the theoretical prediction:

$$\mathcal{L}(\theta) \equiv P(E_{\text{exp}}|\theta). \tag{4.7}$$

Following standard practice in Bayesian analyses of nuclear observables ([12]) the experimental and theoretical uncertainties are modeled by a Gaussian distribution. Under this assumption, the likelihood takes the form:

$$P(E_{\text{exp}}|\theta) = \frac{1}{\sqrt{2\pi\sigma^2}}\exp\big[-\frac{(E_{\text{th}}(\theta) - E_{\text{exp}})^2}{2\sigma^2}\big], \tag{4.8}$$

where σ represents the total uncertainty associated with the comparison between theory and experiment.

In the context of this project, σ is interpreted as an effective uncertainty that incorporates multiple sources of error. These include the experimental uncertainty on the triton binding energy as well as theoretical uncertainties arising from the truncation of the chiral expansion, the omission of three-nucleon forces and residual regulator dependence at finite chiral order.

The use of a Gaussian likelihood reflects the assumption that deviations between theory and experiment are smooth and symmetric around the optimal parameter values and that no systematic bias is present within the explored parameter range. This choice is consistent with the observed smooth and monotonic dependence of the triton binding energy on both interaction parameters and regulator choices, as demonstrated in the numerical results in the next chapters.

4.3 Prior distributions

In a Bayesian framework, the specification of prior distributions encodes the available information on the model parameters before confronting them with the data collected. In the present analysis, different classes of parameters are present:

1. LECs of the two-nucleon interaction;
2. regulator (cutoff) values;
3. discrete model choices, such as the chiral order of the interaction.

Each of these is assigned a prior distribution consistent with its physical interpretation and with the scope of the present study.

Priors on LECs

The LECs entering the nuclear interaction are treated as continuous parameters. In this project, the analysis focuses on *local sensitivity* and *parameter exploration* around reference values taken from established fits or benchmark interactions. For this reason, the priors on the LECs are chosen to be uniform within finite intervals around their baseline values:

$$C_i \in [C_i^{(0)}(1-\delta), C_i^{(0)}(1+\delta)], \tag{4.9}$$

where $C_i^{(0)}$ denotes the reference value of the LEC and δ is a small relative variation.

This choice reflects the absence of prior constraints within the narrow exploration range and ensures that all parameter values within this interval are treated on equal footing. The resulting prior density for each LEC is therefore:

$$P(C_i) = \begin{cases} \text{const.}, & C_i \in [C_i^{\min}, C_i^{\max}] \\ 0, & \text{otherwise.} \end{cases} \tag{4.10}$$

Such uniform priors are commonly adopted in Bayesian sensitivity analyses when the goal is to quantify the response of observables to controlled parameter variations, rather than to perform a full global refit of the interaction.

Priors on regulator cutoff values

The regulator cutoff R is treated as a discrete model parameter. In the present work, a finite set of cutoff values is considered:

$$R \in \{R_1, R_2, \dots, R_N\}, \tag{4.11}$$

corresponding to the regulator choices implemented in the numerical calculations.

Since no cutoff value is a prior preferred within the considered range, a uniform discrete prior is assigned:

$$P(R_i) = \frac{1}{N}, \qquad i = 1, \dots, N. \tag{4.12}$$

Priors on chiral orders

When comparing calculations performed at different chiral orders (LO, NLO, N^2LO) the chiral order itself is treated as a discrete model index. In the absence of additional information favoring one order over another, a uniform prior is assigned:

$$P(LO) = P(NLO) = P(N^2LO). \tag{4.13}$$

This conservative choice ensures that differences in posterior weights arise only from the likelihood, so from the agreement between the predicted binding energies and the reference data rather than from subjective model preference.

4.4 Posterior distribution

Given the likelihood function introduced in section 4.2 and the prior distributions discussed in section 4.3, the posterior probability distribution for the model parameters θ is obtained via Bayes' theorem:

$$P(\theta|\mathcal{D}) = \frac{P(\mathcal{D}|\theta)P(\theta)}{P(\mathcal{D})}, \tag{4.14}$$

where $\mathcal{D}$ denotes the binding energy data and $P(\mathcal{D})$ is the evidence.

In this project, the parameter vector θ can represent:

- a set of LECs;
- a discrete regulator cutoff value;
- a discrete model choice, such as the chiral order of the interaction.

Log-posterior formulation

For numerical stability and convenience, the posterior is evaluated in logarithmic form. Assuming a Gaussian likelihood for the binding energy, the log-posterior:

$$\log P(\theta|\mathcal{D}) = -\frac{[E_3(\theta) - E_{\mathrm{ref}}]^2}{2\sigma^2} + \log P(\theta) + \text{const.}, \tag{4.15}$$

where $E_3(\theta)$ is the triton binding energy predicted by the Faddeev solver for a given parameter set, E_{ref} is the reference value and σ encodes the adopted uncertainty.

Discrete posterior normalization

In several parts of this work, the parameter space is explored on a finite discrete set, for example:

- grids of potential parameters,
- discrete regulator cutoff values,
- discrete chiral orders.

In such cases, the posterior probability is normalized explicitly by summation:

$$P(\theta_i|\mathcal{D}) = \frac{\exp[\log P(\theta_i|\mathcal{D})]}{\sum_j \exp[\log P(\theta_j|\mathcal{D})]}. \tag{4.16}$$

This discrete normalization is used throughout the numerical analysis to compute posterior weights, expectation values and variances of the triton binding energy.

Posterior expectations and uncertainties

Posterior distributions are summarized through expectation values and variances of observables. For a generic observable $O(\theta)$ the posterior mean is given by:

$$\langle O \rangle = \sum_i O(\theta_i) P(\theta_i|\mathcal{D}), \tag{4.17}$$

with an associated posterior variance:

$$\mathrm{Var}(O) = \sum_i [O(\theta_i) - \langle O \rangle]^2 P(\theta_i|\mathcal{D}). \tag{4.18}$$

In this project, these expressions are used to compute posterior estimates of the triton binding energy at fixed chiral order, as well as after marginalization over regulator cutoff values and model choices.

Bayesian model averaging

When multiple model variants are considered, such as different cutoffs or different chiral orders, Bayesian model averaging (BMA) provides a principled way to combine their predictions. The posterior distribution for the observable is obtained by marginalizing over the model index M:

$$P(E_3|\mathcal{D}) = \sum_M P(E_3|M, \mathcal{D}) P(M|\mathcal{D}), \tag{4.19}$$

where $P(M|\mathcal{D})$ is the posterior probability of model M.

4.5 Summary of the Bayesian framework and scope of the analysis

In this chapter has been introduced a Bayesian framework with the scope of analyze the dependence of the triton binding energy on nuclear interaction parameters and model choices. The approach is deliberately tailored to the numerical structure of the problem and to the finite set calculations performed with the Faddeev solvers described in chapter 3.

The likelihood function is constructed from the deviation between the triton binding energy predicted by the three-body calculation and a chosen reference value, assuming a Gaussian error model. This choice provides a simple and transparent way to rank parameter sets and model variants according to their agreement with the reference observable, without introducing additional phenomenological assumptions.

Prior distributions are chosen to be weakly informative and consistent with the numerical strategy adopted in the project. Uniform priors are implicitly implemented for the LECs through uniform parameter scans on finite intervals, while discrete uniform priors are assigned to regulator cutoff values and chiral orders. As a result, posterior probabilities are entirely driven by the likelihood and reflect the numerical behavior of the Faddeev solutions.

Since all analyses are performed on finite discrete parameter spaces, posterior distributions are evaluated through explicit summation rather than continuous integration. Posterior expectations, variances and model weights are computed as weighted sums over the explored parameter grids. This discrete formulation allows Bayesian inference to be applied consistently without resorting to stochastic sampling methods.

In the following chapters, this framework is applied to benchmark calculations with phenomenological interactions and to chiral effective field theory potentials at different orders. The Bayesian formulation provides a unifying language for comparing results, quantifying uncertainties and interpreting systematic trends observed in the numerical solutions of the Faddeev equations.

Chapter 5

Results

5.1 Overview of the numerical setup

The results presented in this chapter are obtained from the solution of the three-body bound-state problem within the Faddeev formalism, using the numerical implementation described in Chapter 3.

The triton binding energy is extracted by solving the homogeneous Faddeev equation in momentum space and searching for the value of the total energy at which the leading eigenvalue of the Faddeev kernel equals unity. The calculation is performed using the Jacobi momentum coordinates and Gaussian quadrature techniques, with non uniform momentum grids chosen to accurately resolve the low momentum region relevant for bound-state dynamics.

Two numerical frameworks are used. The code TRIMOD is used to perform benchmark calculations with phenomenological two-nucleon interactions, providing a controlled environment for testing numerical stability and convergence. The code TRITON is used to perform calculations with chiral two-nucleon interactions, allowing for a systematic investigation of the dependence of three-body observables on the order of the chiral expansion and on the values of the low energy constants.

All calculations are performed with fixed momentum space discretization parameters that have been verified to yield stable results for the binding energy. The numerical grids and quadrature orders are kept constant when comparing different interaction models, in order to isolate purely physical effects from numerical artifacts.

Only two-nucleon interactions are explicitly included. Chiral two-nucleon potentials at LO and NLO are considered.

The results are presented in terms of binding energies, convergence trends and parameter sensitivities. where appropriate, comparisons between different interaction models are performed to asses the robustness of the numerical solution and the impact of systematic improvements in the nuclear force. These results form the basis for the uncertainty analysis and Bayesian parameter inference discussed in the following.

5.2 Benchmark calculations with the MT potential

As a first step in the analysis, benchmark calculations are performed using the MT phenomenological two-nucleon potential. The purpose of this study is twofold. On the one hand, it provides a stringent validation of the numerical solution of the Faddeev equations implemented in TRIMOD. On the other hand, it serves as a controlled environment to test the Bayesian analysis framework developed in this thesis before applying it to chiral nuclear interactions.

The MT potential is particularly well suited for this purpose due to its simple functional form

Table 5.1: Representative parameter sets of the Malfliet-Tjon potential explored in the benchmark study and corresponding triton binding energies. The entry labeled PM (posterior maximum) corresponds to the parameter set that maximizes the posterior probability distribution obtained from the Bayesian analysis.

Set	$v_0^{(1)}$ [MeV]	$v_0^{(2)}$ [MeV]	a_R [fm^{-1}]	E_3 [MeV]
A	-574	1422	1.55	-8.82
B	-573	1425	1.55	-8.52
C	-572	1422	1.55	-8.47
D	-571	1422	1.55	-8.30
PM	-572	1422	1.55	-8.47

and its widespread use as a test interaction in three-body bound-state calculations. Although it is not intended to represent a realistic description of the NN force, it reproduces qualitatively the binding properties of light nuclei and allows for transparent numerical diagnostics.

5.2.1 Numerical setup and execution strategy

The triton binding energy is computed by solving the homogeneous Faddeev equation in momentum space using the TRIMOD code. The code is interfaced with a Python based runner, which automates the generation of input files, the execution of the Fortran solver and the parsing of the output binding energy.

The MT interaction is characterized by a small set of parameters entering the short range repulsive and intermediate range attractive components of the potential. These parameters are treated as continuous variables and are explored through systematic parameter scans. For each parameter set, the Faddeev equation is solved numerically and the corresponding three-body binding energy is extracted.

Table 5.1 summarizes a representative set of MT parameter configurations explored in this benchmark study, together with the corresponding binding energies obtained from coarse scans over broad ranges as well as refined scans in the vicinity of the experimental binding energy. The resulting binding energies span a range that includes the experimental value of the triton binding energy, which is $E_3^{\mathrm{exp}} = -8.48$ MeV.

The dependence of the binding energy on the MT potential parameters is found to be smooth and monotonic in the explored region of parameter space. No numerical instabilities or irregular behavior are observed, indicating that the discretization of the momentum space integrals and the iterative eigenvalue procedure are numerically stable.

This behavior is illustrated in fig. 5.1, which shows the triton binding energy as a function of the MT interaction parameters obtained from a coarse parameter scan.

To further investigate the region of parameter space compatible with the experimental triton binding energy, refined scans are performed around parameter values yielding three-body binding energies close to the physical value. The results of the scans are shown in fig. 5.2, where are represented the MT potential parameters (v_{01}, v_{02}) in the vicinity of the physical triton binding energy. The binding energy varies smoothly across the explored region indicating numerical stability of the Faddeev equations.

5.3 Triton binding energy with chiral NN interactions

After validating the numerical implementation and the Bayesian framework using the phenomenological MT interaction, the analysis is extended to chiral two-nucleon interactions.

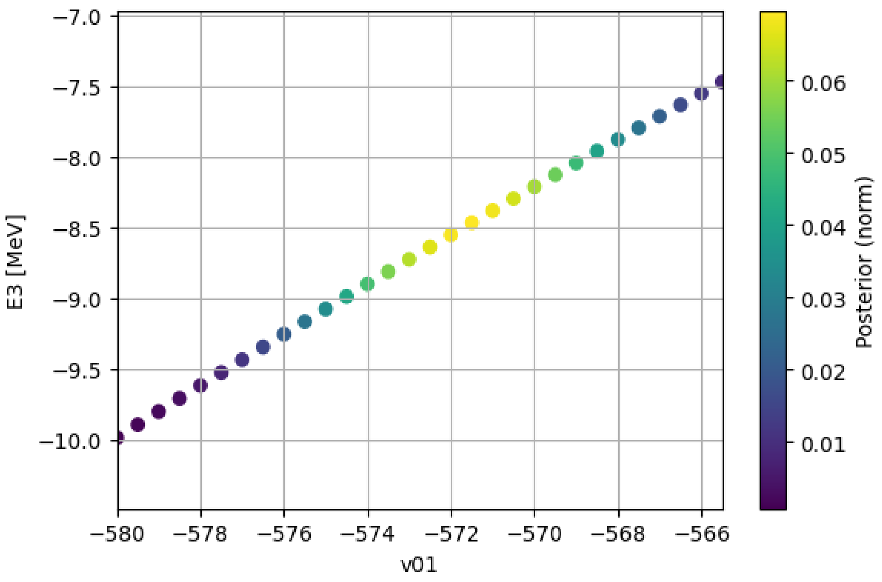

Figure 5.1: Triton binding energy E_3 as a function of the Malfliet-Tjon potential parameter v_{01} obtained from a coarse parameter scan. The smooth and monotonic dependence indicates numerical stability of the Faddeev solver. The color scale represents the normalized posterior probability associated with each parameter value. The posterior values appear numerically small because the distributions is normalized over the full discrete parameter grid.

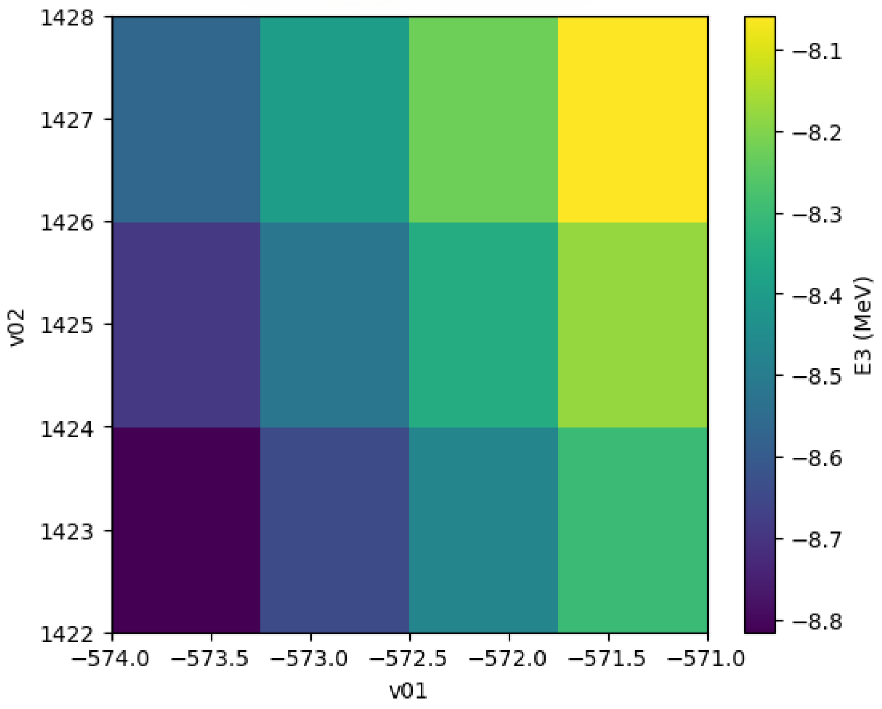

Figure 5.2: Refined scan of the triton binding energy E_3 as a function of the Malfliet-Tjon potential parameters (v_{01}, v_{02}). The color scale represents the binding energy in MeV. The smooth variation across the parameter grid highlights a narrow region of parameter space compatible with the experimental triton binding energy.

Table 5.2: Summary of the triton binding energy obtained with chiral two-nucleon interactions at different orders of the chiral expansion. The reported values correspond to the mean and standard deviation of the posterior distribution obtained from the Bayesian analysis.

Chiral order	$\langle E_3 \rangle$ [MeV]	σ_{E_3} [MeV]
LO	-10.45	0.16
NLO	-8.44	0.21
N^{2}LO	-8.40	0.16

χEFT provides a systematic and model independent description of nuclear forces, organized as an expansion in powers of a low momentum scale over a breakdown scale.

In this section, the triton binding energy is computed using chiral two-nucleon potentials at LO and NLO. For each order, the Faddeev equations are solved using fixed numerical parameters and the resulting binding energy is extracted from the eigenvalue condition.

Table 5.2 summarizes the triton binding energy obtained with chiral two-nucleon interactions at successive orders of the chiral expansion. The reported values correspond to the mean and standard deviation of the posterior distributions resulting from the Bayesian analysis.

A clear systematic trend is observed. At LO, the triton is significantly over bound, reflecting the limited accuracy of the interaction at this order. The inclusion of NLO corrections leads to a substantial reduction in the binding energy, which brings it closer to the experimental value. The further shift at N^{2}LO is comparatively smaller, indicating an improved convergence pattern of the chiral expansion.

5.3.1 Cutoff dependence of the triton binding energy

In χEFT, nuclear interactions are regularized by introducing a momentum space cutoff that suppresses high momentum components beyond the breakdown scale of the theory. While physical observables should be independent of the regulator in the limit of a complete calculation, residual cutoff dependence is expected at finite order and provides a measure of missing higher order contributions. The study of the cutoff dependence therefore provides a valuable diagnostic tool to assess the convergence pattern and theoretical uncertainties of the expansion.

In this project, the cutoff is treated as a nuisance parameter and its impact on the triton binding energy is analyzed within a Bayesian framework. For each chiral order, the binding energy is computed over a discrete set of cutoff values, and a posterior probability distribution over the cutoff is constructed by comparing the calculated energies to the experimental reference value.

The resulting posterior distributions over the cutoff parameter are shown in fig. 5.3. At LO the posterior exhibits a pronounced dependence on the cutoff, with a strong preference for specific regulator values. This behavior indicates that LO interaction alone does not provide a regulator independent description of the three-body bound state.

At NLO the posterior distribution becomes significantly broader, signaling a reduced sensitivity of the binding energy to the cutoff. This trend continues at N^{2}LO, where the posterior approaches an almost flat distribution over the explored cutoff range. The progressive flattening of the posterior reflects the increasing regulator independence of the interaction as higher orders in the chiral expansion are included.

To propagate the residual cutoff uncertainty into the final prediction for the triton binding energy, Bayesian model averaging is used. For each chiral order the binding energy is marginalized over the cutoff using the corresponding posterior distribution, yielding a mean value and an associated uncertainty that consistently incorporate regulator effects.

The results of the Bayesian model averaging are shown in fig. 5.4. At LO the averaged

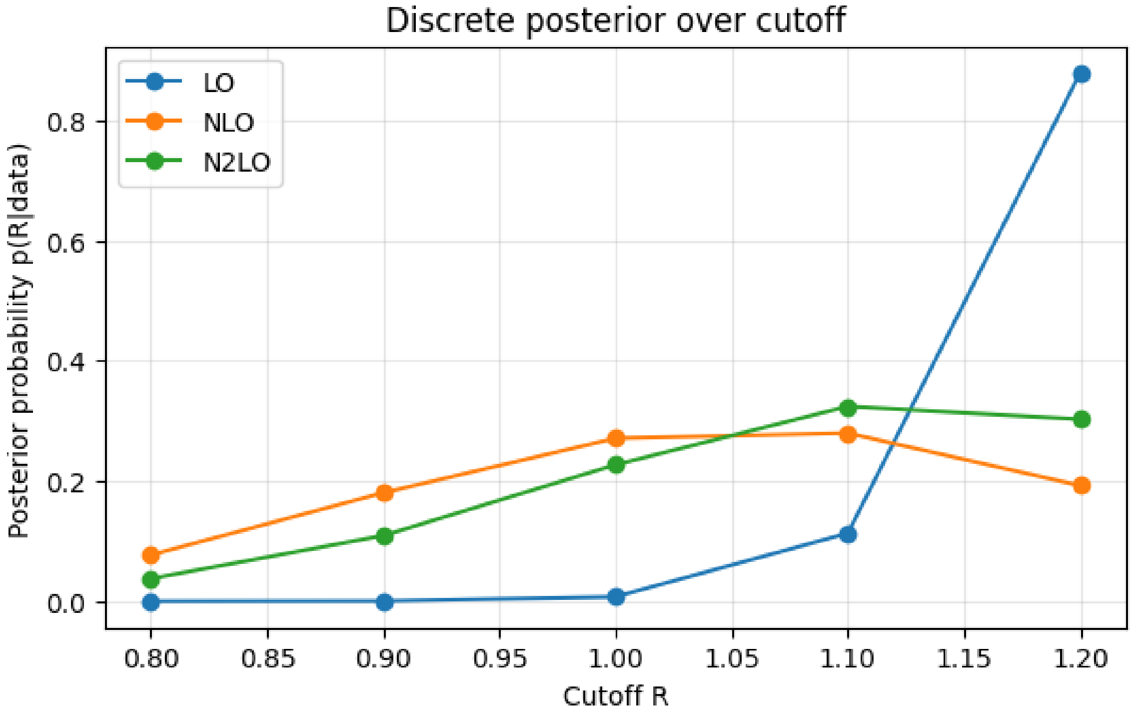

Figure 5.3: Posterior probability distributions of the regulator cutoff R obtained at leading (LO), next-to-leading (NLO), and next-to-next-to-leading order (N^2LO). The strong cutoff preference at LO is progressively reduced at higher orders, indicating an improved regulator independence of the chiral interaction.

binding energy is strongly affected by the cutoff uncertainty, resulting in a large deviation from the experimental value. At NLO both the central value and the associated uncertainty move closer to the experimental binding energy, reflecting the improved description of the three-body system. At N^2LO the binding energy exhibits only a mild residual uncertainty associated with the cutoff and the posterior averaged result is consistent with a converging chiral expansion. The reduction of both the cutoff sensitivity and the theoretical uncertainty provides quantitative evidence for the systematic improvement of the interaction with increasing chiral order.

Taken together, the cutoff posterior distributions and the Bayesian model averaged results provide a coherent picture of the convergence properties of the chiral expansion in the three-body sector. The strong regulator sensitivity observed at LO is progressively reduced at higher order, while the associated uncertainties decrease accordingly.

Residual cutoff dependence at NLO and N^2LO can be naturally interpreted as an estimate of missing higher order effects, most notably the contribution of three-nucleon forces, which first appear at N^2LO in the chiral expansion but are not included explicitly in the present calculations. The Bayesian framework adopted here offers a systematic and transparent way to quantify these uncertainties.

5.3.2 Sensitivity analysis of LO contact low-energy constants

After establishing that the regulator dependence is under control and selecting a reference cutoff value ($R = 1.0$ fm), the focus moves to the role of the low-energy constants (LECs) entering the leading-order (LO) contact interaction.

In χEFT LO contact LECs encode unresolved short range physics and are expected to play a central role in few-body observables. However, not all contact couplings contribute equally to a given observable. Since the present analysis is based on a single three-body measurement (the

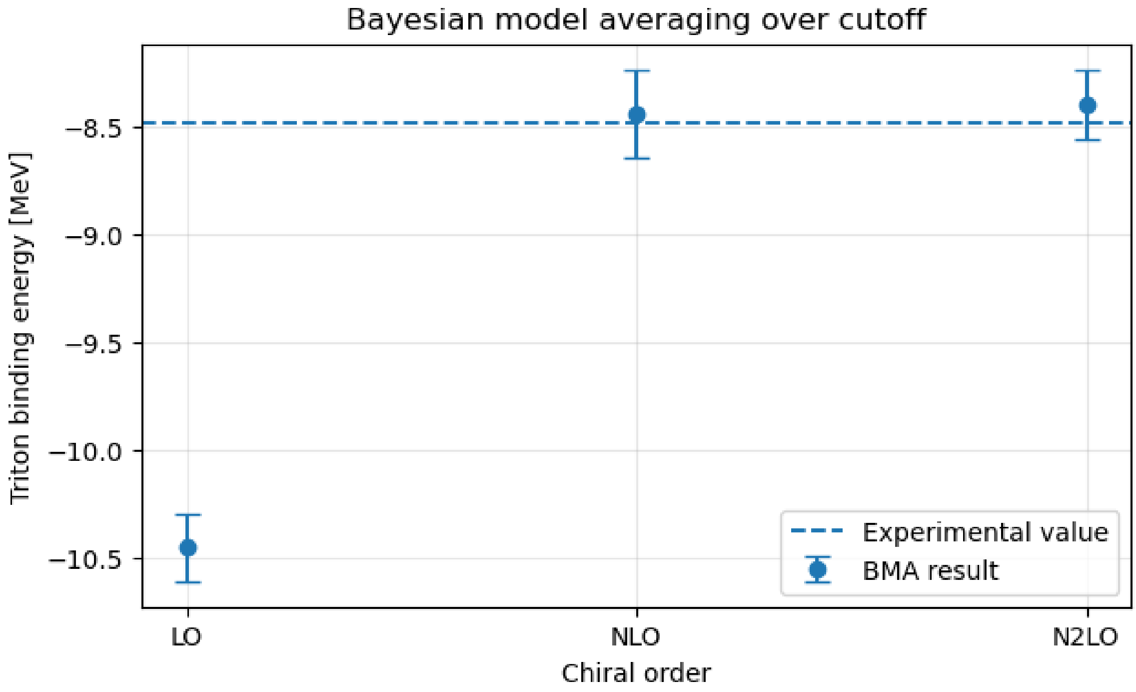

Figure 5.4: Bayesian model averaging of the triton binding energy over the regulator cutoff at LO, NLO, and N^{2}LO. Markers indicate posterior means, while error bars represent the corresponding standard deviations. The dashed line denotes the experimental binding energy.

triton binding energy), it is neither possible nor meaningful to vary all LO LECs simultaneously in a Bayesian calibration.

Instead, the idea is to perform a finite difference sensitivity analysis to identify which LO contact LECs have a significant impact on the triton binding energy at fixed order and cutoff. Each LO contact coupling is perturbed individually by a small relative amount (1%), while all others are kept at their nominal values. The resulting change in the triton binding energy provides a quantitative measure of the sensitivity of the observable to that specific LEC.

The binding energy is treated as a function of the EFT parameters $E = E(C_1, C_2, \dots)$ and its parametric dependence is probed by rescaling one LEC at a time as:

$$C_i \to (1+\delta)C_i, \qquad \delta = 0.01. \tag{5.1}$$

Assuming a local linear response, the sensitivity is estimated through a finite difference approximation:

$$\frac{\partial E}{\partial \ln C_i} \sim \frac{E_i - E_0}{\delta}, \tag{5.2}$$

where E_0 (for LO $E_0 = -11.29600$ MeV) is the reference energy and E_i is the energy obtained after the variation of C_i.

To compare the relative impact of different contact terms, is also defined a dimensionless sensitivity measure:

$$S_i^{\text{rel}} = \frac{|E_i - E_0|}{|E_0|}. \tag{5.3}$$

Table 5.3 reports a local sensitivity analysis of the triton binding energy with respect to the leading-order contact low-es. Each parameter is varied independently by 1% around its baseline value, while all other parameters are kept fixed.

The results show that the triton binding energy is dominated by a small subset of the LO contact interactions. In particular, the two most relevant LECs account for more than 85%

Table 5.3: Local sensitivity analysis of the triton binding energy with respect to the leading-order contact low-energy constants (LECs). Each LEC is varied independently by 1% around its baseline value at fixed cutoff $R = 1.0$, while all other parameters are kept fixed. The resulting change in the triton binding energy E_3 is used to define the logarithmic sensitivity $S_i = \partial E_0/\partial \ln C_i$. The normalized importance and cumulative importance quantify the relative contribution of each LEC to the total sensitivity.

LEC index	E_i [MeV]	$E_i - E_0$ [MeV]	$\partial E_0/\partial \ln C_i$ [MeV]	$\lvert S_i \rvert$	Importance	Cumulative
2	−11.579	−0.283	−28.3	28.3	0.597	0.597
3	−11.422	−0.126	−12.6	12.6	0.266	0.864
1	−11.361	−0.065	−6.48	6.48	0.136	1.000
4	−11.296	0.000	0.00	0.00	0.000	1.000

of the total sensitivity, while the remaining parameters have a negligible impact within the explored variation range.

The hierarchy observed in fig.5.5 confirms that the triton binding energy is primarily controlled by a limited number of short range interaction parameters, while other contact terms have a negligible impact within the explored variation range.

The sensitivity analysis reveals a clear hierarchy among the LO contact LECs. 2 couplings dominate the response of the triton binding energy, while 1 coupling has a subleading effect and another is effectively irrelevant within numerical accuracy.

5.3.3 Sensitivity analysis of NLO contact low-energy constants

The sensitivity analysis is now extended to the next-to-leading-order contact LECs, following the same local variation strategy adopted at LO. Each NLO contact LEC is varied independently by 1% around its baseline value at fixed cutoff $R = 1.0$, while all other parameters are kept fixed. The induced variation of the triton binding energy is used to define the logarithmic sensitivity measure $S_i = \partial E_0/\partial \ln C_i$.

The results of this analysis are summarized in table 5.4. Compared to the LO case, the sensitivity pattern at NLO is distributed over a large number of parameters. While a single contact term still provides the dominant contribution, several additional LECs exhibit non negligible influence on the triton binding energy.

In particular, the most important NLO contact interaction accounts for less than half of the total sensitivity, in contrast to the LO case where the response is strongly dominated by a single parameter. This redistribution of sensitivity reflects the increased operator structure of the NLO interaction and the presence of additional short range contributions.

The relative importance of the individual NLO contact terms is illustrated in fig. 5.6. The bar plot highlights a clear hierarchy among the LECs, with a small subset of parameters controlling the dominant response of the three-body binding energy, while the remaining terms contribute only marginally within the explored variation range.

A direct comparison with the LO sensitivity analysis reveals a qualitative change in the structure of the parameter dependence. While the LO interaction is characterized by a highly concentrated sensitivity dominated by a single contact term, the NLO interaction exhibits a broader sensitivity profile involving multiple LECs.

This behavior is consistent with the expected order by order improvement of χEFT. The inclusion of additional operators at NLO redistributes the short range physics across a larger parameter set, reducing the dominance of individual terms while preserving the overall sensitivity of the three-body system to contact interactions.

The NLO sensitivity analysis confirms that the triton binding energy probes specific combi-

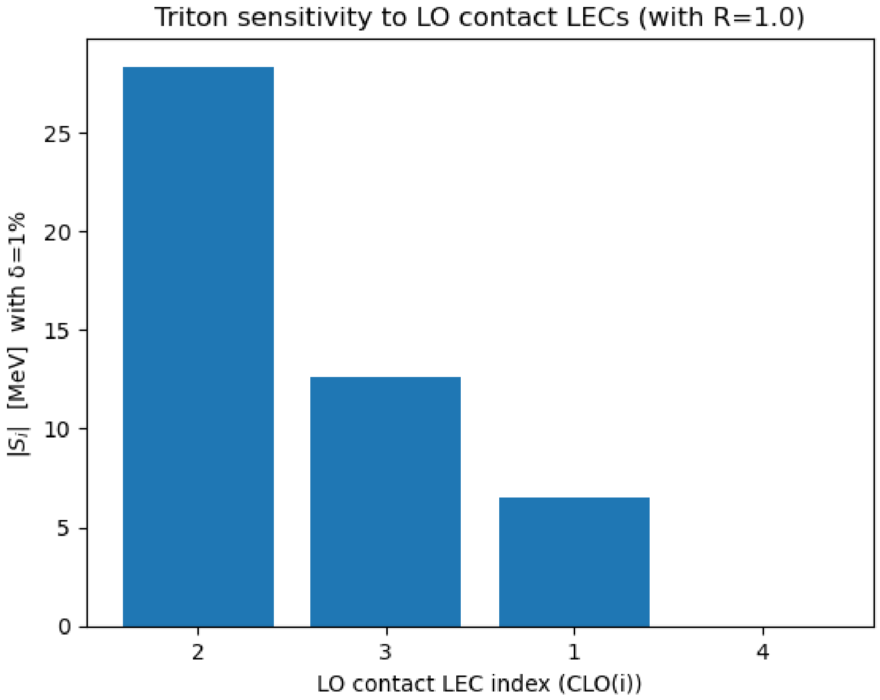

Figure 5.5: Normalized absolute sensitivity of the triton binding energy to variations of the LO contact LECs at fixed cutoff $R = 1.0$. Each LEC is varied independently by 1% around its baseline value. The dominance of a small subset of contact terms highlights the non-uniform sensitivity of the three-body bound state to short-range two-nucleon interactions.

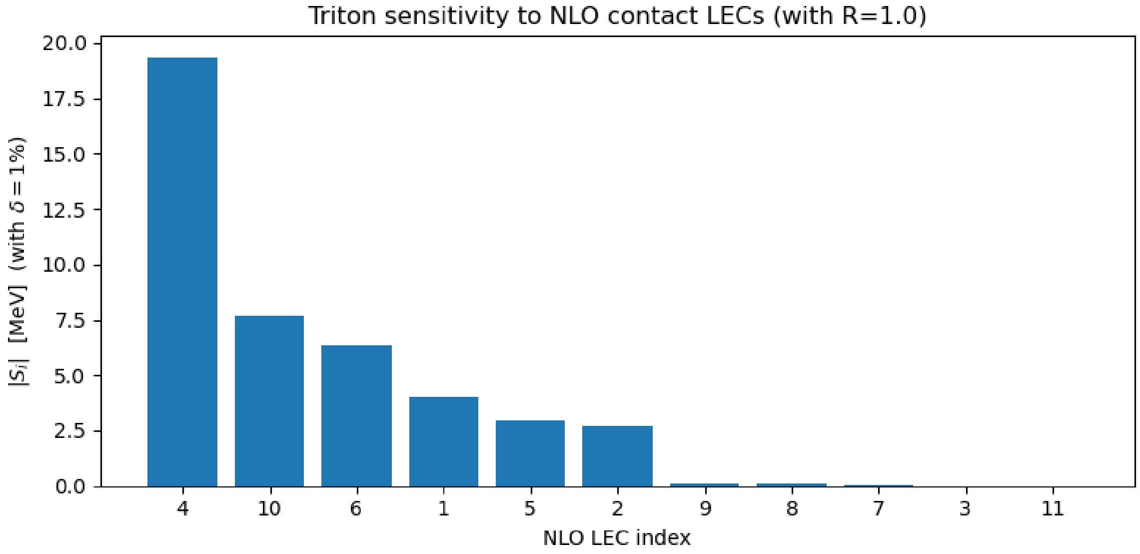

Figure 5.6: Normalized absolute sensitivity of the triton binding energy to variations of the NLO contact LECs at fixed cutoff $R = 1.0$. Each LEC is varied independently by 1% around its baseline value. Compared to LO, the sensitivity is distributed over a larger number of parameters, reflecting the increased operator structure of the NLO interaction.

Table 5.4: Local sensitivity analysis of the triton binding energy with respect to next-to-leading-order (NLO) low-energy constants (LECs). Each LEC is varied independently by 1% around its baseline value at fixed cutoff $R = 1.0$, while all other parameters are kept fixed. The resulting change in the triton binding energy E_3 defines the logarithmic sensitivity $S_i = \partial E_0 / \partial \ln C_i$. The normalized importance quantifies the relative contribution of each LEC to the total sensitivity.

LEC index	E_i [MeV]	$E_i - E_0$ [MeV]	$\partial E_0 / \partial \ln C_i$ [MeV]	$\lvert S_i \rvert$	Importance
4	-8.574	-0.192	-19.33	19.33	0.447
10	-8.458	-0.076	-7.66	7.66	0.177
6	-8.445	-0.063	-6.35	6.35	0.147
1	-8.422	-0.040	-4.02	4.02	0.093
5	-8.352	$+0.030$	$+2.99$	2.99	0.069
2	-8.355	$+0.027$	$+2.67$	2.67	0.062
9	-8.383	-0.001	-0.091	0.091	0.002
8	-8.381	$+0.001$	$+0.090$	0.090	0.002
7	-8.381	$+0.000$	$+0.029$	0.029	0.001
3	-8.382	$+0.000$	$+0.008$	0.008	0.000
11	-8.382	$+0.000$	0.000	0.000	0.000

nations of short range two-nucleon interactions rather than providing uniform constraints on all contact terms. As a consequence, the three-body bound state alone is insufficient to uniquely determine the full set of NLO LECs.

Residual parameter degeneracies and limited sensitivity to certain NLO contacts are naturally interpreted as a manifestation of missing higher order contributions, most notably genuine three-nucleon forces, which are not included in the present calculations. The results therefore provide a clear motivation for extending the analysis to include three-body interactions and additional few-body observables.

5.3.4 Local response of the triton energy to dominant NLO contact LEC multipliers

The one at a time sensitivity analysis reported in sec. 5.3.3 quantifies the local importance of each NLO contact LEC by probing the response of the triton binding energy to small perturbations of individual parameters. Since the procedure implicitly relies on a local linearization of the map from LECs to energy, it is important to verify that the numerical response remains approximately linear in the neighborhood of the baseline interaction.

To this end, it has been performed a study on the dominant NLO contact LECs identified by the sensitivity ranking at cutoff $R = 1.0$. In practice, it has been introduced a **multiplier** m acting on a single contact LEC (keeping all other NLO contact LECs fixed at their baseline values) and recompute the triton binding energy for a small set of perturbations around $m = 1$:

$$m \in \{0.99,\, 0.995,\, 1.0,\, 1.005,\, 1.01\}. \tag{5.4}$$

This local scan probes both the first order trend and potential non linear effects over a ±1% neighborhood.

For each scanned LEC, the computed values $E_3(m)$ are compared to a low degree polynomial model use purely as a diagnostic tool:

$$E_3(m) \approx a\, m^2 + b\, m + c, \tag{5.5}$$

where the coefficient b captures the local slope around the baseline, while the quadratic coefficient a provides a simple indicator of curvature within the probed interval. The resulting curves for the two dominant NLO contact LECs are shown in fig. 5.7 and fig. 5.8.

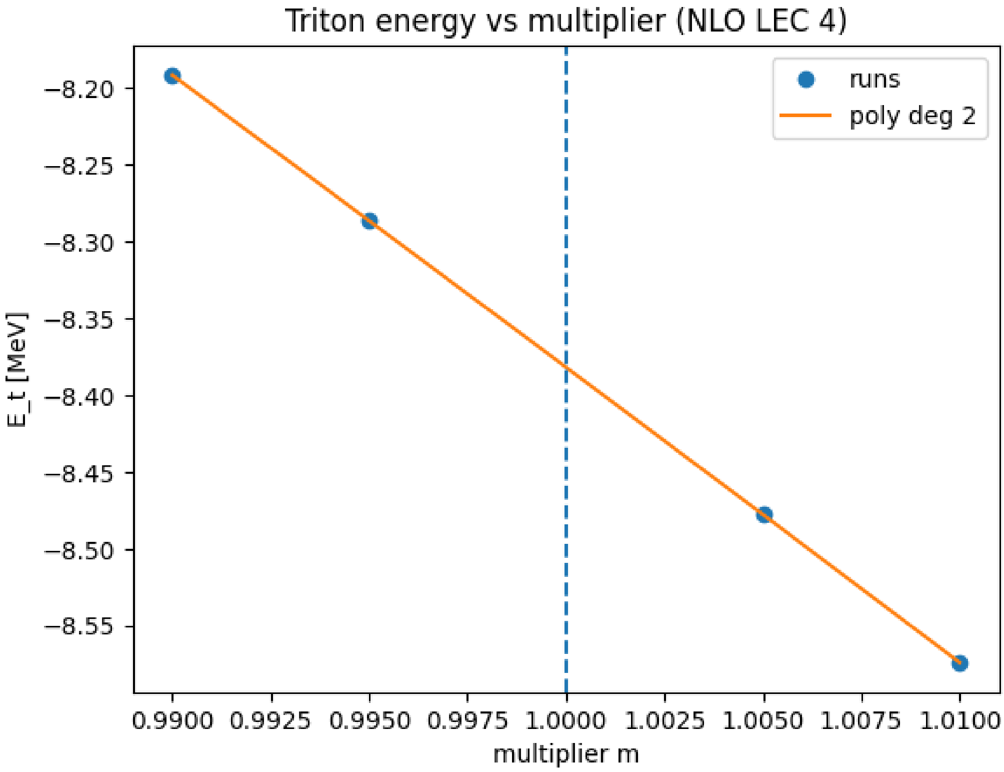

Figure 5.7: Local response of the triton binding energy E_3 to a small multiplier perturbation of the dominant NLO contact LEC (index 4) at cutoff $R = 1.0$. Markers denote TRITON runs, while the curve shows a quadratic fit used as a diagnostic of local nonlinearity around $m = 1$.

Although a quadratic regression model is used as a diagnostic tool, the resulting dependence of the triton binding energy on the LEC multiplier appears nearly linear over the explored interval. This is expected, since the scan is restricted to a narrow ±1% neighborhood around the baseline interaction, where higher-order terms in the Taylor expansion of $E_3(m)$ are strongly suppressed. The small fitted quadratic coefficient thus provides quantitative evidence that nonlinear effects are negligible in this regime, thereby validating the local linear approximation underlying the sensitivity analysis.

5.3.5 Impact of NLO contact variations on NN partial-wave interaction matrices

Cutoff 450 MeV

The sensitivity analysis in sections 5.3.3 quantify how the triton binding energy responds to local variations of individual NN contact couplings at fixed cutoff. Since the triton probes the NN interaction predominantly through low partial waves, it is useful to complement the few-body response with a two-body diagnostic: the goal is to understand how a local perturbation of a given NLO contact term modify the NN interaction in specific partial waves in the low momentum region relevant for few-body dynamics.

To address this, it has been performed a one at a time scan of selected NLO contact contributions in the chiral NN potential at NLO with cutoff $\Lambda = 450$ MeV. Each chosen contact contribution is rescaled as:

$$C \to (1+\delta)C, \qquad \delta = \pm 0.05, \tag{5.6}$$

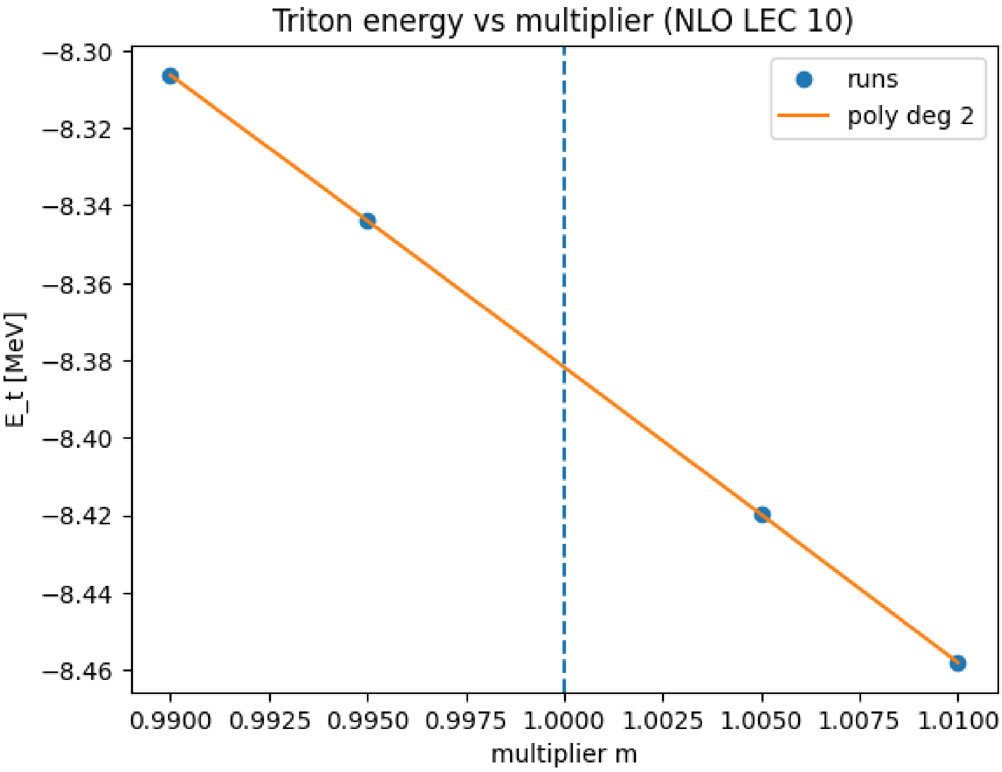

Figure 5.8: Same as Fig. 5.7, but for the second most influential NLO contact LEC identified by the sensitivity ranking (index 10), at cutoff $R = 1.0$.

while all other parameters are kept fixed. For each perturbation it has been recomputed the NN interaction in partial-wave representation and compared it to the baseline potential.

As a compact diagnostic in the few-body momentum range, the comparison has been restricted to $k, k' \leq k_{max}$ with $k_{max} = 200$ MeV and has been defined:

$$M_{\text{low}}(ch) = \max_{k,k' \leq k_{\text{max}}} |V_{ch}(k, k')| \,, \qquad \Delta M_{\text{low}}(ch) = M_{\text{low}}^{(\text{new})}(ch) - M_{\text{low}}^{(\text{base})}(ch), \tag{5.7}$$

together with the relative indicator:

$$\frac{\Delta M_{\text{low}}(ch)}{M_{\text{low}}^{(\text{base})}(ch)}. \tag{5.8}$$

The scan shows a strongly channel localized response: varying a contact term associated with a given partial wave predominantly modifies the corresponding NN channel, while induced changes in other channels are negligible within numerical accuracy. In the present implementation, the dominant relative changes in the low momentum block are observed in the **P-waves**, with typical magnitudes of a few percent for a ±5% rescaling. In contrast, changes in the deuteron sector (the coupled $^3S_1 -^3 D_1$ channel) are substantially smaller at the same perturbation level, indicating that these particular NLO variations deform the interaction mainly in the P-wave sector rather than in the deuteron channel.

This two-body diagnostic provides an important interpretation tool: when few-body observables (triton, deuteron) are used to constrain or retune short range parameters, the resulting improvement can be traced back to which NN partial waves are being effectively reshaped in the momentum region relevant for three-body binding.

Taken together the results of this NN partial-wave diagnostic provide a clear interpretation of the few-body sensitivity patterns observed in the previous sections.

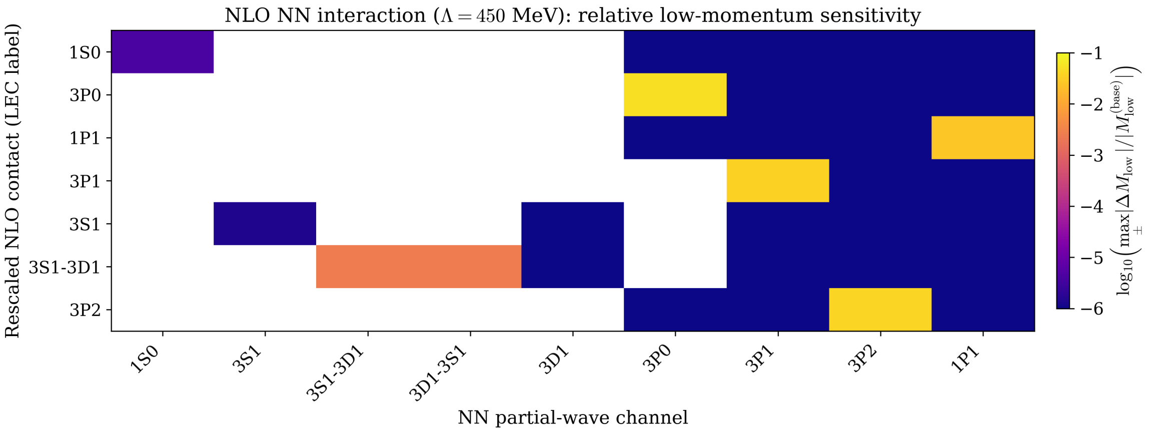

Figure 5.9: Logarithmic map of the relative low momentum sensitivity $\max_{\pm} |\Delta M_{\rm low}|/|M_{\rm low}^{\rm (base)}|$ for the NLO chiral NN interaction at cutoff $\Lambda = 450$ MeV. Each row corresponds to a locally rescaled NLO contact term, while each column denotes a NN partial-wave channel. The color scale highlights a strongly channel localized response, with dominant sensitivities in P-wave channels and suppressed variations in the S-wave sector relevant for few-body binding.

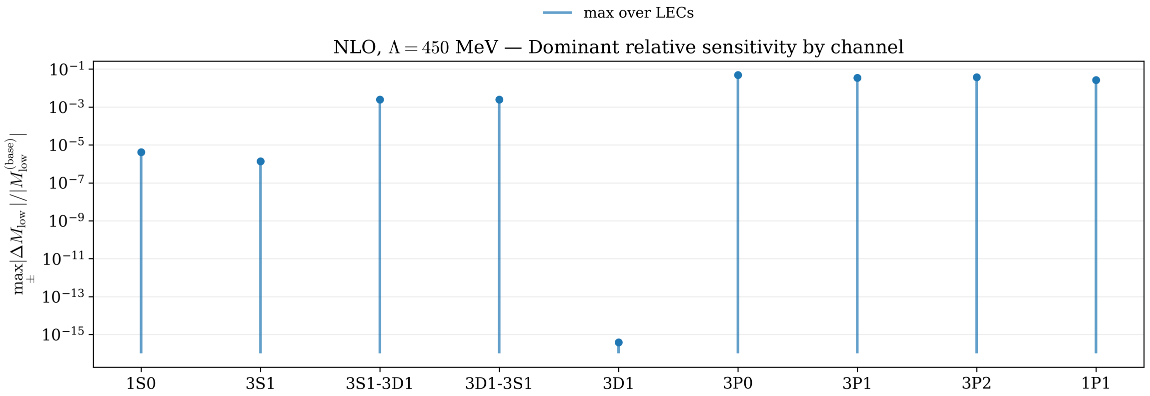

Figure 5.10: Maximum relative variation of the low momentum NN interaction strength induced by ±5% rescalings of individual NLO contact contributions at $\Lambda = 450$ MeV. The logarithmic scale emphasizes the hierarchy between partial waves, with P-wave channels exhibiting percent level sensitivity, while S-wave channels remain essentially uneffected.

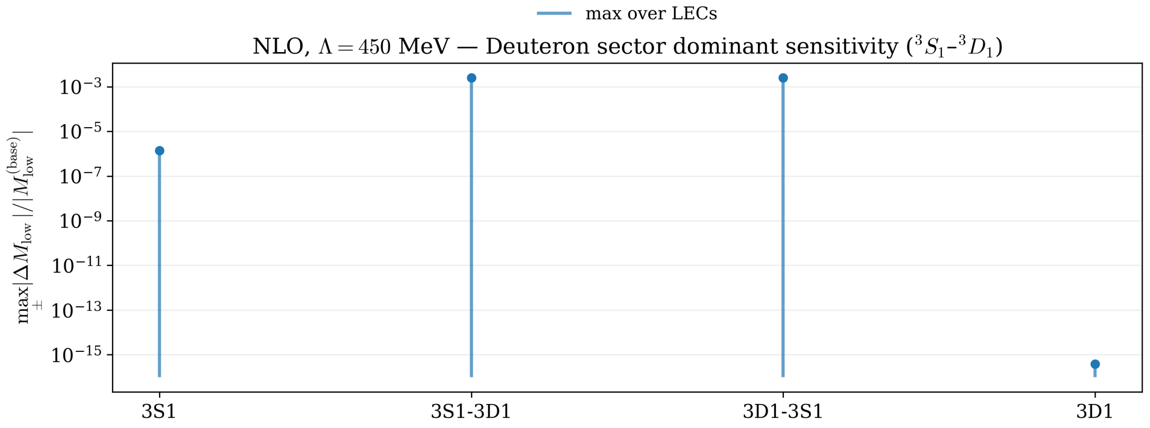

Figure 5.11: Relative low momentum sensitivity of the NN interaction in the deuteron sector (${}^3S_1$–${}^3D_1$ coupled channels) under ±5% variations of NLO contact terms at $\Lambda = 450$ MeV. Even the most effective short range operator produces only a sub percent relative change, illustrating the rigidity of the deuteron channel with respect to NN only NLO retuning.

Table 5.5: Maximum relative variation of the low–momentum NN potential M_{low} induced by a ±5% variation of each NLO contact LEC at cutoff $\Lambda = 450\,\mathrm{MeV}$. For each LEC, only the most sensitive NN partial wave is reported.

LEC	Channel	max $\lvert \Delta M_{\mathrm{low}}/M_{\mathrm{low}}^{(\mathrm{base})} \rvert$
$1S0$	${}^1S_0$	4.2×10^{-6}
$3P0$	${}^3P_0$	4.9×10^{-2}
$1P1$	${}^1P_1$	2.7×10^{-2}
$3P1$	${}^3P_1$	3.5×10^{-2}
$3S1$	${}^3S_1$	1.4×10^{-6}
$3S1$–$3D1$	${}^3S_1$–${}^3D_1$	2.5×10^{-3}
$3P2$	${}^3P_2$	3.7×10^{-2}

While the triton and deuteron binding energy primarily probe the S-wave sector of the NN interaction, local variations of NLO contact terms predominantly deform P-wave channels in the low momentum region relevant for few-body dynamics.

The coupled ${}^3S_1$–${}^3D_1$ channel, which governs deuteron binding and contributes significantly to the triton wavefunction, exhibits a reduced sensitivity, even under percent level variations of the corresponding short range operators. As a consequence, attempts to improve few-body observables by retuning NN interactions at NLO inevitably lead to sizable distortions of NN P-wave physics before producing any appreciable effect in the S-wave sector.

To complement the qualitative information provided by the sensitivity maps, table 5.5 reports a compact quantitative summary of the impact of NLO contact interactions on the low momentum NN potential. For each LEV, it has been identified the partial that exhibits the largest relative variation of M_{low} under a ±5% perturbation. This representation highlights the hierarchical structure of the NLO contact sector with P-wave LECs inducing $\mathcal{O}(10^{-2})$ effects, while S-wave channels and non diagonal couplings display a reduced sensitivity.

This analysis quantitatively explains the limited effectiveness of NN only retuning strategies for few-body systems and provides a robust motivations for the inclusion of genuine three-nucleon forces in chiral effective field theory.

Cutoff 500 MeV

The same partial-wave sensitivity analysis performed for $\Lambda = 450$ MeV has been repeated for the NLO chiral interaction with cutoff $\Lambda = 500$ MeV. The computational setup and definition of the sensitivity indicators are unchanged, allowing for a direct comparison across regulator choices.

The overall qualitative pattern remains stable: the dominant contribution to the low momentum matrix variation are concentrated in the P-wave channels (${}^3P_0, {}^3P_1, {}^3P_2, {}^1P_1$), while S-wave channels exhibit significantly smaller relative variations. The coupled ${}^3S_1 - {}^3D_1$ channel remains moderately sensitive, but does not dominate the response.

Compared to $\Lambda = 450$ MeV, the magnitude of the relative variations shows moderate quantitative changes, reflecting the expected regulator dependence of short range components. However, no qualitative reshuffling of the hierarchy of dominant channels is observed. This confirms that the sensitivity pattern identified at $\Lambda = 450$ MeV is not specific for a particular cutoff choice but rather a robust structural feature of the NLO contact sector.

The results for $\Lambda = 500$ MeV are reported in figs. 5.12, 5.13, 5.14 and in table 5.6.

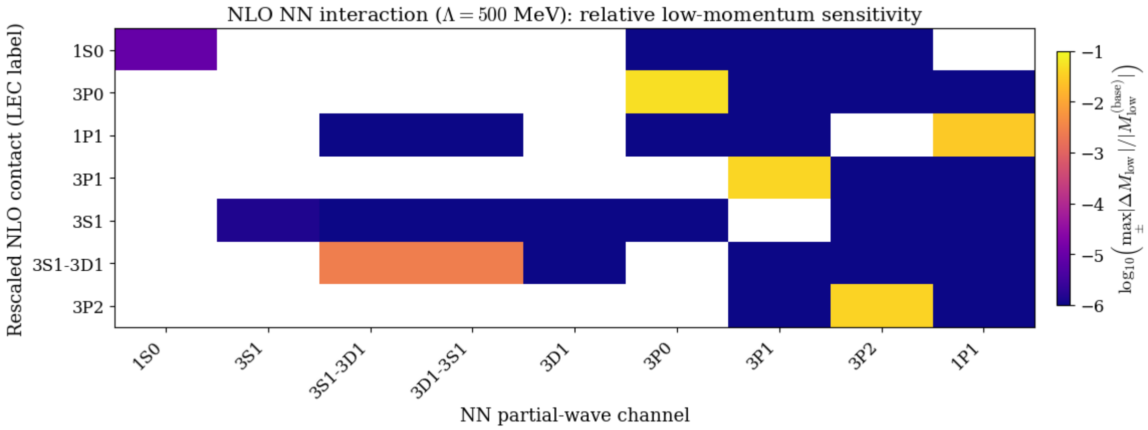

Figure 5.12: Logarithmic map of the relative low momentum sensitivity $\max_{\pm} |\Delta M_{\rm low}|/|M_{\rm low}^{(\rm base)}|$ for the NLO chiral NN interaction at cutoff $\Lambda = 500$ MeV. Each row corresponds to a locally rescaled NLO contact term, while each column denotes a NN partial-wave channel. The color scale highlights a strongly channel localized response, with dominant sensitivities in P-wave channels and suppressed variations in the S-wave sector relevant for few-body binding.

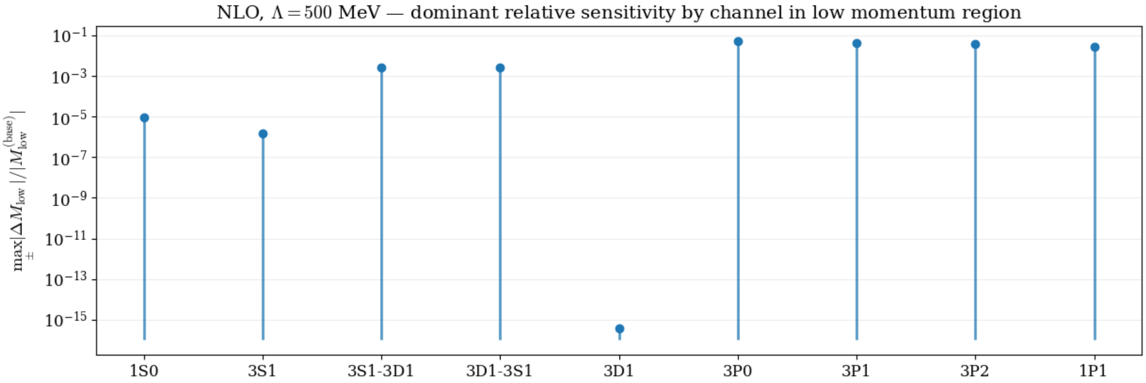

Figure 5.13: Maximum relative variation of the low momentum NN interaction strength induced by ±5% rescalings of individual NLO contact contributions at $\Lambda = 500$ MeV. The logarithmic scale emphasizes the hierarchy between partial waves, with P-wave channels exhibiting percent level sensitivity, while S-wave channels remain essentially unaffected.

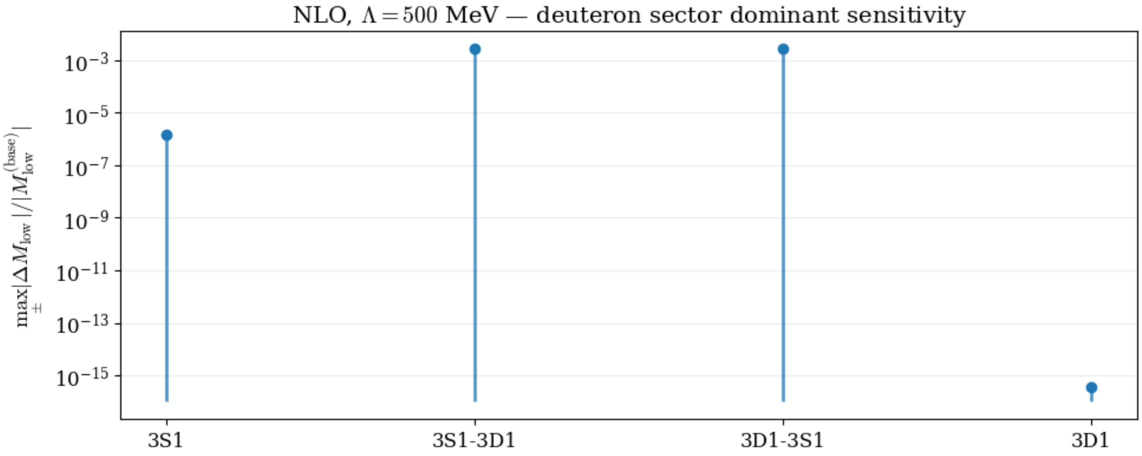

Figure 5.14: Relative low momentum sensitivity of the NN interaction in the deuteron sector ($^3S_1$–$^3D_1$ coupled channels) under ±5% variations of NLO contact terms at $\Lambda = 550$ MeV. Even the most effective short range operator produces only a sub percent relative change, illustrating the rigidity of the deuteron channel with respect to NN only NLO retuning.

Table 5.6: Maximum relative variation of the low–momentum NN potential M_{low} induced by a ±5% variation of each NLO contact LEC at cutoff $\Lambda = 500\,\text{MeV}$. For each LEC, only the most sensitive NN partial wave is reported.

LEC	Channel	max $\Delta M_{\text{low}}/M_{\text{low}}^{(\text{base})}$
$1S0$	$^1S_0$	8.9×10^{-6}
$3P0$	$^3P_0$	5.0×10^{-2}
$1P1$	$^1P_1$	2.8×10^{-2}
$3P1$	$^3P_1$	3.4×10^{-2}
$3S1$	$^3S_1$	1.4×10^{-6}
$3S1$–$3D1$	$^3S_1$–$^3D_1$	2.7×10^{-3}
$3P2$	$^3P_2$	3.6×10^{-2}

Table 5.7: Maximum relative variation of the low–momentum NN potential M_{low} induced by a ±5% variation of each NLO contact LEC at cutoff $\Lambda = 550\,\text{MeV}$. For each LEC, only the most sensitive NN partial wave is reported.

LEC	Channel	max $\Delta M_{\text{low}}/M_{\text{low}}^{(\text{base})}$
$1S0$	$^1S_0$	1.1×10^{-5}
$3P0$	$^3P_0$	5.2×10^{-2}
$1P1$	$^1P_1$	2.2×10^{-2}
$3P1$	$^3P_1$	4.2×10^{-2}
$3S1$	$^3S_1$	1.4×10^{-6}
$3S1$–$3D1$	$^3S_1$–$^3D_1$	2.7×10^{-3}
$3P2$	$^3P_2$	3.5×10^{-2}

Cutoff 550 MeV

The analysis has been also extended to $\Lambda = 550$ MeV. As in the previous cases, the dominant low momentum sensitivity is again driven primarily by the P-wave contact operators.

The results are shown in figs. 5.15, 5.16, 5.17 and in table 5.7.

Comparison across cutoff values

A direct comparison of the results obtained for $\Lambda = 450, 500, 550$ MeV reveals a consistent qualitative pattern across all regulator choices. In all cases, the dominant response of the low momentum NN interaction matrices to NLO contact variations is localized in the P-wave channels, while S-wave contributions remain more rigid.

The cutoff dependence manifests itself mainly at the quantitative level, affecting the absolute magnitude of the sensitivity indicators but not their relative hierarchy. This behavior is consistent with the interpretation of the regulator as a short distance resolution scale: increasing Λ modifies the short range structure of the potential, but does not alter the dominant operator content at low momentum.

The stability of the channel hierarchy across different cutoff values strengthens the interpretation of the observed sensitivity pattern as a structural feature of the NLO contact interaction rather than a regulator artifact. This observation is particularly relevant in the context of uncertainty quantification and Bayesian parameter analysis, where regulator independence of qualitative trends is a desirable property.

Table 5.8 summarizes the maximum relative low momentum sensitivity for each contact operator across the three cutoff choices. While absolute magnitude of the variation increases

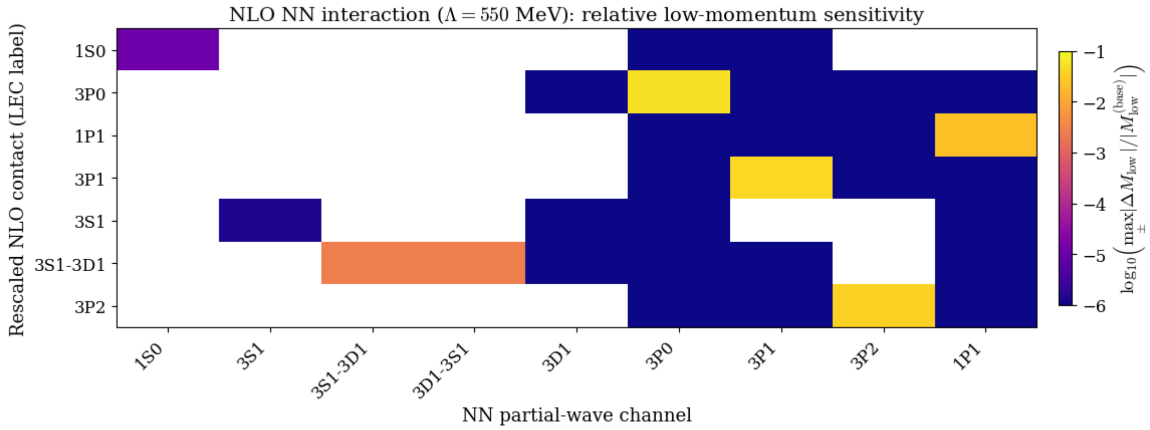

Figure 5.15: Logarithmic map of the relative low momentum sensitivity $\max_{\pm} |\Delta M_{\rm low}|/|M_{\rm low}^{\rm (base)}|$ for the NLO chiral NN interaction at cutoff $\Lambda = 550$ MeV. Each row corresponds to a locally rescaled NLO contact term, while each column denotes a NN partial-wave channel. The color scale highlights a strongly channel localized response, with dominant sensitivities in P-wave channels and suppressed variations in the S-wave sector relevant for few-body binding.

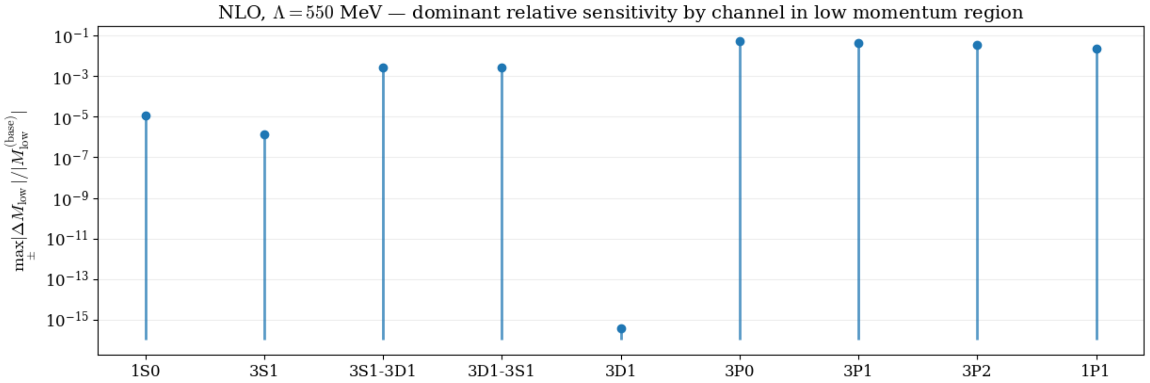

Figure 5.16: Maximum relative variation of the low momentum NN interaction strength induced by ±5% rescalings of individual NLO contact contributions at $\Lambda = 550$ MeV. The logarithmic scale emphasizes the hierarchy between partial waves, with P-wave channels exhibiting percent level sensitivity, while S-wave channels remain essentially unaffected.

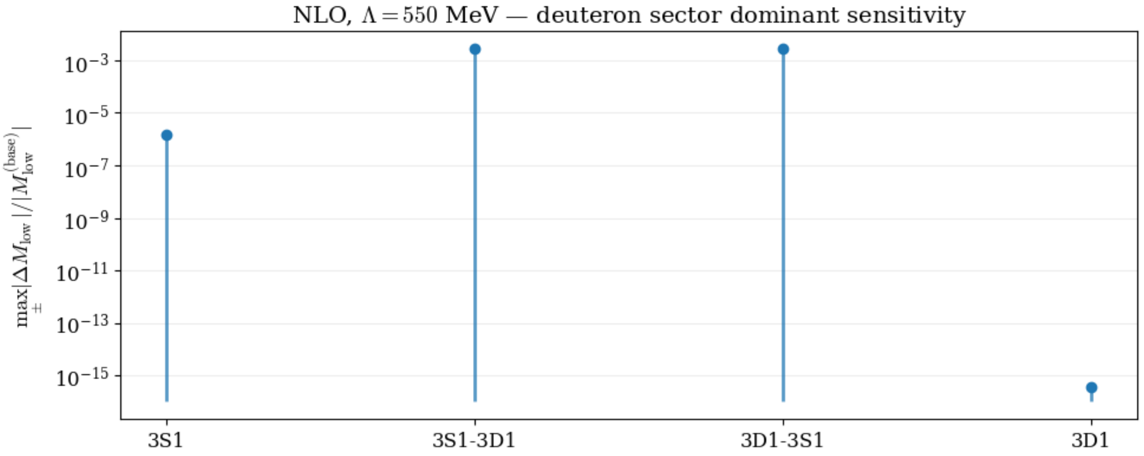

Figure 5.17: Relative low momentum sensitivity of the NN interaction in the deuteron sector ($^3S_1$–$^3D_1$ coupled channels) under ±5% variations of NLO contact terms at $\Lambda = 550$ MeV. Even the most effective short range operator produces only a sub percent relative change, illustrating the rigidity of the deuteron channel with respect to NN only NLO retuning.

Table 5.8: Maximum relative low–momentum sensitivity $\max_{\pm} |\Delta M_{\rm low}/M_{\rm low}^{\rm base}|$ for each NLO contact term and cutoff value.

LEC	$\Lambda = 450$ MeV	$\Lambda = 500$ MeV	$\Lambda = 550$ MeV
$^1S_0$	4.2×10^{-6}	8.9×10^{-6}	1.1×10^{-5}
$^3P_0$	4.9×10^{-2}	5.0×10^{-2}	5.2×10^{-2}
$^1P_1$	2.7×10^{-2}	2.8×10^{-2}	2.2×10^{-2}
$^3P_1$	3.5×10^{-2}	3.4×10^{-2}	4.2×10^{-2}
$^3S_1$	1.4×10^{-6}	1.4×10^{-6}	1.4×10^{-6}
$^3S_1$-$^3D_1$	2.5×10^{-3}	2.7×10^{-3}	2.7×10^{-3}
$^3P_2$	3.7×10^{-2}	3.6×10^{-2}	3.5×10^{-2}

moderately with Λ, the hierarchy of dominant channels remains unchanged. In particular, P-wave operators consistently produce the largest relative response.

5.3.6 Phase shift analysis under NLO contact variations

In order to complement the sensitivity study of the triton binding energy with a direct two-body observable, has been performed a systematic one at a time perturbative analysis to assess the dependence of the two-nucleon phase shifts to variations of the NLO LECs.

Considering the reference NLO450 interaction, individual LECs entering the tabulated contact matrix `tab(i,j)` were independently varied, while all remaining LECs were kept fixed at their baseline values.

The channels considered in this study were: $^1S_0 \quad (j = 17, i = 1)$, $^1S_0 \quad (j = 17, i = 1)$, $^3P_0 \quad (j = 21, i = 1)$, $^1P_1 \quad (j = 23, i = 1)$, $^3P_1 \quad (j = 25, i = 1)$, $^3S_1 \quad (j = 27, i = 1)$, $^3SD_1 \quad (j = 32, i = 1)$.

For each selected LEC, four perturbations were generated:

$$\pm 5\%, \quad \pm 10\%. \tag{5.9}$$

Each modified interaction was rebuilt independently, producing a dedicated `libforce.so` library. The resulting potentials were then used to compute the phase shifts in the neutron-proton channel up to $T_{\rm lab} = 350$ MeV. Since only one coefficient is varied at a time, the deviations observed in the phase shifts directly quantify the response of the scattering amplitude to that specific operator.

The PWA93 solution was used as an empirical benchmark for the on-shell NN interaction. The root mean square error (RMSE) between each perturbed interaction and the PWA93 reference was computed over the considered energy range in order to quantify the deviation in a compact form.

Figure 5.18 shows that the $^1P_1$ channel responds smoothly and systematically to local changes in its contact strength. The phase shift deformation becomes increasingly visible at intermediate and high energies. The deformation remains moderate for ±5% variations and becomes more visible for ±10%, particularly above $T_{\rm lab} \sim 100$ MeV. Although the phase shifts are shown up to $T_{\rm lab} = 350$ MeV for completeness, the quantitative discussion is restricted to energies below 200 MeV. At NLO, the chiral interaction is not expected to reproduce the empirical phase shifts accurately at higher energies; a consistent description in that region typically requires N^{3}LO or higher orders.

As shown in fig. 5.19 the $^3P_0$ channel exhibits a slightly stronger low energy sensitivity compared to $^1P_1$. The deviations remain moderate within ±5%, but become visibly larger for ±10% variations, particularly above 100 MeV.

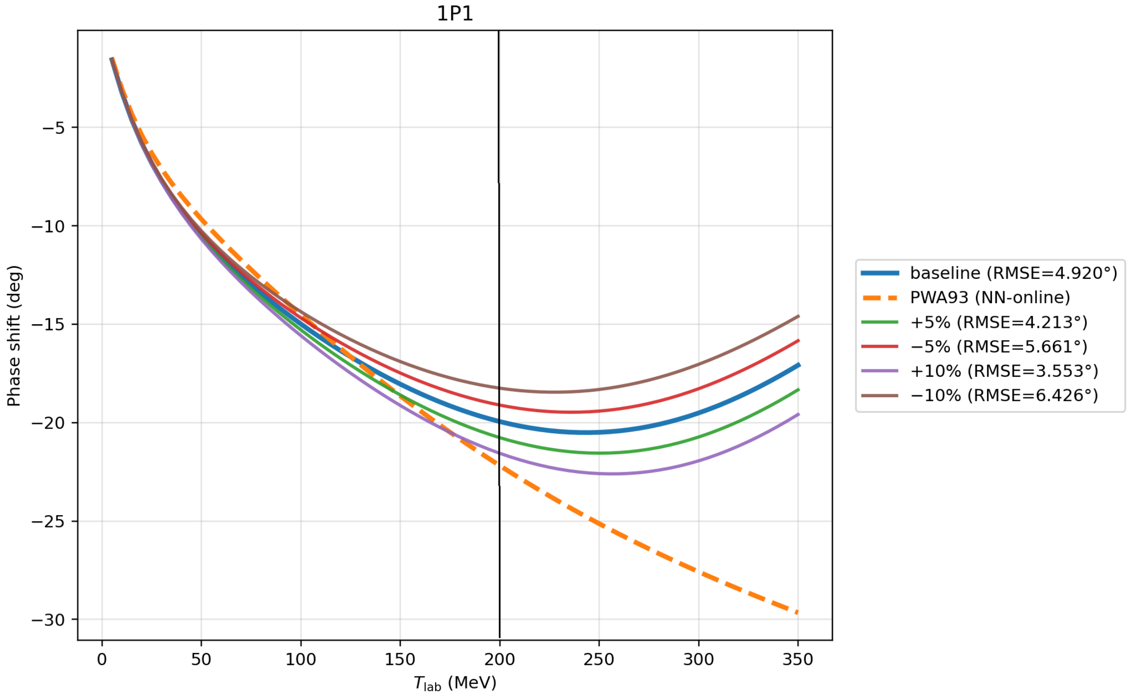

Figure 5.18: ${}^1P_1$ phase shifts as a function of laboratory energy. The solid blue curve represents the baseline chiral interaction. The dashed orange curve shows the PWA93 phase shift analysis. Colored solid curves correspond to ±5% and ±10% multiplicative variations of the associated NLO contact LEC. The vertical line at $T_{\text{lab}} = 200$ MeV marks the upper limit of the energy region where the NLO chiral interaction is expected to provide a controlled description. Results above this energy are displayed for completeness but are not considered qualitatively reliable at this order.

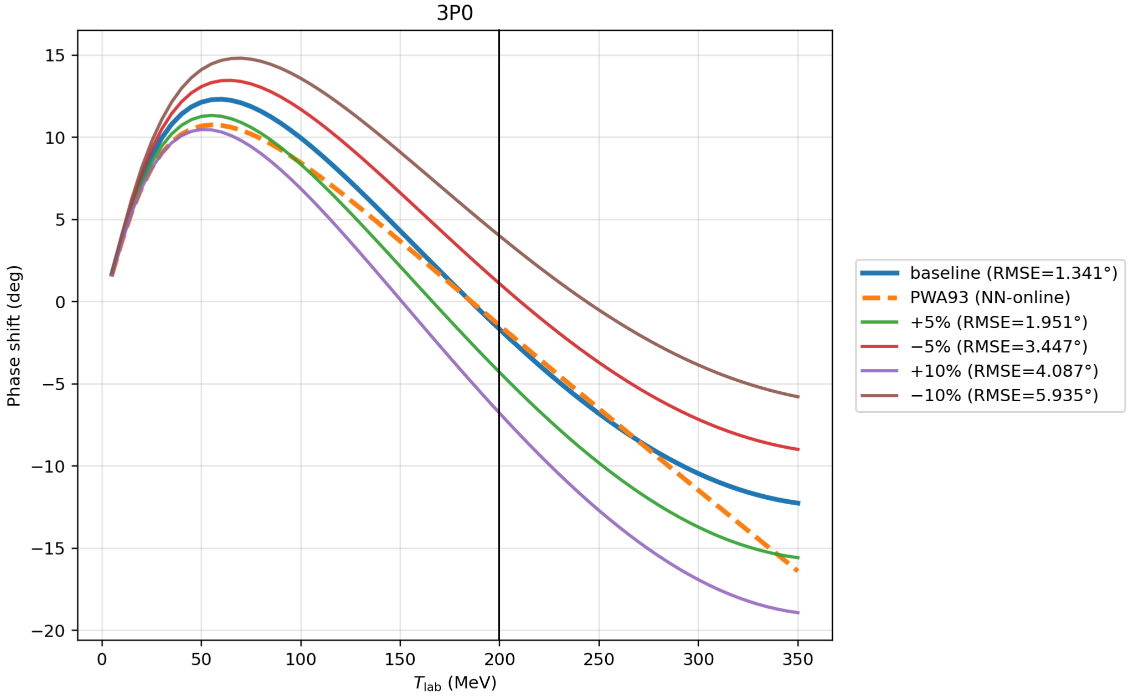

Figure 5.19: ${}^3P_0$ phase shifts for the baseline interaction and for ±5% and ±10% variations of the associated NLO contact LEC. The vertical line at $T_{\text{lab}} = 200$ MeV marks the upper limit of the energy region where the NLO chiral interaction is expected to provide a controlled description. Results above this energy are displayed for completeness but are not considered qualitatively reliable at this order.

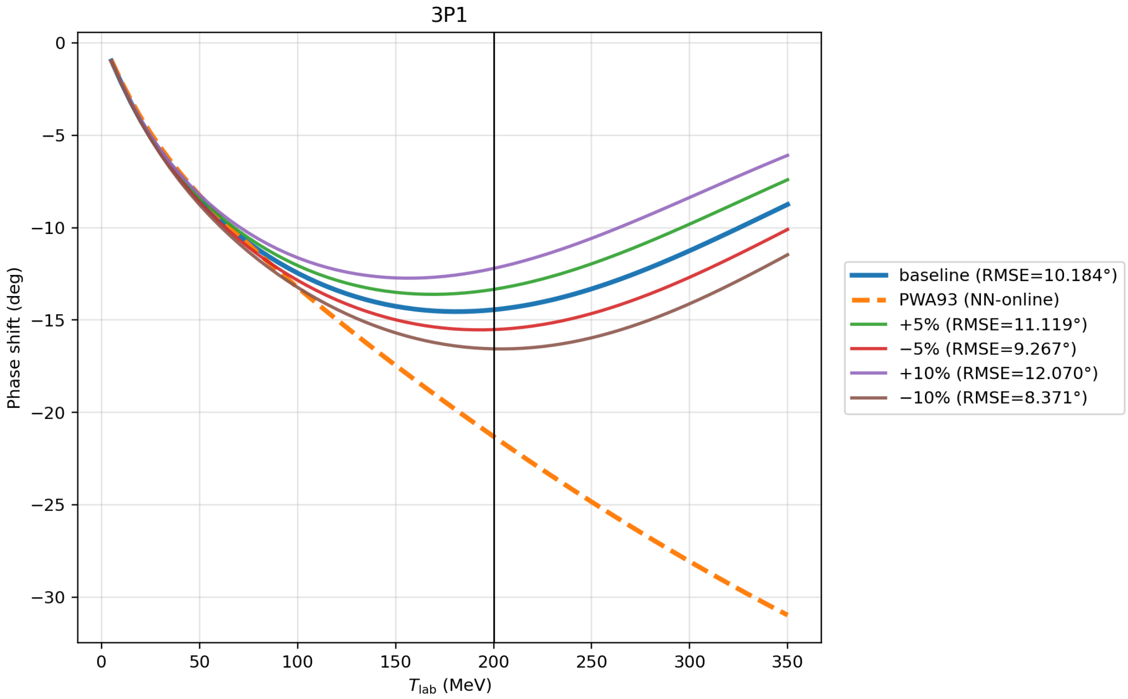

Figure 5.20: $^3P_1$ phase shifts for the baseline interaction and for ±5% and ±10% variations of the associated NLO contact LEC. The vertical line at $T_{\rm lab} = 200$ MeV marks the upper limit of the energy region where the NLO chiral interaction is expected to provide a controlled description. Results above this energy are displayed for completeness but are not considered qualitatively reliable at this order.

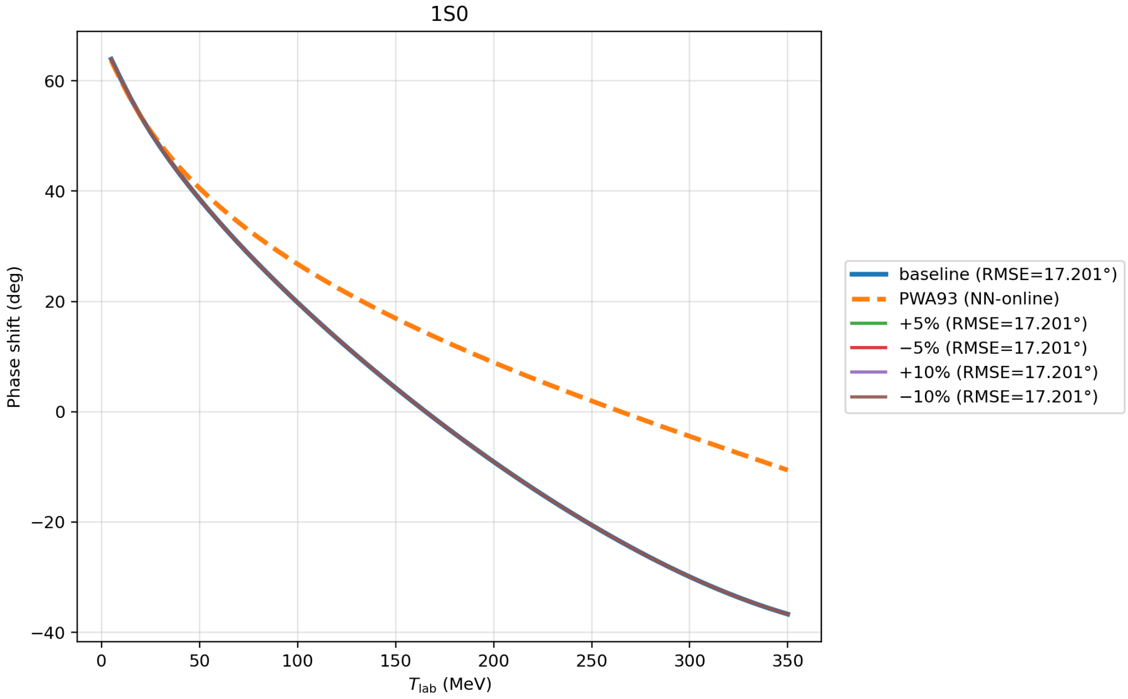

Figure 5.21: $^1S_0$ phase shifts for the baseline interaction and for ±5% and ±10% variations of the associated NLO contact LEC.

In fig.5.20 are reported the phase shifts for the ${}^3P_1$ channel.

The ${}^1S_0$ channel (reported in fig. 5.21) exhibits a markedly different behavior compared to P waves. In this case, no visible deviation of the phase shifts is observed under the perturbations of the contact LECs. The curves remain essentially indistinguishable from the baseline interaction over the entire energy range considered.

The reference phase shifts were obtained from the Nijmegen NN-OnLine database.

5.3.7 Physical interpretation in terms of operator component

The sensitivity analysis performed above can be interpreted in terms of the operator structure of the NN interaction introduced in the theoretical background chapter.

The dominant percent level variations are found in the P-wave channels (${}^3P_0$, ${}^3P_1$, ${}^3P_2$, ${}^1P_1$), which receive their leading contributions at NLO from derivative contact operators and from the spin-orbit component of the potential. This explains the comparatively strong response of these channels to controlled rescalings of individual NLO LECs.

In contrast, the uncoupled S-wave channels (${}^1S_0$ and ${}^3S_1$) remain essentially at the 10^{-6} level. This rigidity reflects the fact that their dominant dynamics is already fixed at LO through momentum independent contact terms and one pion exchange, so that moderate NLO short range variations produce only negligible corrections.

The coupled ${}^3S_1$–${}^3D_1$ channel, which is driven by the tensor operator S_{12}, exhibits an intermediate sensitivity at the 10^{-3} level. This behavior is consistent with the role of tensor correlations, which are important ut structurally constrained by the underlying long range pion dynamics.

Overall, the results indicate that NLO short range variations primarily affect angular momentum dependent components of the NN interaction, while leaving the dominant S-wave binding mechanism largely intact.

Chapter 6

Conclusions

The purpose of this thesis was to study the three-nucleon bound state problem within the momentum space Faddeev formalism, with particular focus on the triton binding energy as a diagnostic observable. The work combined a detailed analysis of the theoretical framework, a careful validation of numerical implementations and a quantitative investigation of the sensitivity of the three-body system to variations in the underlying two-nucleon interaction.

In the first part of the project, the structure of the Faddeev equations for identical nucleons was reviewed and reformulated in a form suitable for numerical solution. The bound state problem was interpreted as an homogeneous integral equations whose solutions correspond to eigenvalues of the kernel $K(E) = G_0(E)tP$. Particular attention was dedicated to the role of the embedded two-body t-matrix, the permutation operator and the spectral condition determining the binding energy. Benchmark calculations were performed using the Malfliet-Tjon potential through the TRIMOD implementation. This step allows a systematic validation of the computational setup, including the construction of Jacobi momentum grids, spline interpolation procedures and channel space truncation. In the explored parameter region, the triton binding energy exhibited a smooth and stable dependence on the potential parameters, confirming the numerical reliability of the solver and providing a controlled reference case.

The analysis was then extended to chiral effective field theory NN interactions using the TRITON framework. The cutoff dependence of the triton binding energy was investigated across different chiral orders. At leading order, a pronounced sensitivity to the regulator was observed, reflecting the limited flexibility of the interaction at that level. As the chiral order increases, the cutoff dependence progressively reduces, indicating an improved internal consistency of the EFT expansion. A Bayesian framework was employed to quantify the statistical impact of regulator variations. By treating the cutoff as a nuisance parameter and constructing posterior distributions conditioned on the experimental triton binding energy, it was possible to propagate residual regulator dependence into a final averaged prediction. This approach provided a quantitative method to asses theoretical uncertainties associated with the choice of regulator.

An important part of the thesis was the sensitivity analysis of contact low energy constants at LO and NLO. The triton binding energy was found to respond non uniformly to variations in the LEC multiplier. At LO, the triton calculation involves four effective contact multipliers entering the S-wave channels. The observed sensitivity pattern is therefore not simply the consequence of a small parameter space, but reflects the fact that all LO contact operators act predominantly in the S-wave sector, which is also the dominant component of the three-body bound state. As a result, variations of these LECs directly affect the binding energy, but within a structurally constrained operator basis. At NLO, additional momentum dependent contact operators enlarge the interaction space and introduce deformations in higher partial waves, in particular in P-wave channels. The sensitivity of the triton energy becomes more distributed among several parameters. However, the overall impact of these additional degrees of freedom remains limited, since the triton ground state is still largely governed by S-wave dynamics.

To better understand this behavior, the impact of NLO contact variations on NN partial-wave interaction matrices and phase shifts was analyzed. The results show that the dominant LEC variations primarily deform low momentum P-wave channels, while S-wave channels remain more rigid. This observation explains why retuning NN contact terms alone has limited power in reproducing the experimental triton binding energy and highlights the structural role of genuine three-nucleon forces in achieving a quantitative accurate description.

Overall, this work demonstrates how the triton binding energy can serve as a sensitive probe of both numerical implementation choices and theoretical input in few-body nuclear physics. The combined three-body, partial-wave and Bayesian analyses provide a coherent picture of the interplay between two-body dynamics, regulator dependence and many-body observables.

Future extensions of this study could include the explicit inclusion of three-nucleon forces within the same Bayesian framework. Since the present analysis shows that variations of NN contact terms alone have limited power on the triton binding energy, a consistent extension at N^2LO including genuine three-body operators would allow one to disentangle regulator effects from genuine many-body dynamics and to quantify their relative impact. A second important extension concerns the simultaneous analysis of additional observables, such as nucleon-deuteron elastic scattering or breakup processes. Including continuum observables would provide complementary constraints and reduce parameter degeneracies that cannot be resolved using the binding energy alone. In this context, a correlated Bayesian treatment of multiple observables would offer a systematic strategy for uncertainty propagation and parameter inference. Finally, a more systematic treatment of chiral truncation uncertainties could be incorporated. While this thesis focused on regulator dependence and local LEC sensitivity, combining these effects with order by order EFT truncation estimates would provide a more complete assessment of theoretical uncertainties. Such an approach would strengthen the connection between few-body calculations and modern uncertainty quantification methodologies in nuclear physics.

Appendix A

Implementation details

A.1 Jacobi momentum grids and quadrature routines

The numerical solution of the Faddeev equations requires the discretization of the Jacobi momentum variables associated with the interacting pair and the spectator particle. In TRIMOD, both momentum variables are represented on non uniform grids constructed through Gauss-Legendre quadrature, with a suitable mapping to the physical momentum intervals. This strategy allows one to achieve high numerical accuracy while keeping the total number of grid points manageable.

The construction of the grids is performed using an auxiliary quadrature routine, `gauss`, which generates integration nodes and weights on a generic interval $[a, c]$ with an adjustable clustering around a user defined mid point b. Internally, the routine first computes standard Gauss-Legendre nodes on the interval $[-1, 1]$ and then maps them to the physical domain through a rational transformation. This procedure preserves the exactness of the quadrature for polynomials up to degree $2n - 1$ while allowing for an enhanced resolution in regions of physical relevance.

Two distinct momentum grids are generated:

- the spectator momentum grid $q \in [0, q_{\max}]$, which controls the motion of the third particle relative to the interacting pair;
- the pair relative momentum grid p, which resolves the internal dynamics of the two-body subsystems.

The spectator momentum grid is generated using a single quadrature interval, with an increased density of points at low momenta in order to resolve the long range behavior of the kernel. In the code, the grid is constructed through the call:

```
call gauss(0.d0, q0, qmax, nq, q, q2, wq)
```

which produces n_q quadrature points $q(i)$, the corresponding squared momenta $q^2(i)$ stored in `q2` and the Gaussian weights `wq`.The clustering parameter q_0 controls the resolution in the low momentum region.

The pair relative momentum grid is constructed by splitting the physical domain into two momentum intervals in order to separately resolve the low/intermediate and high momentum regions. The two sub grids are generated as:

```
call gauss(0.d0, p0, pmax, np1, aux1, aux2, aux3)
call gauss(pmax, pm, pcut, np2, aux4, aux5, aux6)
```

The first call generates a dense grid in the interval $[0, p_{\max}]$, while the second covers the high momentum tail up to the cutoff p_{cut}. The two grids are subsequently merged into a single array $p(1{:}n_p)$, with the first grid point fixed at $p = 0$ and assigned a vanishing integration weight. This choice simplifies the treatment of the kernel at the origin.

A.2 Spline interpolation and permutation operator

The numerical evaluation of the permutation operator P in the Faddeev kernel requires transforming the Faddeev component between different sets of Jacobi coordinates corresponding to different choices of interacting pair and spectator. While the relations between the old and new Jacobi momenta can be derived analytically, their numerical implementation requires evaluating the Faddeev component at momentum values that do not coincide with the original discretization grid.

In TRIMOD, this problem is addressed by representing the Faddeev component on the pair momentum grid through cubic spline interpolation. This approach allows for an accurate and efficient evaluation of the kernel without introducing additional quadrature grids or excessive computational overhead.

The spline representation is constructed in the module `interpolation`. The routine:

```
call spline(nptot, np, nq, nx, q, q2, wq, p, wp, x, wx, s1, s2)
```

receives as input the Jacobi momentum grids and the associated Gaussian weights, and returns the precomputed spline coefficients stored in the four dimensional arrays `s1` and `s2`. These arrays encode the cubic spline basis functions required to interpolate the Faddeev component when transforming between different Jacobi partitions.

In addition, an angular quadrature grid $x \in [-1, 1]$ with weights w_x is constructed to discretize the cosine of the angle between the Jacobi momenta. This angular integration enters explicitly in the action of the permutation operator.

Within the spline helper routines, the Faddeev component is locally approximated by a cubic polynomial in the pair momentum variable. Schematically, the interpolation can be written as:

```
    spl(j) = ((fak3(i,j)*dx + fak2(i,j))*dx + fak1(i,j))*dx
```

which explicitly shows that the spline is a third-order polynomial in the local coordinate dx. The precomputed coefficients stored in `s1` and `s2` allow one to efficiently evaluate this polynomial at arbitrary transformed momentum values.

The spline representation is used in the numerical evaluation of the permutation operator appearing in the kernel $K(E) = G_0(E)\,t(E)\,P$. For a fixed set of Jacobi momenta (p, q), the action of P involves an integral over the angle between the momenta and a transformation to a different Jacobi partition.

In TRIMOD, this is implemented through a combined angular quadrature and spline-based interpolation. The discrete action of the permutation operator takes the form of a double sum:

```
s = s + wx(ix)*s1(ix,ip1,iqp,iq)*s2(ix,ip2,iqp,iq)
```

where the summation over i_x corresponds to Gaussian integration over the cosine of the angle between the Jacobi momenta. The spline coefficients account for the evaluation of the Faddeev component at the transformed momenta arising from the permutation.

This procedure provides an accurate numerical realization of the permutation operator without explicitly storing or recomputing the Faddeev component on multiple Jacobi grids. It plays a crucial role in ensuring both numerical stability and computational efficiency of the iterative solution of the Faddeev equations.

A.3 Two-body t-matrix computation

The two-body transition operator entering the Faddeev kernel is computed in TRIMOD by solving the Lippmann-Schwinger equation in momentum space for each value of the spectator momentum.

For a fixed two-body energy e and a discretized pair momentum grid $\{p_i\}$, the Lippmann-Schwinger equation for the two-body t-matrix can be written as:

$$t(e) = V + VG_0(e)t(e), \tag{A.1}$$

where V denotes the two-body interaction in momentum space and $G_0(e)$ is the free two-body propagator. After discretization of the intermediate momentum variable, this equation reduces to a linear algebraic system of the form:

$$At = V, \tag{A.2}$$

where the matrix A represents the operator $1 - VG_0$ in the chosen momentum basis.

In TRIMOD, the matrix A is constructed explicitly in the subroutine `tmat` contained in the module `m_trimod_sub.f90`. The matrix elements incorporate the momentum space interaction and the discretized free propagator, including the appropriate Gaussian quadrature weights.

The resulting linear system is solved using standard LU decomposition with partial pivoting provided by the LAPACK routine `dgesv`:

```
call dgesv(nptot, nptot, akern, nptot, ipiv, vv, nptot, ifail)
```

The input array `vv`, initially containing the potential matrix V, is overwritten with the solution of the system and returned as the off shell two-body t-matrix. This approach ensures a robust and numerically stable solution of the Lippmann-Schwinger equation for all momentum grid points.

A.4 Iterative solver and energy search

This appendix documents the numerical strategy adopted in TRIMOD to solve the homogeneous Faddeev equation for the three-body bound state and to determine the corresponding binding energy. The procedure consists of an iterative application of the discretized Faddeev kernel combined with an outer energy search loop.

For a fixed trial value of the three-body energy E, the homogeneous Faddeev equation can be written schematically as:

$$\psi = K(E)\psi, \qquad K(E) = G_0(E)t(E)P, \tag{A.3}$$

where $G_0(E)$ is the free three-body propagator, $t(E)$ is the embedded two-body t-matrix, and P is the permutation operator. In TRIMOD, this equation is solved by power iteration.

For a fixed energy $E = e(\text{ie})$, the code first computes the off-shell t-matrix for all spectator momenta:

```
    do iq = 1, nq
        e2 = e(ie) - 0.75_dp * q2(iq)
        call tmat(e2, nptot, p, p2, wp, v, th)
        t(:,:,iq) = th(:,:)
    end do
```

The iterations then start from the constant trial vector

```
     psi0(ip,iq) = 1.0_dp  ! for all ip, iq
    x1 = psi0
```

and repeatedly applies the discretized kernel to obtain a new vector x2. The kernel action has the following structure:

```
    ! angular + spectator-momentum integration using splines
    do ip1 = 1, np
        shh = 0.0_dp
        do iqp = 1, nq
            sh = 0.0_dp
            do ip2 = 1, np
                s = 0.0_dp
                do ix = 1, nx
                    s = s + wx(ix)*s1(ix,ip1,iqp,iq)*s2(ix,ip2,iqp,iq)
                end do
                sh = sh + s * x1(ip2,iqp)
            end do
            shh = shh + sh * wq(iqp)
        end do
        h(ip1) = shh
    end do

    ! convolution with two-body t-matrix and free propagator
    do ip = 1, np
        shhh = 0.0_dp
        do ip1 = 1, np
            shhh = shhh + t(ip,ip1,iq) * h(ip1)
        end do
        x2(ip,iq) = shhh / ( e(ie) - 0.75_dp*q2(iq) - p2(ip) )
    end do
```

which is the discrete analog of applying $G_0(E)t(E)P$ to the Faddeev component. After each application, TRIMOD, computes the local ratio:

```
     rnew(ip,iq) = x2(ip,iq) / x1(ip,iq)
```

whenever $|x1(ip, iq)|$ is not too small. The convergence of the iterations is monitored at a fixed pivot point $(i_{\rm pf}, q_{\rm pf})$, chosen as `ipf=8`, `iqf=5`:

```
    df = ( rnew(ipf,iqf) - rold(ipf,iqf) ) / rold(ipf,iqf)
```

and the loop ends when $|df| < 10^{-7}$ or when the maximal number of iterations `itermax` is reached. The quantity:

```
    eta(ie) = rnew(ipf,iqf)
```

is then taken as the approximate eigenvalue $\eta(E)$ of the kernel at that energy.

The binding energy is located by searching for the zero of:

$$\mathrm{eig}(E) = \eta(E) - 1 \tag{A.4}$$

In the code this is stored as:

```
    eig(ie) = eta(ie) - 1.0_dp
```

and the function `search` in `m_trimod_sub.f90` updates the next trial energy `e(ie+1)` using a simple secant like scheme:

- if $\mathrm{eig}(E_{i-1})$ and $\mathrm{eig}(E_i)$ have opposite signs, the new estimate is:

  $$E_{i+1} = E_i - \mathrm{eig}(E_i)\frac{E_i - E_{i-1}}{\mathrm{eig}(E_i) - \mathrm{eig}(E_{i-1})}, \tag{A.5}$$

  which is exactly what the code implements as:

  ```
  e3 = e2 - f2*(e2-e1)/(f2-f1)
  ```

- if the signs are equal, the code performs a simple step in energy of size `de` (converted in internal units), ensuring that the algorithm continues moving towards the root.

The energy loop is bounded by `iemax`, and the search is stopped as soon as $|\mathrm{eig}(E)| < 10^{-6}$, at which point the corresponding value fo `emev = e(ie)*hbarc/mf` is printed as the three-body binding energy.

A.5 Computational details of the NN partial-wave analysis

The NN partial-wave analysis presented in this thesis is based on the publicly available `pyScattering` code [10], which provides Fortran routines for the computation of momentum–space NN interaction kernels. These routines were used as a starting point and interfaced with custom Python scripts developed for the present work to automate parameter scans and data analysis.

The numerical workflow adopted for the partial-wave sensitivity analysis can be summarized as follows:

1. Compilation of the NN interaction at fixed cutoff and chiral order.
2. Evaluation of the NN potential matrices in partial-wave representation on a discrete momentum grid.
3. Controlled multiplicative variations of individual NLO contact terms.
4. Re-evaluation of the partial-wave matrices for each parameter choice.
5. Extraction of low momentum sensitivity indicators and generation of diagnostic plots.

Unless otherwise stated, the NN interaction is evaluated on a momentum grid extending up to the cutoff value, and the sensitivity analysis is restricted to a low momentum region $k, k' \leq k_{\mathrm{max}}$ representative of few-body dynamics. Relative parameter variations of ±5% are employed throughout the analysis.

Table A.1: Summary of the numerical components used in the NN partial-wave analysis.

Component	Description
Fortran routines	NN interaction kernels (based on `pyScattering`)
Python scripts	Parameter scans and data analysis (this work)
Output format	Partial-wave potential matrices (*.npz* files)

List of Figures

List of Tables

Bibliography

[1] A C Phillips. Three-body systems in nuclear physics. *Reports on Progress in Physics*, 40(8):905, aug 1977.

[2] R. A. Malfliet and J. A. Tjon. Solution of the faddeev equations for the triton problem using local two-particle potentials. *Nuclear Physics A*, 127:161–168, 1969.

[3] S. P. Merkuriev and L. D. Faddeev. *The Quantum Mechanical Few-Body Problem.* Springer, 1993.

[4] Walter Glöckle. *The Quantum Mechanical Few-Body Problem.* Springer, 1983.

[5] Walter Gloeckle, H. Witala, D. Huber, H. Kamada, and J. Golak. The Three nucleon continuum: Achievements, challenges and applications. *Phys. Rept.*, 274:107–285, 1996.

[6] Evgeny Epelbaum, Hermann Krebs, and Patrick Reinert. High-precision nuclear forces from chiral eft: State-of-the-art, challenges, and outlook. *Frontiers in Physics*, Volume 8 - 2020, 2020.

[7] R Machleidt and F Sammarruca. Chiral eft based nuclear forces: achievements and challenges. *Physica Scripta*, 91(8):083007, July 2016.

[8] Steven Weinberg. Three-body interactions among nucleons and pions. *Physics Letters B*, 295(1–2):114–121, November 1992.

[9] Patrick Reinert. Partial wave analysis of NN scattering data in chiral EFT. *PoS*, CD2018:106, 2020.

[10] Hurongzhe. pyScattering: A python and fortran framework for nn scattering calculations. `https://github.com/hhurongzhe/pyScattering`, 2022. Accessed: 2026-02-05.

[11] Allen B. Downey. *Think Bayes: Bayesian Statistics in Python.* O'Reilly Media, 2013.

[12] Hao-Xiang Pan, De-Kai Kong, Qiao-Yi Wen, and Shao-Zhou Jiang. Bayesian method for fitting the low-energy constants in chiral perturbation theory. *Frontiers of Physics*, 19(6), August 2024.